

Westfälische
Wilhelms-Universität
Münster

Data-aware methods for the simulation of glioblastoma multiforme

Dissertation

Mathematik

**Data-aware methods for the
simulation of glioblastoma
multiforme**

Inaugural-Dissertation

zur Erlangung des Doktorgrades

Dr. rer. nat.

der Naturwissenschaften im Fachbereich

Mathematik und Informatik

der Mathematisch-Naturwissenschaftlichen Fakultät

der Westfälischen Wilhelms-Universität Münster

vorgelegt von

Michael Wenske

aus Bielefeld

Münster, 2020

Dekanin / Dekan:	Prof. Dr. Xiaoyi Jiang
Erster Gutachter:	Prof. Dr. Christian Engwer
Zweiter Gutachter:	Prof. Dr. Carsten Wolters
Tag der mündlichen Prüfung:	_____
Tag der Promotion:	_____

Abstract

This work is about the question of how mathematics may aid in the understanding and treatment of malignant brain tumors called glioblastoma multiforme (GBM). We present two independent approaches to this research question.

Firstly, we investigated how *a priori* information on the diffusive properties of the human brain measured by diffusion tensor imaging (DTI) may be leveraged for the numerical simulation of GBM tumor models. To investigate how to best utilize this data set, we incorporate a matrix Hölder mean into a vertex-centered finite volume method. We found that the choice of Hölder parameter α for the matrix mean can influence the numerical error significantly. We were able to identify the optimal Hölder parameter for our application ($\alpha \rightarrow 0$) resulting in a log-Euclidian matrix interpolation. We numerically compare our results to those of the industry-standard MPFA-O method (Aavatsmark, 2002). The Hölder finite volume method (HFVM) with the log-Euclidian matrix interpolation outperformed the MPFA-O method in all nontrivial testcases we investigated. This parameterized discretization scheme can be easily adjusted via the Hölder parameter. This is especially relevant in those cases, where the available resolution of the underlying data sets is fixed and the diffusivity field is strongly inhomogeneous. In these cases numerical grid refinement has limited benefits. The convergence of the method has been established numerically via inhomogeneous and anisotropic manufactured solutions.

The second contribution focuses on the modeling perspective. We derive a nonlinear penalty term for the 1D Fisher-KPP equation which allows the formulation of a stationary PDE problem to estimate the tumor invasion. This stationary formulation is perfectly aligned with datasets available at the time of diagnosis and makes quantifiable predictions that may aid medical treatment. We investigate the applicability first in simple artificial test settings. We then present results on two real 3D patient datasets. The 3D results allow direct comparison of its predictions with the medical treatment planning volumes (GTV, PTV, CTV). The results suggest that the stationalization procedure could provide medical practitioners with previously unavailable information for treatment radius delineation.

Zusammenfassung

In dieser Arbeit wird die Frage thematisiert, wie mathematische Methoden und Modellierung bei der korrekten Vorhersage und der Behandlung von Glioblastoma Multiforme helfen könnten. Es werden zwei unabhängige Ansätze eingeführt um diesem Ziel näher zu kommen.

Erstens beschreiben wir ein knotenzentriertes Finite-Volumen-Verfahren mit Matrix-Hölder-Mittel (HFVM). Die Verwendung des Hölder Mittels erlaubt es *a priori* Informationen über die zugrunde liegenden Materialeigenschaften direkt in die numerische Diskretisierung einfließen zu lassen. Die Konvergenz und die Diskretisierungsfehler dieser Methode wurden numerisch untersucht. Die numerischen Tests legen nahe, dass ein Matrix-Hölder-Mittel von $\alpha \rightarrow 0$, welches in einer Log-Euklidischen Matrix interpolation resultiert, für den Fall der numerischen Tumorsimulation die besten Ergebnisse erzielt. Im Vergleich mit der in der Praxis viel verwendeten MPFA-O Methode, zeigt sich die HFVM in allen von uns berücksichtigten Fällen überlegen.

Der zweite Beitrag ist ein approximativer Modellierungsansatz, welcher es erlaubt das Invasionsprofil der Tumorzelldichte stationär zu berechnen. Diese Stationalisierung kann anhand von der eindimensionalen Fisher-KPP Gleichung motiviert werden. Wir präsentieren ausführliche numerische Tests welche die Anwendbarkeit auf kompliziertere Tumormodelle untersuchen. Die Ergebnisse legen nahe, dass der Stationalisierungsansatz in Anbetracht der schwierigen Parametrisierung und Validierung der Vorwärtsmodelle einen wichtigen Beitrag leisten könnte. Die Ergebnisse der stationären Problemformulierung enthalten qualitative Informationen welche direkt für die medizinische Therapie verwendet werden können.

Acknowledgments

I would like to thank all the people who have been at my side during my academic studies and especially this PhD project. Without all of you this work would not have been possible. I would like to express gratitude towards:

Christian Engwer for the supervision throughout the years. Thank you for your scientific honesty, for leaving me enough room to approach the GBM problem from my own perspective and for tolerating my occasional stubbornness,

the *Bundesministerium für Bildung und Forschung* for funding the glioMath Project,

the PhD students from the glioMath project, especially Sven Knobe, Gregor Corbin and Anne Dietrich for their professionalism and solidarity during this project,

my colleagues Liesel Sommer, Nils-Arne Dreier, Marcel Koch, Jorrit Fahlke for the nice work environment, occasional advice and lots of shared hot and cold beverages,

Dr. Müller and Marcel Klose for helping me through some of the hardest parts of this project,

Joscha Hekele, Liesel Sommer and Jonas Ketteler for proofreading this document,

Sophie, für alles.

Ich möchte außerdem Gisela und Karl-Heinz Wenske für die jahrelange Unterstützung während meines Studiums und der Promotion danken.

Contents

Abstract	iii
Zusammenfassung	v
Acknowledgments	vii
List of Abbreviations	xii
List of Figures	xiii
List of Tables	xv
1 Introduction	1
1.1 Medical perspective	2
1.1.1 Diagnostic techniques	2
1.1.2 Treatment techniques	5
1.2 Mathematical forward modeling of GBM	8
1.3 Problems and challenges of the PDE models	11
1.4 Stationary modeling of GBM	15
1.5 Existing numerical approaches	16
1.6 Outline	17
2 Preliminaries	19
2.1 Notations	19
2.2 Fully anisotropic advection diffusion reaction equations	20
2.2.1 Péclet number	21
2.3 Variational formulation	21
2.4 Finite-dimensional space and grid	22
2.5 Matrix expressions	28
2.5.1 Matrix exponential and logarithm	28

2.5.2	Powers of a matrix	28
2.5.3	Artificial inhomogeneous diffusion	29
2.5.4	Fractional anisotropy	29
2.6	Manufactured solutions	30
2.6.1	Analytical solution	31
2.6.2	Analytical diffusivity field	31
2.6.3	Error definition	32
2.7	The MPFA-O method	33
3	The Hölder finite volume method	37
3.1	Problem description	38
3.2	Diffusivity averaging	40
3.2.1	Scalar averaging in flux discretizations	41
3.2.2	Matrix Hölder mean	43
3.3	Hölder finite volume method	47
3.4	Numerical convergence results	49
3.4.1	Inhomogeneous isotropic case (eigenvalue)	50
3.4.2	Homogeneous anisotropic case	51
3.4.3	Inhomogeneous anisotropic case (rotation)	53
3.4.4	Inhomogeneous anisotropic case (combined)	54
3.5	Conclusion	55
4	Stationalization	57
4.1	Forward tumor models	58
4.1.1	1D Fisher-Kolmogorov-Petrovsky-Piscounov equation	58
4.1.2	Myopic forward model	60
4.1.3	Haptotactic tumor model	61
4.2	Stationalization of Fisher-KPP equation in 1D	63
4.3	Stationalized tumor models	66
4.3.1	Notes on uniqueness	68
4.4	Numerical methods	69
4.5	Numerical results	71
4.5.1	1D homogeneous Fisher-KPP equation	71
4.5.2	1D myopic testcase	73
4.5.3	2D myopic diffusion model	73
4.5.4	Investigation of gradient statistics	76
4.5.5	3D comparison of forward and stationary solutions	79

5	Implementation: The DUNE-glio module	83
5.1	Features of DUNE-glio	83
5.2	Software architecture	84
6	Application to real data sets	87
6.1	The glioMath data set	87
6.1.1	Data preparation	88
6.2	Numerical results	90
6.3	Comparison via Péclet numbers	94
7	Discussion and outlook	97
7.1	Hölder finite volume method	97
7.1.1	Discussion	97
7.1.2	Outlook	99
7.2	Stationalization	100
7.2.1	Discussion	100
7.2.2	Outlook	102
8	Bibliography	107
	Appendix	120
A	Appendix	121
A.1	Reproduction of numerical results	121

List of Abbreviations

CFEM	Conforming finite element method
CT	Computer tomography with x-rays
DTI	Diffusion tensor imaging
DUNE	Distributed and unified numerics environment
ECM	Extracellular matrix
FAAD	Fully anisotropic advection diffusion (reaction) equation
FKPP	Fisher-Kolmogorov-Petrovsky-Piscounov equation
GBM	Glioblastoma multiforme
GTR	Gross tumor resection (treatment via operative removal)
HFVM	Hölder finite volume method
MMS	Method of manufactured solutions
MPFA	Multipoint flux approximation
MRI	Magnetic resonance imaging
RT	Radiotherapy (treatment via ionizing radiation)
SPD	Symmetric, positive definite matrices
TMZ	Chemotherapy (treatment via temozolomide)
TPFA	Two point flux approximation

List of Figures

1	Overview of segmentation and DTI modality (axial SEG + FA)	5
2	Visual comparison of <i>ideal</i> and <i>realistic</i> data set acquisition sequences . . .	12
3	Schematic of <i>ab initio</i> numerical setup	14
4	Schematic of postdiagnostic numerical setup	15
5	2D schematic representation of primal and dual grid.	24
6	Visual representation of subinterfaces and subvolumes within a primal grid cell	25
7	1D schematic of interleaving piecewise constant and Lagrange base.	27
8	Interaction region of the MPFA-O method	34
9	Schematic of simple TPFA flux discretization in two neighboring cells	39
10	1D schematic of scalar diffusivity interpolation for different Hölder parameters	43
11	Fractional Anisotropy and determinant of Hölder-interpolated matrices . . .	45
12	Schematic of quadrilateral and simplicial elements with internal subinterfaces.	46
13	Convergence plot for the eigenvalue variation case	51
14	Convergence plot for the homogeneous anisotropic case	52
15	Convergence plot for the inhomogeneous anisotropic case (rotation)	53
16	Convergence plot for the inhomogeneous anisotropic case (combined)	54
17	Example of an inhomogeneous anisotropic manufactured solution (combined)	56
18	Schematic of outwards- and inwards moving solution branches of the sta- tionalized formulation	68
19	Schematic of the characteristic level set distance	70
20	Numerical results for the 1D homogeneous stationalization	72
21	Numerical results for the 1D inhomogeneous stationalization	74
22	Numerical results of the 2D inhomogeneous stationalization tests	75
23	Visual comparison of the gradient statistics of the considered testcases . . .	77
24	Initial condition for the comparison of forward and stationary simulations. .	79

25	Comparison results of forward run and stationary simulation	81
26	Characteristic level set errors L_B for four simulations on a healthy subject's data set	82
27	Schematic of most important components of the DUNE-glio software module	85
28	3D visualization of the tumors in data sets #29 and #31	91
29	Axial view with level sets on data sets #29 and #31	92
30	Sagittal view with level sets on data sets #29 and #31	93
31	Frontal view with level sets on data sets #29 and #31	94
32	Comparison of level sets on solutions of problems with high and low Péclet number parameterizations	96

List of Tables

1	Integer labels of the segmented tissue compartments (SEG), estimated tumor density	4
3	Full set of parameters for the manufactured solutions	32
4	Overview of the considered convergence test cases for the HFVM method .	49
5	Manufactured solution parameters for the inhom. isotropic case	50
6	Manufactured solution parameters for the homogeneous anisotropic case . .	52
7	Manufactured solution parameters for the inhom. anisotropic case (rotation)	53
8	Manufactured solution parameters for the inhom. anisotropic case (combined)	55
9	Parameters used for the 3D stationary simulations of model (4.16a) resulting in a low effective Péclet number $Pe \approx 0.1$	80
10	The glioMath data set consisting of 15 pairs of DTI and corresponding segmentation data. Gender and age of subjects is unknown.	88
11	Parameters used for the 3D stationary simulations of model (4.16a) resulting in an effective Péclet number $Pe \approx 1$	95

1 Introduction

Glioblastoma multiforme (GBM) is a brain tumor that results from mutations of glia cells of the central nervous system (CNS). The prognosis for patients with GBM is quite poor, even with modern treatment techniques and imaging equipment. Cheo et al. (2017) analyzed the outcomes of 107 GBM patients in Singapore and found a median survival of 15.1 months and two-year survival rate of 23.5%. However, patients surviving for two years are not in the clear. The 10 year survival of patients with GBM was found to be 0.71% (Tykocki and Eltayeb, 2018).

The word multiforme describes the fact that its invasive profile can have a branched structure resulting in complicated tumor geometries. Also, the tumor shapes vary significantly between patients. This inhomogeneous shape, which extends outside of the tumor region visible on medical images, is a strong impediment towards effectively treating GBM (Painter and Hillen, 2013). The common treatments of GBM are radiotherapy (RT), gross tumor resection (GTR) as well as chemotherapy (TMZ). The Radiotherapy and resection both rely on the ability to delineate between healthy brain tissue that should be left intact and the tumorous tissue which should be removed or radiated. Due to the diffusive nature of the tumor cells this distinction is quite hard. Tumor cells have been histologically cultivated from healthy appearing tissue as far as 4 cm away from the bulk of the tumor (Silbergeld and Chicoine, 1997). Mathematical models have been developed to gain a deeper understanding of the invasion dynamics and to accurately predict further tumor invasion. Due to inter-patient differences and missing time series data sets these goals remain unreachable.

To give a detailed introduction into this topic we first describe the medical perspective in Section 1.1 where we cover the aspects most important to this work. The medical perspective is important to understand the real world problems of mathematical modeling of GBM and what our results may contribute.

We give an introduction to the mathematical view of the problem and the numerical methods in Sections 1.2 and 1.5. We limit the scope to PDE forward models, multiscale modeling and one stationary approach. We conclude the introduction by the outline of the rest of

the work in Section 1.6.

1.1 Medical perspective

The initial diagnosis is mostly based on computer tomography (CT) or magnetic resonance imaging (MRI). Depending on the location and size of the tumor, the symptoms include: persistent headaches, double or blurred vision, vomiting, loss of appetite, changes in mood and personality, changes in ability to think and learn, the onset of seizures and speech difficulty of gradual onset (of Neurological Surgeons, AANS; Chamberlain and Kormanik, 1998). The misattribution of these symptoms often delays the record of computer tomography (CT) or magnetic resonance imaging (MRI) scans, and therefore correct diagnosis and any targeted treatments.

When the tumors are diagnosed, their average diameter is already about 4 cm to 5 cm (Chamberlain and Kormanik, 1998). Generally, the GBM treatment methods following the diagnosis are palliative in nature, with the intent of prolonging survival and improving the quality of life of the patients (Chamberlain and Kormanik, 1998). Nonetheless, some progress has been made in recent years. The survival rates for 1 year and 3 years after diagnosis improved from 20.7% and 4.4% in 1999/2000 to 40.0% and 10.3% in 2009/2010 (deSouza et al., 2016).

1.1.1 Diagnostic techniques

We now shortly introduce the two imaging modalities, which we will rely on later in the document, and clearly explain what information they offer.

Diffusion Tensor Imaging (DTI)

Diffusion tensor imaging (DTI) is a noninvasive imaging technique developed since the 1990s. The DTI modality allows the measurement of approximate water diffusion tensors at any given location within the brain (Basser et al., 1994; Basser, 1995). To reconstruct the full tensors, a series of measurements is taken. In each of the measurements the

displacement of magnetizable water molecules in one spatial direction is captured. This displacement allows to reconstruct the approximate diffusivity in the measured direction. From the combination of many of those measurements it is possible to reconstruct the full water diffusion tensor $\mathbf{D}_w(x) \in \mathbb{R}^{3 \times 3}$ in each measurement voxel with a typical resolution of about 1-2 mm. For details of the measurement sequence and the reconstruction we refer to (Basser et al., 1994; Alexander et al., 2007; Atlas, 2009).

Most importantly, the DTI modality allows to capture not only the information entailed in a conventional MRI scan, but also indicates *directional information* indicating the location and orientation of fibres and directed tissue within the body. The water diffusion is comparatively strong in the direction parallel to the fibre orientation and weak in the perpendicular direction. It is known that the transport of tumorous glia cells happens primarily along these tracts, which makes the DTI data sets invaluable for making patient-based predictions both by medical practitioners and numerical modeling (Jbabdi et al., 2005; Engwer et al., 2015). For high enough resolutions, the increased anisotropy in white matter regions is clearly visible in DTI scans and makes it possible to distinguish different tissue types by properties like the fractional anisotropy (FA, see (2.33)) or the mean diffusivity of the measured tensors (Alexander et al., 2007; Özarslan et al., 2005). The DTI imaging modality is used in clinical practice for preoperative planning. It is used to locate the white matter tracts adjacent to the bulk tumor and their state of degradation. GBM causes both a distinct increase in mean diffusivity and a decrease in fractional anisotropy (FA) (Mekkaoui et al., 2016). The degradation of the anisotropy by the tumor bulk is clearly visible in Figure 1 (right).

Medical Segmentation of GBM (SEG)

A medical segmentation (SEG) is the automatic or manual selection of tissue volumes of different types. In the context of glioblastomas, the segmentation labels the extent of the predominantly tumorous tissue types next to the healthy tissue types (Simi and Joseph, 2015). Due to the diffusive nature of the tumor progression the correct classification at any given position is not trivial. There are several stages of tumor progression resulting in different imaging footprints, such as regions of active growth versus regions which are already necrotic. Segmenting tumors on medical images manually for operation and radiotherapy planning is still common practice in many treatment centers.

Recently, there have been advances in automatic multimodal brain tumor segmentation (Porz et al., 2014). The novelty in this regard is that the introduced software combines

information from four different MRI modalities to generate a segmentation: T1, T1-Gd (contrast agent), T2 and FLAIR. The four modalities each emphasize different tissue types. For example, the T1-weighted images can be used to effectively distinguish between grey and white matter regions. If additional contrast agents (e.g., gadolinium) are given to the patient the contrast between the blood vessels and the surrounding tissue is increased (Kalpathy-Cramer et al., 2014). The importance lies in the full automation, making the procedure comparable between institutions (and practitioners), which is an important prerequisite for further studies. A direct comparison of the manual segmentation of two medical practitioners and the automated segmentation via the software *BraTumIA* was performed in Porz et al. (2014) with promising results. The segmentation data sets used in this work have all been generated by this software. A comprehensive comparison of different automated algorithms can be found in (Simi and Joseph, 2015).

From a numerical standpoint, the 3D segmentation data sets can be considered as a tissue labeling in the form of integer values assigned to each voxel indicating its tissue compartment. The tissue compartments and the approximate volumetric tumor cell density assigned to them are listed in Table 1. We will make use of the information contained in the medical segmentations in Section 6.2. There, we assume a visibility threshold of 16% following Swanson et al. (2008). This threshold simply means that we assume the outer surface of the segmented volumes to have about 16% volumetric tumor density. An example of a medical segmentation with color code is shown in Figure 1 (left). We will introduce the modeling approaches utilizing DTI data sets shortly.

SEG	Tissue type	Volumetric tumor density
-1	Invalid	0.0
0	Background	0.0
1	Cerebral spinal fluid	0.0
2	Gray matter	0.0
3	White matter	0.0
4	Necrotic	0.16
5	Edema	0.16
6	Non-enhancing	0.8
7	Enhancing	1.0

Table 1: Integer labels and assumed tumor densities of the segmented tissue compartments. Enhancement refers to whether the tissue shows increased signal when contrast agent (gadolinium) is given to the patient. A volumetric tumor density of 100% indicates that the brain tissue entirely consists of tumorous tissue.

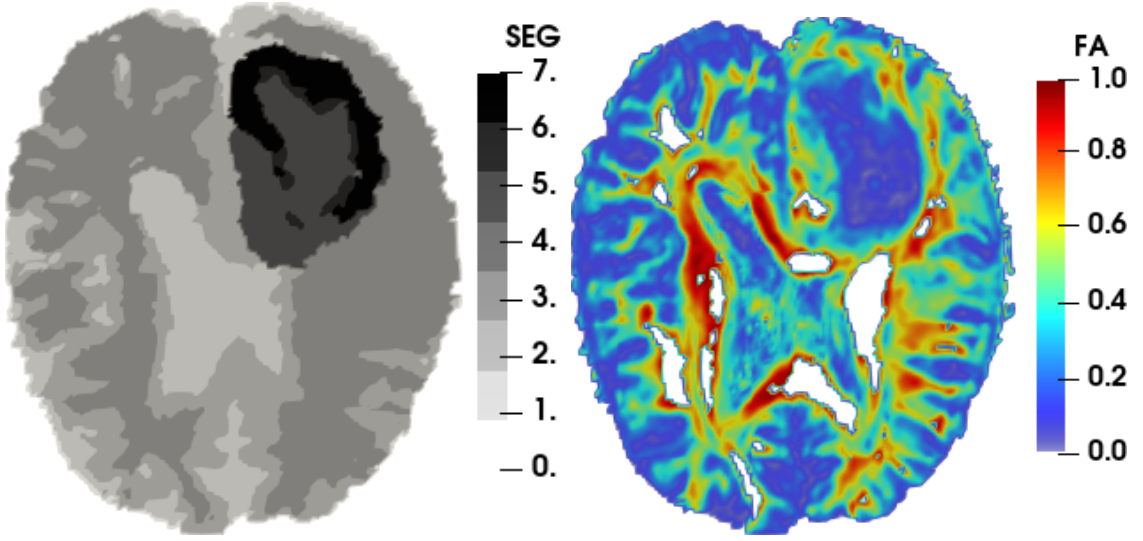


Figure 1: Axial slices ($z = 0.05$ m) of a patient diagnosed with GBM (data set #31). The tumor is visible in the upper right of the two slices. Left: Medical segmentation (SEG). Tissue types and approximate tumor volume percentage are listed in Table 1. Right: Fractional anisotropy (FA), see Equation (2.27). Regions with high FA indicate the white matter tracts. The reduction of anisotropy caused by the tumor is clearly visible in the upper right of the FA image.

1.1.2 Treatment techniques

Once the GBM diagnosis is established and medical images of the tumor are available, a combination of three treatment techniques is usually employed. These techniques are gross tumor resection of the bulk tumor in the form of operation, followed by radiotherapy with additional adjuvant temozolomide chemotherapy (Stupp et al., 2005). This standard treatment is also called the *Stupp regimen* (Nishikawa, 2010).

Gross tumor resection (GTR)

The objectives of the tumor resection are firstly to reduce the mass effect of the bulk on the rest of the brain and secondly, to further specify the diagnosis via biopsy of the removed tissue. Thirdly the aim is to remove the whole tumor if possible (Chamberlain and Kormanik, 1998). When the tumor volume includes important functional regions of the brain, the medical practitioner is faced with the choice of how much tissue to resect and how much

to leave in place. Removal of too much tissue risks the reduction of cognitive function, while resection of too little tissue is connected with the near-certainty of reoccurrence. From the patient's perspective this choice can mean improved quality of life for a shorter time or vice versa. The recommended extent of resection has been studied extensively with results advising generous resection. Lacroix et al. (2001) performed a multivariate analysis of 416 patients, investigating which treatment variants improved patient outcomes. They were motivated by the fact that previously the amount of resection was categorized very roughly into 'gross total resection', 'subtotal resection', 'partial resection', and 'biopsy sampling'. As a result, the classification into these categories was quite arbitrary. After analysis of their data set they found that the percentage of resection of the visible tumor had significant influence on the median survival. Resection of 98% or more resulted in a median survival of 13 months whereas the resection of less than 98% resulted in 8.8 months median survival. Ultimately, they recommend that maximal resection should be performed, but not at the expense of neurological function.

The clinical guidelines from the European Society for Medical Oncology (ESMO) similarly state that 'Surgery to the extent feasible is the first therapeutic intervention for all malignant glioma' (Stupp et al., 2014). What exactly that feasible extent is, is ultimately a judgment call from the handling practitioner. A recent review on the surgical state of the art was done by (Guzman et al., 2017).

There have also been attempts to model the effect of resection radius computationally. Hathout et al. (2016) studied the effect of the size of tumor resection *in silico*. Their numerical model is a Fisher-KPP equation with additional terms modeling the treatments. Their results indicate an increased survival time for total resection, and no prolonged survival time for partial or subtotal resection. In accordance with clinical experience, gliomas also appear incurable in these numerical models. This is the case no matter how extensive the resection is chosen due to the diffusive nature of the tumor cells (Hatzikirou et al., 2005; Swanson et al., 2003).

Radiotherapy (RT)

In radiation therapy high-energy x-rays or other ionizing radiation is applied to regions of the brain with the intent to destroy tumorous tissue. There are different approaches in choosing the treatment radii and intensities. The *University of Texas M. D. Anderson Cancer Center* (MDACC) recommends to use the following definitions of treatment radii (Chang et al., 2007).

Definition 1.1.1 (*Treatment volumes*)

- **GTV:** *Gross Tumor Volume: bulk tumor visible on medical images*
- **CTV:** *Clinical Target Volume: treatment radius for RT: $GTV + \text{margin}$ ($\approx 2\text{cm}$)*
- **PTV:** *Planning Target Volume: $CTV + \text{safety margin}$ ($\approx 0 - 5\text{mm}$).*

Radiation therapy based on these volumes will lead to treatment plans that do not include the peritumoral edema. A different approach is recommended by the Radiation Therapy Oncology Group (RTOG). They state that the radiation intensity to the peritumoral edema + 2 cm should be 46 Gy and to a central boost field ($GTV + 2.5\text{ cm}$) 60 Gy. Depending on the size of the edema, the second variant leads to a much greater target volume for the radiation treatment (Nelson et al., 1993; Chang et al., 2007). Both of the suggested treatment radii are only rough recommendations which do not take into account the relative importance of the different brain regions. In practice, medical practitioners deviate from these blunt recommendations to prevent radiation damage to the most important functional regions of the brain.

Similarly to the spatial extent of the treatment there are different approaches to the intensity of the irradiation. The accepted standard of care is adjuvant radiotherapy after resection for a total dose of 50.4 Gy ($28 \times 1.8\text{ Gy}$). Higher dosages did not improve overall survival, at least for lower grade gliomas (Karim et al., 1996; Stupp et al., 2014). Medical practitioners may deviate from this on a patient by patient basis. There is no established standard procedure for elderly patients. Initial studies indicated that for elderly patients the adverse effects of strong irradiative treatment outweighed the benefits (Nishikawa, 2010).

Nishikawa (2010) also state that: 'Because of the highly invasive nature of GBM, however high the irradiated dose is, the effect of radiotherapy would be limited as the irradiated field is restricted to the enhanced lesion.' In other words, due to the highly diffusive cells, it is not to be expected that all tumorous cells at the re-occurrence sites are effectively killed by radiotherapy, at least not without destroying significant amounts of predominantly healthy cells as well. Similarly to the situation of resective treatment, the handling medical practitioner has to make the judgment call of how much radiation should be administered and where.

Chemotherapy (TMZ)

1.2 Mathematical forward modeling of GBM

The mathematical modeling of glioblastoma multiforme has been extensive. The approaches vary from cellular automata and extensions to lattice-gas cellular automata over agent based models and even evolutionary game theory (Alfonso et al., 2017). The systematic review of all modeling approaches would be outside of the scope of this work and we will focus on exemplary forward models in the form of partial differential equations (PDE), and also mention one stationary approach. For a wider overview, we refer the reader to the excellent reviews by Hatzikirou et al. (2005), Harpold et al. (2007), Tracqui (2009) and Alfonso et al. (2017).

The PDE forward models describe the dynamic of the macroscopic tumor density $u(x, t) : \mathbb{R}^d \times T \rightarrow \mathbb{R}$ over time. The models differ by their inclusion or exclusion of anisotropic effects, by chemotactical or haptotactical drift terms, by whether they include terms describing therapy and by their choice of growth characteristic, e.g., exponential growth, logistic growth etc. In the following, we will further focus on three aspects of forward models, isotropic, anisotropic and models derived from multiscale approaches. These aspects are nonexclusive in the sense that models may fall into multiple of these categories.

Isotropic models

Swanson et al. (2000) presented an isotropic diffusion-reaction tumor model with exponential growth term $\frac{\partial u}{\partial t} = \nabla(D(x)\nabla u) + \rho u$, where $u(x, t) : \mathbb{R}^d \times T \rightarrow \mathbb{R}$ is a tumor cell density $D(x) : \mathbb{R}^3 \rightarrow \mathbb{R}$ an isotropic scalar diffusion coefficient and $\rho \in \mathbb{R}$ a proliferation rate. They used a binary segmentation of the brain to map grey and white matter regions to two constant isotropic diffusivities. This procedure does not take into account the directionality of the white matter tracts, but has the advantage that the necessary information can be reconstructed from T1/T2-MRI alone. This modeling approach marked an important first step in modeling GBM.

Similarly, Tracqui et al. (1995) used an isotropic diffusion model $\frac{\partial u}{\partial t} = D\Delta u + \rho u - K(t)u$ with exponential growth and a step function $K(t)$, modeling the effect of chemotherapy on the tumor. They derived the homogeneous diffusion parameter and growth rates via a best-fit with computer tomography data (Tracqui et al., 1995).

Anisotropic models

One of the first models that made direct use of DTI information was that of Jbabdi et al. (2005). There, the dynamic is modeled via a combination of anisotropic Fickian diffusion $\nabla \cdot (\mathbf{D}(x)\nabla u(x))$ and an exponential proliferation term. The novelty was that they used patient DTI data sets to reconstruct the inhomogeneous anisotropic diffusivity field $\mathbf{D}(x) : \mathbb{R}^3 \rightarrow \mathbb{R}^{3 \times 3}$. This exponential growth term is unrealistic for long simulation times, but may be appropriate for the early stages of the progression. Later, Swanson et al. (2011) presented a comparatively complex model which investigates the influences of hypoxia, necrosis and angiogenesis on the invasion of GBM. They modeled the dynamics of the tumor not by a single reaction-diffusion equation, but by a system of coupled PDEs. They were able to numerically reproduce effects like hypoxia and necrosis which are readily observed in patients.

One modeling challenge of the anisotropic models is the linkage of the DTI data sets, which represent measurements of the local *water* diffusivity $\mathbf{D}_w(x) : \mathbb{R}^3 \rightarrow \mathbb{R}^{3 \times 3}$, to the effective diffusivity of the *tumor* cells $\mathbf{D}_t(x) : \mathbb{R}^3 \rightarrow \mathbb{R}^{3 \times 3}$. This problem was already identified in the earlier work by Jbabdi et al. (2005). The size difference of water molecules and tumorous glia cells is about three orders of magnitude. Given this size difference, it is a modeling problem in itself to derive the permeability of glia cells in the biological tissue from the permeability of water molecules. Jbabdi et al. (2005) state that the anisotropy of the water diffusivity tensors gained from DTI data sets has to be increased to reproduce the medical observations. Even if some form of proportionality seems plausible, there are no rigorous ways to link these diffusivity values that could be motivated by the underlying physics. A very similar modeling problem appears in the attempt to use DTI tensor information to reconstruct the electric conductivity of brain tissue in electro- and magnetoencephalography source analysis (Vorwerk et al., 2014).

Two important reconstructions are the peanut distribution described in (Hillen, 2006), and the bimodal von-Mises-Distribution (Painter and Hillen, 2013). The practicability of both of them was investigated in Hunt (2018) where they eventually chose the peanut distribution. We follow their example and also use the peanut reconstruction in the model (4.7a), see Equation (4.8a). The main qualitative difference in the two reconstructions is, that the von-Mises reconstruction introduces a new parameter $\kappa \in \mathbb{R}$, which influences the effective anisotropy of the resulting tumor diffusion tensors, and therefore all subsequent numerical simulations. As of now, there is no reasonable way to estimate this parameter from either medical imaging or biomedical arguments. The peanut distribution is not reliant on such an additional parameter.

Multiscale modeling

Multiscale modeling refers to the practice of utilizing knowledge on the behaviour of individual cells on the microscopic scale, and deriving meso- or macroscopic evolution equations from them. The mathematical challenges are similar to the problems arising in statistical mechanics, but with the increased complexity of 'cell-particles' actively moving and changing directions. Important foundations for the biological application of the Boltzmann equation were laid by (Hillen, 2006; Painter and Hillen, 2013). We introduce the model by Engwer et al. (2015) as that is later used in the document and name important other contributions to multiscale modeling.

In (Engwer et al., 2015) and other similar multiscale models, the cell population is described by a (phase-space) density function $p(x, v, t, y) : \mathbb{R}^d \times \mathbb{R}^d \times \mathbb{R} \times \mathbb{R} \rightarrow \mathbb{R}$. This probability density describes the likelihood of finding a cell at location x with speed v and internal state y at any time t . In this particular model, the internal state y represents the number of surface receptors which are bound to the extracellular matrix. The inclusion of other internal dynamics is possible (Erban and Othmer, 2005). The kinetic equation

$$\frac{\partial p}{\partial t} = -\nabla_x(vp) - \nabla_y(G(y)p) - \lambda(y)p + \lambda(y) \int_V \kappa(x, v, v')p(v')dv'$$

describes the dynamics of how the phase space density changes over time. The probability density is affected by advection of cells in the direction of v via $-\nabla_x(vp)$. Also the velocities of the cells change with the turning rate $\lambda(y)$. This is expressed by cells changing orientation away from v via the term $-\lambda(y)p$ and cells changing orientation into v from v' expressed by the integral term. Within the integral is the turning operator $\kappa(x, v, v')$ expressing how exactly the changes in velocity are modeled. In the case of non-animate gas dynamics, this kernel is isotropic, homogeneous and given by the physics of colliding gas particles changing velocity. For the application of GBM modeling the environmental cues influencing the cell migration like the orientations of the tissue (DTI) or acidity gradients (chemotaxis) can be encoded in appropriate kernels $\kappa(x, v, v')$. In Engwer et al. (2015) the turning kernel was modeled to be $\kappa(x, v, v') = \frac{q(v')}{s^{n-1}}$ with a peanut distribution linking $q(v')$ to the water diffusion tensor as given by the DTI data sets. The cells are more likely to change their direction along the tissue orientation resulting in macroscopic drift terms. For the detailed derivation of the macroscopic PDE upscaling techniques we refer to the original publication and (Hillen and Painter, 2013), where they are introduced in detail.

The model (Engwer et al., 2015) was extended by including proliferative effects in (Engwer

et al., 2016). Hunt and Surulescu (2017) extended the model further by adding terms modeling the effects of chemotherapy, radiotherapy and resection. Another variant of multiscale modeling is to numerically solve the kinetic equations directly without deriving fully macroscopic equations. This approach was taken in (Corbin et al., 2018) and offers even more modeling flexibility at the cost of severely increased numerical cost.

The publication Corbin et al. (2020) to which we contributed the numerical implementation and results, describes an even more elaborate multiscale model. It includes macroscopic PDEs for a tumor cell density $u \in \mathbb{R}$, for a local acidity concentration $h \in \mathbb{R}$, the percentage of intact tissue $Q \in \mathbb{R}$ and the necrotic density $n \in \mathbb{R}$, as well as the coupling between these quantities. The model was implemented in DUNE-glio (See Section 5). The numerical simulations showed a necrotic core at the center of the tumor bulk, where the tumor cells die from high acidity and lack of nutrients. They also showed the active chemotactic repulsion of the tumor cells away from the high acidity regions in the center, as well as the degradation of tissue density Q due to the acid. The model incorporates a total of four superimposed advective fields influencing the tumor cell density. It is one of the most complex multiscale models we are aware of and gives unique insight into the possible inner workings of the infiltration process (Corbin et al., 2020).

Multiscale modeling in this elaboration is performed under the working assumption, that the correct parameterization of the equations will be available, and that there will be some way to define proper initial conditions for forward simulations. Even though the model is plausible in its predictions, it is currently unclear how initial conditions for the acidity field h , the tissue density Q and the necrotic field n should be estimated from medical data. There is also no reliable way to estimate the diffusivity of the acidity field h .

1.3 Problems and challenges of the PDE models

Even though numerous PDE forward models have been published, it has proven very difficult to validate or falsify them against experimental data. We now present the most important obstacles to GBM model validation.

Data set availability

So far there are no time-series of *untreated* patient DTI data sets of high grade gliomas. The only notable exception are Stensjøen et al. (2015), who gathered 106 T1-Gd MRI data sets from patients aged 26-83 years and measured the growth characteristics of the tumors. The time between the preoperative scans was at least 2 weeks for all considered patients. They found large variations in growth rates between patients. Also, they found that the growth for larger tumors seems to be slower than for smaller tumors. The mean volume doubling time was 29.8 days and the mean radial expansion velocity was 29.8 mm/year. Unfortunately, DTI data sets were not collected.

For a *conclusive quantitative comparison* between PDE forward models and actual GBM progression, a large and representative set of periodically repeated medical scans (MRI + DTI + SEG) would be needed, without the interference of therapeutic effects on the tumor growth. Gathering such a data set would imply to deprive the subjects of live-prolonging treatment, while burdening them with regular medical scans. The ethical impossibility of gathering such a data set is obvious. Indicative of this is also that even the authors of Stensjøen et al. (2015) themselves recommend that treatment should not be delayed after diagnosis, while following that same recommendation would have made their own survey impossible. Figure 2 illustrates a theoretically ideal and a realistic sequence of measurements for the validation of GBM models.

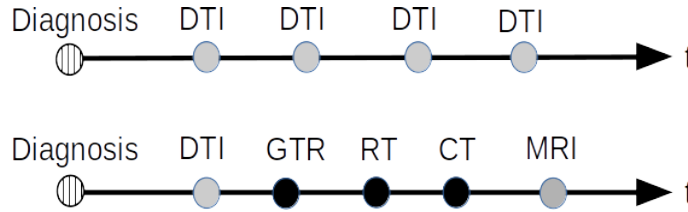


Figure 2: Top: ideal data set sequence for the validation of GBM forward models consisting of regular medical imaging without any treatment. Bottom: realistic data set sequence consisting of preoperative DTI followed by tumor resection (GTR), radiotherapy (RT), chemotherapy (CT/TMZ) with possible follow-up MRI scans.

Naturally, there are more data sets available of patients who were treated. If these data sets were used for validation, then the effects of the treatments had to be modeled and validated *alongside* the underlying tumor models. For large tumors, these effects would include the mechanical deformations of the brain during growth and following the resection.

One would not be able to assume that the preoperative DTI scans correctly represent the state of the patient brains after surgery. Also, since it is the outspoken goal of chemo- and radiotherapy to change the growth dynamics of the tumor, the correct parameterization of the growth terms before and during treatment is further hindered.

Validation attempts

DTI and segmentation data sets at one point in time, mostly the preoperative scans, are readily available. The glioMath data set presented in Section 6.1 is such an example. Several attempts were made to conduct numerical simulations with these preoperative data sets. We discuss two (numerical) experimental setups in detail, which are both based on DTI and segmentation data sets.

Ab initio setup

In this approach the location and initial cell density distribution $u_0(x) : \mathbb{R}^3 \rightarrow \mathbb{R}$ is *guessed* within an available DTI data set of either a healthy subject, or a patient taken at the time of diagnosis. For the healthy subject, one may inspect the predictions made by the underlying model and parameterization, and observe whether the effects envisioned within the modeling phase materialize as intended. For the healthy subject, there naturally is no way to tell how close the model prediction is to real tumor dynamics.

For the DTI scan taken of a patient at diagnosis, one has to assume that the diffusivity within the tumor mass was massively affected by the tumor during its growth. This reduction of anisotropy is visible in the upper right of Figure 1. Guessing the initial tumor distribution *within* this already degraded tissue may not be an optimal approach (Jbabdi et al., 2005; Swan et al., 2018). If the parameters are then determined to best fit the extent visible at diagnosis, strong over- or underestimation of the model parameters is to be expected. Within this setting, the interpretability of the simulated time is difficult as the (degraded) diffusivity field from the time of diagnosis is used for forward simulations up until the time of diagnosis. There is no precise way to estimate the time between carcinogenesis and diagnosis.

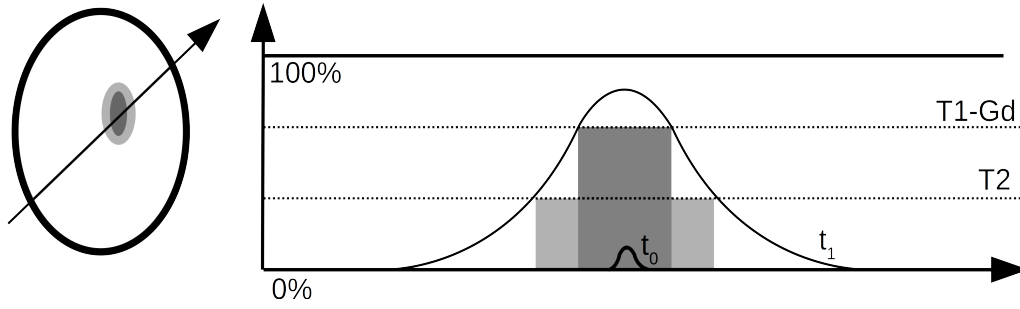


Figure 3: *Ab initio* numerical setup. Left: 2D schematic of skull with enclosed segmented tumor (grey) and location of a line plot. Right: Tumor density over a line through the tumor. Grey areas indicate the medical segmentation regions. The outer density distribution indicates an underlying real tumor distribution at the time of imaging t_1 . The initial tumor density distribution at t_0 is guessed within the existing tumor region, and a forward simulation is conducted.

Postdiagnostic setup

Since medical segmentations of the tumor mass can be derived from MRI/DTI images, one may try to use them as initial tumor density distributions, and conduct numerical simulations to predict further development. In this setup the evolution in the tumor center is mostly complete and the important growth dynamics will occur outside of the strongly degraded tissue. This approach is better aligned with the available data sets but also not without drawbacks.

The problem with this setup is, that the diagnostic scan is rapidly followed by gross tumor resection combined with radio- and chemotherapy which alter the geometry of the tissue and the growth dynamics significantly. This is by all means intended behavior, but also implies that these forward simulations may not offer any useful comparison if the complexities of the therapeutic effects are not modeled on top of the natural tumor growth. The segmentation information is thresholded in the sense that we may assume that only those regions with a tumor cell density higher than a certain value will be segmented correctly. If this segmentation is naively used as an initial condition, then we would assign a stepped density profile with sharp gradients at the start of the simulation (Fig. 4). Starting a simulation of the diffusive tumor models from such a sharp stepped initial condition will lead to very high fluxes in the first timesteps. We again find that the simulated time would not be interpretable, as we know that the initial condition is *lagging behind* the real underlying tumor distribution due to the thresholding.

Assuming, for the sake of argument, that a correct initial distribution would be available.

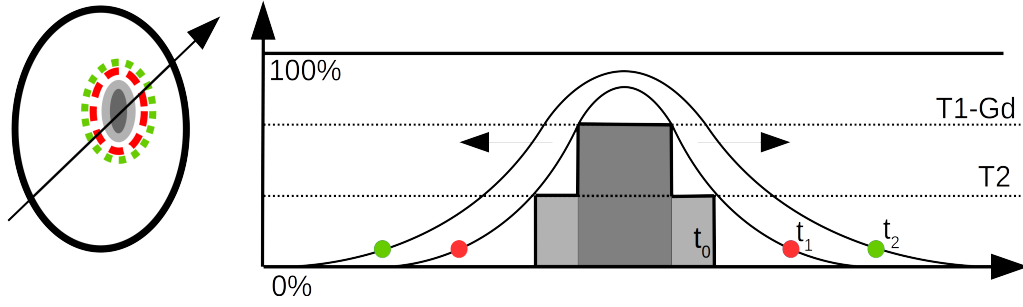


Figure 4: Postdiagnostic numerical setup. Left: 2D schematic of skull with enclosed segmented tumor (grey) and level sets of the density solution outside of the segmentation (dotted lines). The diagonal line indicates the line plot. Right: Tumor density over a line through the bulk. Grey areas indicate the medical segmentation regions. If the medical segmentation at the time of diagnosis t_0 is to be taken as initial condition, then a forward simulation would only reach the real underlying tumor profile at t_1 , thereby underestimating the actual extend of the tumor.

Then, a classic PDE forward simulation starting at the time of diagnosis, predicting the uninterrupted growth, would carry no practical information from the treatment perspective. The medically relevant information would be the full initial density distribution itself. A better estimation of this initial tumor distribution would enable more accurate targeting by treatment techniques such as resection or radiotherapy.

1.4 Stationary modeling of GBM

There have been attempts to model the invasion of GBM in a stationary way based on data sets from only one point in time. This approach aims at correctly predicting the state of tumor invasion at diagnosis, especially outside of the visible region. In the two publications Konukoglu et al. (2006) and Konukoglu et al. (2010) the authors proposed to estimate the extent of tumor invasion via traveling time formulations resulting in anisotropic eikonal equations. In this formulation, the principal variable $T(x) \in \mathbb{R}$ describes the time at which the tumor progression has reached the location $x \in \mathbb{R}^d$. A simple isotropic eikonal problem is given by

$$F\sqrt{(\nabla T)^T D \nabla T} = 1 \quad \forall x \in \Omega_b, \quad (1.1)$$

$$T(x) = T_0 \quad \forall x \in \Gamma, \quad (1.2)$$

with a parameter $F \in \mathbb{R}$ and a diffusivity $D \in \mathbb{R}$ and may be solved by a fast-marching algorithm (Konukoglu et al., 2007). Here, Ω_b denotes the whole brain and Γ the tumor outline given by the medical images. The stationary problem is augmented with the side condition (1.2) of the tumor delimiter visible on the medical images. Level sets of the solution to the eikonal problem formulation (1.1) can then be interpreted as the approximate front location after a given time $T > T_0$. This mathematical approach is quite different to the (multiscale) PDE modeling and also the stationalization we will present, but has been used to address the same problems of data availability and lack of parameterization.

1.5 Existing numerical approaches

In this work, we will present a parameterized finite volume discretization for anisotropic diffusion problems. To put our results into context and convey the possible advantages we now give a short overview of other discretization approaches for this class of problems.

Among the commonly used discretizations for anisotropic diffusion are the mimetic finite difference method presented by Lipnikov et al. (2014). In this approach, the discrete operators are constructed to mimic conservation laws, symmetry of the continuous differential operators and other properties. It is also algebraically asserted that the resulting operators conform to identities of vector- and tensor calculus. The discretization has been successfully applied to tumor models in (Hunt, 2018).

Another viable discretization is the discontinuous Galerkin method (Reed and Hill, 1973). In this finite element approach the polynomial trial functions may be discontinuous at cell boundaries. Here, similarly to finite volume methods, a flux integral is evaluated at the cell boundaries. The choice of a correct flux approximation at the cell boundaries and their discontinuities have been discussed in (Arnold et al., 2000).

In addition, there are numerous discretization schemes in the family of finite volume methods for anisotropic diffusion problems. Their main differences lie in the choice of control volume construction, the choice of flux discretization through the surfaces of these control volumes and the quadrature point locations on them. We recommend the reviews given by Barth et al. (2017) and Droniou (2014). Within the finite volume method family, the multipoint flux approximation (MPFA) methods have been successfully applied to discretize Equation (3.1) on orthogonal and non-orthogonal grids and for diffusivity fields which are not 'K-aligned', i.e., where the principal axes of the diffusivity tensors are not aligned with the grid faces. The MPFA method family offers increased precision at the cost of a wider

total stencil size compared to two point flux approximations. One special method is the so called *O-method*, named after the O-shaped region of the involved degrees of freedom in its flux reconstruction. The method is discretely mass preserving (Aavatsmark et al., 1996; Aavatsmark, 2002; Aavatsmark et al., 2007). The MPFA-O method has been described as the industry standard method in reservoir simulation (Klausen and Winther, 2006). We will present it in more detail in Section 2.7, as we will directly compare our discretization to it in Section 3.4.

The most extensive quantitative comparison of existing numerical methods for anisotropic diffusion (see Eq. (3.1)), that we are aware of, are the benchmarks by (Herbin and Hubert, 2008) and (Eymard et al., 2011). In these publications up to 20 different discretizations were tested and compared for precision and performance. The families of numerical discretizations that were considered include cell-centered finite volume schemes, the discontinuous Galerkin schemes, finite element discretizations and even lattice Boltzmann methods. The authors state that: 'schemes are not so easy to classify, and some schemes are known to be identical in special cases' (Herbin and Hubert, 2008). In light of our initial research question, it is therefore a non-trivial question which numerical discretization method is most suited to the simulation of GBM on real data sets. The Hölder finite volume method which we will present later in the document is an attempt to optimize anisotropic finite volume methods like the MPFA-O method for our use case.

The 2D benchmark (Herbin and Hubert, 2008) makes use of manufactured solutions of varying complexity to measure the accuracy of the numerical methods. The tests presented in Section 3.4 are inspired by their experimental setup but are significantly extended.

1.6 Outline

This work is divided into 7 Sections. Following this introductory section we will define all necessary notations in Section 2. We introduce the PDE model class of fully anisotropic advection diffusion reaction equations (FAAD). Also all necessary mathematical preliminaries for the definition of the Hölder finite volume method are defined, as well as the numerical setup for its convergence tests. For these convergence tests we define parameterized manufactured solutions. Also, we summarize the MPFA-O method in order to compare both methods.

In Section 3 the problem of diffusivity averaging for anisotropic inhomogeneous diffusion is described. Subsequently, the scalar and matrix Hölder mean are presented which are

then incorporated into the numerical discretization. Then, the full parameterized residual expression of the method is presented. A brief overview of our implementation in the software module DUNE-glio is given before numerical convergence tests are presented. These convergence tests make use of parameterized manufactured solutions which allow the investigation of different aspects of the method. For the subsequent numerical computations in two and three dimensions we used the Hölder finite volume method.

In Section 4, a stationary modeling approach is presented. This approach is independent of the choice of numerical discretization. We derive a nonlinear penalty term via the one-dimensional Fisher-KPP equation that allows us to formulate a stationary problem that is consistent with imaging data available from only one point in time. We establish the applicability to more complex models by increasing the model complexity step by step and validating that the approximation remains justified via comparisons to forward simulations gradient statistics.

Afterwards, we give a quick overview of the implementation module DUNE-glio in Section 5. There, we state some of its design decisions and an overview of its current capabilities. In Section 6 we present numerical results for the stationalized problem using two real 3D patient data sets. We present a conservative parameterization that results in tumor delineations that reproduce medical recommendations. We then compare these to a parameterization with stronger advective components to illustrate the possible advantages that the method may offer to medical practitioners.

We conclude the work by discussing both the Hölder finite volume method and the stationary modeling approach in Section 7. We also give an outlook on avenues of further improvement.

2 Preliminaries

2.1 Notations

$d \in \mathbb{N}$	The considered dimension of a problem
$\Omega \subset \mathbb{R}^d$	simulation domain
$\Omega_b \subset \mathbb{R}^d$	simply connected convex domain bounded by the brain's surface
Ω_i	<i>Internal</i> volume given by the tumor visible on DTI/MRI which is possibly non-convex and not connected (metastases)
$x \in \mathbb{R}^d$	Spatial coordinate, dimension d given by context
$t_0 \leq t \leq t_e \in \mathbb{R}$	Time variable
$T = [t_0, t_e] \subset \mathbb{R}$	The considered time interval in forward simulations.
$u(x, t) \in C^2 : \Omega_b \times T \rightarrow \mathbb{R}$	Time dependent scalar tumor density field
$u_s(x) \in C^2 : \Omega_b \rightarrow \mathbb{R}$	<i>Stationary</i> scalar tumor density field
$\mathbf{D}_w(x) : \mathbb{R}^d \rightarrow \mathbb{R}^{d \times d}$	<i>Water</i> diffusion tensor field (given by DTI)
$\mathbf{D}_t(x) : \mathbb{R}^d \rightarrow \mathbb{R}^{d \times d}$	<i>Tumor</i> diffusion tensor field
$\tilde{x} \in \mathbb{R}^d$	Nondimensionalized spatial coordinate
$\tilde{t}_0 < \tilde{t} < \tilde{t}_e \in \mathbb{R}$	Nondimensionalized time variables
$N_v \in \mathbb{N}$	Associated degrees of freedom within a (primal) grid cell
\mathcal{T}_h	Primary grid tessellation of Ω_b
\mathcal{X}_h	Dual grid tessellation of Ω_b
$N_p \in \mathbb{N}$	Total number of <i>primary</i> grid cells
$N_d \in \mathbb{N}$	Total number of <i>dual</i> grid cells
Q_k	Space spanned by monomials x_i^α with multiindex $\alpha \leq k$

$H^k(\Omega_b)$	Sobolev space of L^2 functions with weak derivatives defined up to $k \in \mathbb{N}$
$N_s \in \mathbb{N}$	Subinterfaces within one primal grid cell (2D: 4, 3D: 12)
$N_\theta \in \mathbb{N}$	Subvolumes within one primal grid cell (2D: 4, 3D: 8)
$\theta_i \in \Theta$	subvolume within $\tau_j \in \mathcal{T}_h$
$s_i \in \mathcal{S}$	subinterface within $\tau_j \in \mathcal{T}_h$

2.2 Fully anisotropic advection diffusion reaction equations

The PDE model class considered in this work is that of fully anisotropic advection diffusion reaction equations (FAAD). They describe the progression of a scalar time dependent tumor density field $u(x, t) \in C^2 : \Omega_b \times T \rightarrow \mathbb{R}$. We now introduce this model class, and will present three specializations in Section 4. The equation is stated in a general form to emphasize the similarities of many tumor forward models. We focus on those models that can be expressed as follows:

Definition 2.2.1 (*Fully anisotropic advection diffusion reaction equation*)

Let $\Omega_b \subset \mathbb{R}^d$ be a bounded domain (brain), $T = [t_0, t_e] \subset \mathbb{R}$ and $u(x, t) : \Omega_b \times T \rightarrow \mathbb{R}$ the volumetric tumor density. For an arbitrary $x \in \Omega_b$ we denote by $\mathbf{D}(x) : \mathbb{R}^d \rightarrow \mathbb{R}^{d \times d}$ the diffusion tensor, by $b(x) : \Omega_b \rightarrow \mathbb{R}^d$ the advective field, by $g(x) : \Omega_b \rightarrow \mathbb{R}$ the initial tumor density profile at initial time $t_0 \in \mathbb{R}$ and by $f(u(x, t)) : \mathbb{R} \rightarrow \mathbb{R}$ the reaction term. For given $\mathbf{D}(x), b(x), g(x)$ we seek the tumor density $u(x, t)$ so that

$$\begin{aligned} \frac{\partial u(x, t)}{\partial t} &= \nabla \cdot ((\mathbf{D}(x) \nabla u(x, t)) + b(x)u(x, t)) \\ &\quad + f(u(x, t)) \end{aligned} \quad \forall (x, t) \in \Omega_b \times T, \quad (2.1a)$$

$$0 = (\mathbf{D}(x) \nabla u(x, t) + b(x)u(x, t)) \cdot n, \quad \forall (x, t) \in \partial\Omega_b \times T, \quad (2.1b)$$

$$u(x, t_0) = g(x) \quad \forall x \in \Omega_b. \quad (2.1c)$$

where n denotes the normal vector at the outer surface.

We use this notation because many forward models can be expressed in this form, and merely differ in their definition of the diffusivity field $\mathbf{D}(x)$ and the modeled advective effects within $b(x)$. A classical solution to (2.1a) would require $f(u), g(x), b(x)$ and $\mathbf{D}(x)$ to be known and sufficiently smooth. In our case the advective fields and the diffusivity field are reconstructed from discrete data sets, and consequently we look for weak solutions of the continuous problem. Throughout this document, we will discuss three specializations of Equation (2.1a) in more detail (see Section 4).

2.2.1 Péclet number

The Péclet number Pe is relevant in the classification of transport problems and relates the relative strength of diffusion and advection against each other. A high local Péclet number indicates that a problem is advection-dominated whereas a low Péclet number indicates that a problem is diffusion-dominated. It may be used to allow better comparisons between models which consider different advective effects.

Definition 2.2.2 (*Péclet number*)

Let $b(x) \in \mathbb{R}^d$ be the local advective field, $|\mathbf{D}(x)|_F$ the Frobenius norm of the local diffusivity and $h \in \mathbb{R}$ a characteristic length (cell size). Then we define the local Péclet number

$$Pe(x) = \frac{|b(x)|h}{|\mathbf{D}(x)|_F}. \quad (2.2)$$

In Section 6 this quantity is used to compare stationary results for two model parameterizations which lead to high-Péclet and a low-Péclet number scenarios.

2.3 Variational formulation

We now formulate the problem of finding a solution to the FAAD equation (2.1a) in a variational setting. We recall the FAAD equation as

$$\frac{\partial u(x, t)}{\partial t} = \nabla \cdot ((\mathbf{D}(x) \nabla u(x, t)) + b(x)u(x, t)) + f(u(x, t)),$$

where the advective fields defined by the particular models are encased in $b(x)$ and the reaction terms within $f(u(x, t))$. We multiply by a piecewise constant test function $v \in L^2$, and integrate over a domain $\Omega \subset \mathbb{R}^d$ to obtain

$$\frac{d}{dt} \int_{\Omega} uv \, dx = \int_{\Omega} \left(\nabla \cdot ((\mathbf{D}\nabla u) + \mathbf{b}u) + f(u) \right) v \, dx. \quad (2.3)$$

We introduce the following notation for the *spatial* residual given by the right hand side as

$$r^s(u, v) = \int_{\Omega} \left(\nabla \cdot ((\mathbf{D}\nabla u) + \mathbf{b}u) + f(u) \right) v \, dx. \quad (2.4)$$

We integrate (2.3) over a small time interval $h \in \mathbb{R}$ via endpoint rule (implicit Euler),

$$\langle u^{t+h}, v \rangle = \langle u^t, v \rangle + h r^s(u^{t+h}, v), \quad (2.5)$$

where the two involved time steps are notated in superscript. We introduce the *spatio-temporal* residual

$$r^{st}(u^{t+h}, v) = -\langle u^{t+h}, v \rangle + \langle u^t, v \rangle + h r^s(u^{t+h}, v). \quad (2.6)$$

The weak problem for the forward model can now be stated as: find u^{t+h} such that

$$r^{st}(u^{t+h}, v) = 0, \quad (2.7)$$

i.e., that the spatio-temporal residual is minimized. As the reaction term $f(u)$ is generally nonlinear, the numerical solution can not be calculated directly but has to be approximated iteratively. In discretized form, the problem may be solved in a weak sense to arbitrary precision via classical Newton iteration until $|r^{st}| < \epsilon$ with $\epsilon \ll 1$. Hereinafter we will omit discussion of the temporal residual form and only state how the spatial residual contribution is calculated in Section 3. There, we will seek the discrete weak solution $u_h \in H^1$.

2.4 Finite-dimensional space and grid

We will now introduce a primary and secondary grid subdividing the simulation domain $\Omega_b \subset \mathbb{R}^d$ as well as the finite-dimensional spaces. The symbols introduced here will be used in the definition of the Hölder finite volume method in Section 3. We define the following

nonoverlapping partition

Definition 2.4.1 (Primal grid)

Let $N_p \in \mathbb{N}$ be the total number of cells subdividing $\Omega_b \subset \mathbb{R}^d$, we then define the set of primal grid cells

$$\mathcal{T}_h(\Omega_b) = \{\tau_1, \dots, \tau_{N_p}\} \quad N_p \in \mathbb{N}, \quad (2.8a)$$

$$\tau_i \subseteq \Omega_b \quad \text{for } 1 \leq i \leq N_p, \quad (2.8b)$$

$$\tau_i \cap \tau_j = \emptyset \quad \text{for } i \neq j, \quad (2.8c)$$

$$\Omega_b = \bigcup_{i=1}^{N_p} \tau_i. \quad (2.8d)$$

We will refer to any $\tau_i \in \mathcal{T}_h$ as a *primal* or *primary* grid cell. Within this document we assume convex quadrialateral hexahedral elements τ_i , each connecting four vertices in 2D and eight vertices in 3D.

Additionally, we define a second nonoverlapping hexahedral partition of Ω_b . These dual grid cells are constructed from the primal grid by joining the barycenter of any primal grid cell with the centers of its respective faces and edges, i.e., a median dual control volume construction. We chose the barycenter for construction as it is always within the primal grid cell.

Definition 2.4.2 (Dual grid)

Let $\mathcal{T}_h(\Omega_b)$ be a primal grid tessellation of the domain $\Omega_b \subset \mathbb{R}^d$, then the dual grid is given by $N_d \in \mathbb{N}$ cells χ which are constructed via median dual control volume construction, i.e., the connection of the primary cell barycenters with face and edge midpoints

$$\mathcal{X}_h(\Omega_b) = \{\chi_1, \dots, \chi_{N_d}\} \quad N_d \in \mathbb{N}, \quad (2.9a)$$

$$\chi_j \subseteq \Omega \quad \text{for } 1 \leq j \leq N_d, \quad (2.9b)$$

$$\chi_j \cap \chi_i = \emptyset \quad \text{for } i \neq j, \quad (2.9c)$$

$$\Omega = \bigcup_{j=1}^{N_d} \chi_j. \quad (2.9d)$$

We will refer to any $\chi_i \in \mathcal{X}_h$ as a *dual* grid cell. A schematic of the two grids is presented in Figure 5. Further, we define the skeleton of the dual grid. This skeleton can be subdivided

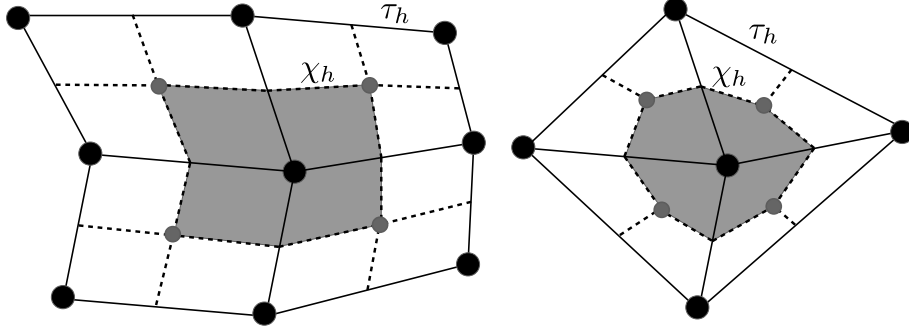


Figure 5: Schematic representation of unstructured primal grid cells (black lines), and their induced dual grid cells (grey area, dashed lines), created by joining the primal grid cell centers (grey dots) with the primal grid face centers. The degrees of freedom are associated with the vertices of the primal grid (black dots). Later, the finite volume fluxes will be discretized over the surface enclosing each dual grid cell while assembly is expressed over primary grid cells.

into subinterfaces.

Definition 2.4.3 (Dual grid skeleton)

Let f be the shared interface of any adjacent pair of dual grid cells in \mathcal{X}_h . We then define the internal skeleton of the dual grid as

$$\Gamma = \{f_{i,j} = \partial\chi_i \cap \partial\chi_j \mid \chi_i, \chi_j \in \mathcal{X}_h; i \neq j; |f_{i,j}| > 0\}. \quad (2.10)$$

Further, we denote the subset of Γ which lies within a primal grid cell $\tau_i \in \mathcal{T}_h$ as

$$\Gamma_i = \Gamma \cap \tau_i \quad (2.11)$$

We now define subinterfaces within the primal grid cells. These subinterfaces are each part of the skeleton of the dual grid. Any internal dual grid cell is fully encased by a certain number of subinterfaces (2D: 8, 3D: 24). We can define the subinterfaces as

Definition 2.4.4 (Subinterfaces)

For a primal grid cell $\tau_j \in \mathcal{T}_h$, and the faces $f_{k,l}$ connecting $\chi_k, \chi_l \in \mathcal{X}_h$ we define its $N_s \in \mathbb{N}$ subinterfaces as $s_i \in \mathcal{S}$, where

$$\mathcal{S} = \{f_{k,l} \cap \tau_j \neq \emptyset; k \neq l\}. \quad (2.12a)$$

In two-dimensional quadrilateral grids there are $N_s = 4$ subinterfaces within each primal grid cell, in three dimensions we find $N_s = 12$. Each subinterface connects two adjacent dual grid cells and is part of the dual-grid skeleton Γ (see Eq. (2.11)). Consequently, any integration over Γ may be expressed as the sum of integrations over all subinterfaces $s_i \in \mathcal{S}$. We will make use of this in Section 3 to express residual contributions from the perspective of any given primary grid cell. In two dimensions and quadrilateral grid geometry there are four subinterfaces within any primary grid cell $\tau_i \in \mathcal{T}_h$, as illustrated in Figure 6 and twelve subinterfaces within a hexaedral 3D cell.

Similarly to the definition of the subinterfaces subdividing the dual grid's surface, we define subvolumes subdividing its volume. The subvolumes are each given by the overlap of a primary and dual grid cell.

Definition 2.4.5 (Subvolumes)

For a primal grid cell $\tau_j \in \mathcal{T}_h$ we define its subvolumes as $\theta_k \in \Theta$, where

$$\Theta = \{\chi_k \cap \tau_j \neq \emptyset \mid \chi_k \in \mathcal{X}_h\}. \quad (2.13a)$$

These *subvolumes* θ_k lie within τ_j and are each associated with one corner degree of freedom. In two dimensions we find four subvolumes making up a primal grid cell, in three dimensions there are eight subvolumes. An example of subinterfaces and subvolumes within a primal grid cell is depicted in Figure 6.

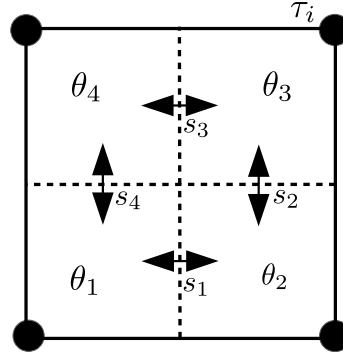


Figure 6: Illustration of four subinterfaces $s_k \in \mathcal{S}$ and four subvolumes $\theta_i \in \Theta$ lying within a primal grid cell $\tau_j \in \mathcal{T}_h$. The primal grid cell is again shown with black lines, while the borders of the dual grid cell are shown in dashed lines.

We will later use the subinterfaces $s_i \in \mathcal{S}$ and subvolumes $\theta_k \in \Theta$ to express the surface and volume integrals within the Hölder finite volume method (Section 3). We now state

the discrete function space and bases used later in the document. Let

$$Q_k^d = \text{span} \left\{ \prod_{i=1}^d x_i^{\alpha_i} : 0 \leq \alpha_i \leq k, \text{ for } i = 1, \dots, d \right\} \quad (2.14)$$

be a space of polynomials. Here, $x = (x_1, \dots, x_d)^T$ and $\alpha = \alpha_1, \dots, \alpha_d$ is a multiindex. We define the space of piecewise d-linear functions

$$U_h = \{v \in C^0(\Omega) : \forall \tau_i \in \mathcal{T}_h : v|_{\tau_i} \in Q_1^d\} \quad (2.15)$$

on the primal grid, and the space of piecewise constant functions on the dual grid

$$V_h = \{w \in L^2(\Omega) : \forall \chi_i \in \mathcal{X}_h : w|_{\chi_i} = \text{const}\}. \quad (2.16)$$

We define the Lagrange base for U_h with N_d as the total number of degrees of freedom, and N_v as the number of associated vertex degrees of freedom as

$$\Phi = \{\phi_1, \dots, \phi_{N_d}\} \subset U_h, \forall \tau_j \in \mathcal{T}_h \quad (2.17a)$$

$$\sum_{i=1}^{N_v} \phi_i(x) = 1 \quad \forall x \in \tau_j, \quad (2.17b)$$

$$\phi_i(x_k) = \delta_{i,k} \quad \text{for every (primal) vertex position: } x_k, k \in \{1, \dots, N_v\} \quad (2.17c)$$

Each base function ϕ_i is associated with one vertex of the primary grid. We may then approximate a continuous scalar function $u(x) : \Omega_b \rightarrow \mathbb{R}$ and its gradient via this finite-dimensional base

$$u_h(x) = \sum_{i=1}^{N_d} u_i \phi_i(x) \quad \forall x \in \Omega_b, \quad (2.18)$$

and

$$\nabla u_h = \sum_{i=1}^{N_d} u_i (\nabla \phi_i(x)) \quad \forall x \in \Omega_b, \quad (2.19)$$

where $u_i \in \mathbb{R}$ are the local degrees of freedom associated with the primary grid vertices.

Remark 2.4.1 *In finite volume methods which approximate the primary variable via a piecewise constant base, the gradient at the control volume surfaces is ill-defined, and often approximated in an ad-hoc fashion. Since we use a Lagrange base defined on the primary grid and control volumes given by the dual grid, the full gradient can easily be evaluated. In our formulation the gradient approximation (2.19) is used at the subinterfaces which encase the control volume (Figure 7).*

In addition to the Lagrange base defined above, we define a set of base functions which are piecewise constant on the dual grid cells as

$$\Xi = \{\xi_1, \dots, \xi_{N_d}\} \in V_h \quad (2.20a)$$

$$\xi_i(x) = \begin{cases} 1 & \text{if } x \in \chi_i, i \in \{1, \dots, N_d\} \\ 0 & \text{else.} \end{cases} \quad (2.20b)$$

We then define the piecewise constant test function $v_h(x) \in V_h$ as

$$v_h(x) = \sum_{i=1}^{N_d} \xi_i \quad (2.21)$$

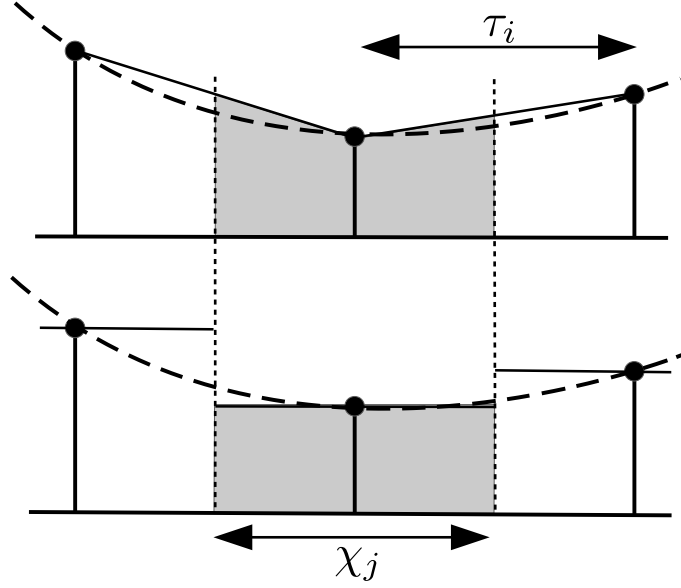


Figure 7: One-dimensional schematic of the finite-dimensional approximation of an exemplary function (dashed) by a d-linear base (top) on primal grid cells, i.e. $\tau_i \in \mathcal{T}_h$, and a piecewise constant base (bottom) on dual grid cells, i.e. $\chi_j \in \mathcal{X}_h$. One important property of this setup is, that the gradient of the d-linear Q_1 -base, defined on the primal grid, is continuous at the subvolume interfaces (subinterfaces), where the flux integral is evaluated.

2.5 Matrix expressions

We now define some expressions regarding symmetric positive definite matrices, which are used later in the document. We define matrix exponentiation and logarithms, the powers of invertible matrices and how we generate scattered diffusivity fields for numerical tests. We also define the fractional anisotropy.

2.5.1 Matrix exponential and logarithm

When we introduce the matrix Hölder mean we will make use of matrix exponentials defined as follows.

Definition 2.5.1 (*Matrix exponential*)

Let $\mathbf{A} \in \mathbb{R}^{d \times d}$ be a symmetric positive definite matrix. We then define the matrix exponential

$$\exp(\mathbf{A}) = \sum_{i=1}^{\infty} \frac{\mathbf{A}^i}{i!}. \quad (2.22)$$

Details on this definition can be found in (Hall, 2015). The corresponding matrix logarithm is given by

Definition 2.5.2 (*Matrix logarithm*)

Let $\mathbf{A} \in \mathbb{R}^{d \times d}$ be a symmetric positive definite matrix. We then define the matrix logarithm

$$\log(\mathbf{A}) = \sum_{i=1}^{\infty} (-1)^{i+1} \frac{(\mathbf{A} - \mathbb{1}_d)^i}{i}. \quad (2.23)$$

2.5.2 Powers of a matrix

We define the power of a symmetric positive definite and therefore invertible matrix $\mathbf{A} \in \mathbb{R}^{d \times d}$, with $\alpha \in \mathbb{R}$ via its diagonalization $\mathbf{A} = \mathbf{T} \mathbf{D} \mathbf{T}^{-1}$ as

$$\mathbf{A}^\alpha = \mathbf{T} \mathbf{D}^\alpha \mathbf{T}^{-1} \quad (2.24)$$

An efficient implementation of the matrix exponentiation, the logarithm and a diagonalization are available in the `armadillo` C++ software library (Sanderson and Curtin., 2016; Sanderson and Curtin, 2018).

2.5.3 Artificial inhomogeneous diffusion

In Section 4.5.2 we introduce numerical test cases in 1D and 2D with randomly perturbed isotropic diffusion coefficients $\mathbf{D}_\beta(x) \in \mathbb{R}^{d \times d}$. We define the diffusion matrices as

$$\mathbf{D}_\beta = \mathbf{1}_d \delta^{\frac{1}{d}}, \quad (2.25)$$

with $\delta \in \mathbb{R}$ being a uniformly distributed random value: $\delta = \text{unif}(1 - \beta, 1 + \beta)$. Here, $d \in \mathbb{N}$ is the spatial dimension. The exponent $\frac{1}{d}$ is chosen to allow comparisons between the isotropic homogeneous case and the randomized case by assuring that the average of the determinants of the diffusive medium are close to unity for every realization of the random field:

$$\det(\mathbf{D}_\beta) \approx 1 \quad \forall d \in \mathbb{N}. \quad (2.26)$$

We only compare homogeneous and inhomogeneous cases with identical grid resolution. We evaluate the random inhomogeneous diffusion at the primal grid vertices. The diffusivity within one dual grid cell is therefore statistically independent from any neighbor.

2.5.4 Fractional anisotropy

The fractional anisotropy (FA) is a skalar value describing how anisotropic a given symmetric positive definite matrix is. We follow the definitions from the literature (Basser and Pierpaoli (2011); Painter and Hillen (2013)).

Definition 2.5.3 (*Fractional anisotropy*)

Let $\mathbf{D}_w \in \mathbb{R}^{3 \times 3}$ be a symmetric positive definite matrix (water diffusion), then the local

fractional anisotropy $FA(\mathbf{D}_w) \in [0, 1]$ is given by

$$FA(\mathbf{D}_w) = \sqrt{\frac{1}{2} \left(3 - \text{tr} \left(\left(\frac{\mathbf{D}_w}{\text{tr}(\mathbf{D}_w)} \right)^2 \right)^{-1} \right)}. \quad (2.27)$$

Here, $FA(\mathbf{D}_w) = 0$ would correspond to an isotropic case, and $FA(\mathbf{D}_w) = 1$ would describe a completely anisotropic diffusivity \mathbf{D}_w .

2.6 Manufactured solutions

For the numerical tests of the Hölder finite volume method we will make use of the method of manufactured solutions (MMS). For these tests we solve a stationary inhomogeneous anisotropic diffusion problem $\nabla \cdot (\mathbf{D}_a(x) \nabla u(x)) = f(x)$ in two dimensions. The general idea of the MMS is to choose an analytical expression for a solution $u(x) : \mathbb{R}^2 \rightarrow \mathbb{R}$ and the diffusivity field $\mathbf{D}_a(x) : \mathbb{R}^2 \rightarrow \mathbb{R}^{2 \times 2}$ to then derive the necessary source term $f(x) : \mathbb{R}^2 \rightarrow \mathbb{R}$ analytically. The approach is useful to validate codebases for proper convergence and accuracy. In our case it serves the two-fold purpose of firstly validating that the inhomogeneous anisotropic diffusive fluxes were correctly discretized and secondly as a means of investigating the effect of different matrix Hölder means.

The chosen solution $u(x)$ does not necessarily have to be physically plausible to serve in code validation (Roache, 2001). Since our focus lies on inhomogeneous anisotropic diffusion, we construct a spatially varying analytic diffusion field $\mathbf{D}_a(x)$. The diffusivity field presented here is comparatively complex. This complexity is necessary to capture those aspects of the numerical discretization which are nontrivial. These aspects are for example the rapid spatial changes in diffusivity $\mathbf{D}_a(x)$ with regard to total amplitude (determinant), and with respect to direction of the strongest eigenvector, i.e., the principal direction of the diffusivity. The solution and the diffusivity field are parameterized in a way that allows us to conveniently inspect these corner cases. We now define all necessary terms and provide a complete list of parameters in Table 3. An example plot of one particular configuration used in Section 3.4.4 is given in Figure 17.

2.6.1 Analytical solution

We now define the analytical solution $u_a(x) : [0, 1]^2 \rightarrow \mathbb{R}$. It is constructed to be zero at the border to allow for simple homogeneous Dirichlet boundary conditions

$$u_a(x) = c_u \sin(2\pi p_u x_0) \sin(2\pi p_u x_1), \quad \text{with } x \in [0, 1]^2; c_u, p_u \in \mathbb{R}. \quad (2.28)$$

We employ a comparatively simple solution form for $u(x)$ because the interest lies primarily in the correct interpolation of the diffusivity field and not so much in the gradient discretization.

2.6.2 Analytical diffusivity field

We construct the diffusion matrix field $\mathbf{D}_a(x) : [0, 1]^2 \rightarrow \mathbb{R}^{2 \times 2}$ by first setting a diagonal matrix with spatially varying components $a(x), b(x) : [0, 1]^2 \rightarrow \mathbb{R}$. Then this diagonal matrix is turned at each point in space by a rotating angle $\beta(x) : [0, 1]^2 \rightarrow [0, 2\pi]$ via the rotation matrix $\mathbf{T}(\beta(x)) \in \mathbb{R}^{2 \times 2}$

$$a(x) = a_{xx}(1.1 + \sin(2\pi p_d x_0)) \quad \text{with } a_{xx}, p_d \in \mathbb{R}, \quad (2.29)$$

$$b(x) = a_{yy}(1.1 + \sin(2\pi p_d x_1)) \quad \text{with } a_{yy}, p_d \in \mathbb{R}, \quad (2.30)$$

$$\beta(x) = \frac{\pi}{2} \sin(2\pi p_\beta x_0^4) \sin(2\pi p_\beta x_1^4) \quad \text{with } p_\beta \in \mathbb{R}. \quad (2.31)$$

The rotation matrix is given by

$$\mathbf{T}(\beta(x)) = \begin{pmatrix} \cos(\beta(x)) & -\sin(\beta(x)) \\ \sin(\beta(x)) & \cos(\beta(x)) \end{pmatrix}. \quad (2.32)$$

The diffusion matrix field thus becomes

$$\mathbf{D}_a(x) = \mathbf{T}(\beta(x)) \begin{pmatrix} a(x) & 0 \\ 0 & b(x) \end{pmatrix} \mathbf{T}^{-1}(\beta(x)). \quad (2.33)$$

Inserting above relations into $\nabla \cdot (\mathbf{D}_a(x) \nabla u(x))$ provides the induced source term

$$f(x) = \nabla \cdot (\mathbf{D}(x) \nabla u_a(x)) \in \mathbb{R}. \quad (2.34)$$

The expanded form of $f(x)$ can be derived analytically due to the use of easily differentiable trigonometric functions. Validation with a CAD system (MATLAB, 2016) was performed. The reaction term $f(x)$ can be evaluated analytically, i.e. not via the d-linear base, as both $u_a(x)$ and $\mathbf{D}(x)$ are given.

For any chosen amplitude parameter $c_u \in \mathbb{R}$, any diffusion coefficients $a_{xx}, b_{yy} \in \mathbb{R}$ and any whole number of periods p_u for rotating the diffusivity field $p_\beta \in \mathbb{R}$ the above solution strictly abides the Dirichlet boundary conditions and allows us to test the generated finite volume methods for any measure of anisotropy, inhomogeneity and gradient amplitude. We provide a full list of parameters in Table 3. In the numerical tests in Section 3.4 we varied p_d and p_β , and the diagonal entries a_{xx} and a_{yy} . A visual representation of the manufactured solution is given in Figure 17.

Parameter	Effect on solution $D_a(x)u_a(x)$
$p_u = 0.5$	periods of $u(x)$
$p_d \in \mathbb{R}$	periods of $a(x), b(x)$
$p_\beta \in \mathbb{R}$	periods of angle β
$c_u = 10^3$	amplitude factor for $u_a(x)$
$a_{xx} \in \mathbb{R}$	base amplitude for D_{xx}
$a_{yy} \in \mathbb{R}$	base amplitude for D_{yy}

Table 3: Full set of parameters of the manufactured solution. Those that are constant throughout this manuscript are only defined here, variations in p_d, p_β, a_{xx} and a_{yy} are stated in Section 3.4.

2.6.3 Error definition

In Section 3 we will present a Hölder finite volume method, which has a free parameter. We will numerically investigate the convergence of different Hölder methods and compare it to other numerical discretizations. For this, we define the considered global error as

Definition 2.6.1 (Global L^2 -errors)

Let $u_a(x) : \Omega \rightarrow \mathbb{R}$ be an analytical solution, and $u_h(x)$ the numerical approximation to it.

We then denote the global L^2 -error as

$$\|u_a - u_h\|_{L^2(\Omega)} = \sqrt{\sum_{i=1}^{N_p} \int_{\tau_i} (u_a - u_h)^2 dx}. \quad (2.35a)$$

At this point we do not specify the particular base of u_h as we will later compare multiple different discretization methods.

2.7 The MPFA-O method

We now present the two-dimensional MPFA-O method as described in (Aavatsmark, 2002). It will serve as a reference to better contextualize the construction and the performance of the HFVM presented later in the document.

The MPFA-O method is a finite volume method where each primary grid cell is associated with one degree of freedom. To discretize the flux across the primary grids surface, an O-shaped interaction region is defined which overlaps the primary grid cell. For structured hexahedral grids this interaction region is given by a dual grid cell overlapping a corner of a primary grid cell. For any of these interaction regions the MPFA-O defines how to derive a local transmissibility matrix $\mathbf{T} \in \mathbb{R}^{4 \times 4}$ which allows the calculation of the flux densities $\mathbf{f} \in \mathbb{R}^4$ at the four subinterfaces lying within the interaction region. It is derived for each interaction region algebraically by setting up a small local system expressing two necessary conditions. Firstly, the fluxes have to be symmetric at the outer corner points of the subinterfaces. This property assures the discrete mass preservation of the method. Secondly, the density itself has to be continuous at the subinterface corner points and has to be consistent with the degree of freedom at the center of the primary grid cells. This implies that within the four subvolumes making up an interaction region the density is given by a linear function. We will now shortly present how the flux is reconstructed with this method. A 2D primary grid cell and one of its interaction regions is shown in Figure 8. For the construction we define the four corner degrees of freedom of the interaction region as $z = (z_1, z_2, z_3, z_4)^T \in \mathbb{R}^4$, the continuity points of the density as $\bar{z} = (\bar{z}_1, \bar{z}_2, \bar{z}_3, \bar{z}_4)^T$, and the material diffusivities as $\mathbf{D}_i \in \mathbb{R}^{d \times d}$. The subinterface values \bar{z}_i are merely intermediate variables helping in the construction and are eliminated later. For the four subinterfaces

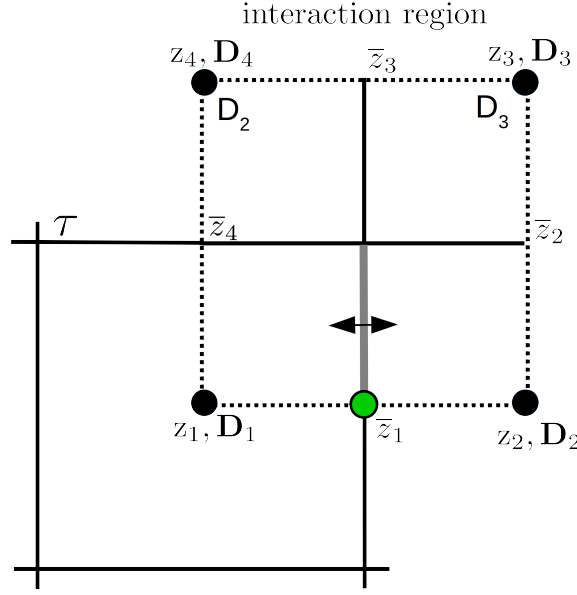


Figure 8: 2D interaction region of the MPFA-O method (dashed). The black lines indicate the primary grid associated with one degree of freedom z_1 and diffusivity $\mathbf{D}_1 \in \mathbb{R}^{2 \times 2}$. The dashed area indicates the interaction region for the subinterface marked in grey. The point where continuity of potential \bar{z}_1 is demanded is marked with a green dot.

indicated in Figure 8 the equal fluxes from both sides of the subinterfaces are

$$\begin{aligned}
 \mathbf{D}_{1,11}(\bar{z}_1 - z_1) + \mathbf{D}_{1,12}(\bar{z}_4 - z_1) &= \mathbf{D}_{2,11}(z_2 - \bar{z}_1) + \mathbf{D}_{2,12}(\bar{z}_2 - z_2), \\
 \mathbf{D}_{2,22}(\bar{z}_2 - z_2) + \mathbf{D}_{2,21}(z_2 - \bar{z}_1) &= \mathbf{D}_{3,22}(z_3 - \bar{z}_2) + \mathbf{D}_{3,21}(z_3 - \bar{z}_3), \\
 \mathbf{D}_{3,11}(z_3 - \bar{z}_3) + \mathbf{D}_{3,12}(z_3 - \bar{z}_2) &= \mathbf{D}_{4,11}(\bar{z}_3 - z_4) + \mathbf{D}_{4,12}(z_4 - \bar{z}_4), \\
 \mathbf{D}_{4,22}(z_4 - \bar{z}_4) + \mathbf{D}_{4,21}(\bar{z}_3 - z_4) &= \mathbf{D}_{1,22}(\bar{z}_4 - z_1) + \mathbf{D}_{1,21}(\bar{z}_1 - z_1),
 \end{aligned} \tag{2.36}$$

where the first line corresponds to the grey subinterface indicated in Figure 8. The first index of \mathbf{D} indicates the associated corner of the interaction region, the other two indicate the matrix entries.

The system of equations (2.36) can be written in more concise form with the vectors of interface and corner values \bar{z} and z and the four matrices $\mathbf{A}, \mathbf{B}, \mathbf{C}, \mathbf{D} \in \mathbb{R}^{4 \times 4}$ (Aavatsmark, 2002). The four subinterfaces fluxes $f \in \mathbb{R}^4$ can then be written as

$$f = \mathbf{C}\bar{z} - \mathbf{D}z. \tag{2.37}$$

The system can also be rewritten to

$$\mathbf{A}\bar{z} = \mathbf{B}z. \tag{2.38}$$

With this notation, the interface values \bar{z} can be eliminated and the transmissibility matrix can be expressed algebraically as

$$\mathbf{T} = (\mathbf{C}\mathbf{A}^{-1}\mathbf{B} - \mathbf{D}). \quad (2.39)$$

The matrix $\mathbf{T} \in \mathbb{R}^{4 \times 4}$ then results in the four subinterface fluxes when applied to the four unknowns z of the interaction regions,

$$f = \mathbf{T}z. \quad (2.40)$$

The total flux into a primary grid cell is given by the sum over the subfluxes making up its interface. The transmissibility matrices of all interaction regions can be precomputed given that the grid geometry and diffusivity field is constant. The reconstruction of the fluxes only requires a matrix vector product to produce the local fluxes during runtime which makes this method quite performant.

One disadvantage of this method is that the construction hides the implied assumptions on the effective diffusivity within the interaction region. They are not considered and stated separately, but in conjunction. In other words, the MPFA-O method makes no interpretable statement on the effective anisotropic diffusivity field within the interaction region. In Section 3 we will present a vertex-centered finite volume method that shares the advantages of the MPFA-O and extends it in this regard.

3 The Hölder finite volume method

Within this section we present a vertex-centered finite volume method for the FAAD model class introduced in Equation (2.1a). The discretization uses a matrix Hölder mean for the diffusive flux approximation. The proposed Hölder mean allows to evaluate the interpolated diffusion matrices anywhere within the discretization cells. The resulting numerical discretization is parameterized by a scalar value $\alpha \in \mathbb{R}$ which determines the behavior of the diffusivity interpolation and consequently the numerical results.

The question we sought to answer was that of which Hölder parameter α and therefore which matrix interpolation is optimal for the numerical simulation of tumor models. Although the very concrete application of PDE tumor models on DTI data sets was our focus, the question of the most accurate matrix interpolation is also relevant in other discretization schemes and applications.

For brevity we will refer to the discretization as the Hölder finite volume method (HFVM). The presented method is of Petrov-Galerkin type with a d-linear Lagrange ansatz space and a piecewise constant test space. The effects of different choices of matrix interpolation were investigated via the method of manufactured solutions (MMS), described in Section 2.6.

We begin by motivating the question of the appropriate scalar mean in a simple TPFA setting in 3.1. In Section 3.2 we then define the scalar Hölder means to formalize our notation before we extend it to the matrix Hölder mean and define the necessary weights. The combination of the weights and the averages allows explicit expressions of how the diffusivity fields may be evaluated in between datapoints, everywhere within the discretization cells. We then present the discretized spatial residual of the Hölder finite volume method in Section 3.3. Finally, we present results of our numerical investigation of the method in Section 3.4. We investigated the effect of the Hölder parameter $\alpha \in \mathbb{R}$ for four different underlying diffusivity fields.

3.1 Problem description

For the numerical simulation of GBM, one may use patient DTI data sets which express the approximate water diffusion tensors at any voxel within a given data set. The discrete data sets approximate the real underlying inhomogeneous anisotropic permeability fields. From this water diffusivity field, one may reconstruct the approximate diffusion of the tumor cells: $\mathbf{D}_t(x) \in \mathbb{R}^{d \times d}$.

The discretization of anisotropic inhomogeneous diffusion processes on real world data sets poses challenges in the numerical treatment because the underlying data sets may include jumps in diffusivity spanning many orders of magnitude. Another aspect is that the preferred direction of diffusivity may change rapidly from datapoint to datapoint. Omitting advective and reactive terms in Equation (2.1a), we focus our problem description on the anisotropic diffusion of the tumor density. The governing equation is given by Fick's first and second law.

Definition 3.1.1 (*Fick's diffusive flux law*)

Let $u(x, t) : \Omega_b \times T \rightarrow \mathbb{R}$ be a tumor density and $\mathbf{D}(x) : \Omega_b \rightarrow \mathbb{R}^{d \times d}$ the diffusive material properties, then Fick's combined first and second law state that

$$\frac{\partial u(x, t)}{\partial t} = \nabla \cdot (\mathbf{D}(x) \nabla u(x, t)). \quad (3.1)$$

The underlying question is how this diffusive flux is best discretized with finite data set resolutions, where purely numerical grid refinement can not be expected to produce more precise results. Finite volume discretizations can be derived by multiplying Equation (3.1) with a piecewise constant test function v , integrating over small control volumes τ_i and re-expressing the volume integral of the right hand side as a surface integral via the Gauss theorem

$$\frac{d}{dt} \int_{\tau_i} u(x, t) v \, dx = \oint_{\partial \tau_i} (\mathbf{D}(x) \nabla u(x, t)) v \cdot n \, dS. \quad (3.2)$$

In polygonal conforming grids, the right hand side can be further divided down into a sum of integrals over simple geometric surfaces. The simplest of such flux reconstructions is the two point flux approximation (TPFA). In this construction a piecewise constant base is chosen to approximate the density within each cell $\tau_i \in \mathcal{T}_h$. The TPFA flux expression can be analytically derived by first demanding, that the flux density constructed has to be consistent at the adjacent cell's boundary and secondly, that the density has to be

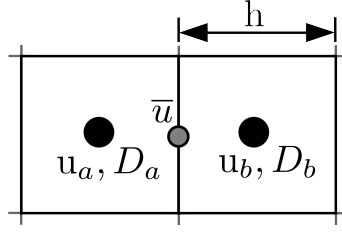


Figure 9: Schematic of a flux discretization based on the TPFA method between two cells A, B with diffusion coefficients $D_a, D_b \in \mathbb{R}$ and densities $u_a, u_b \in \mathbb{R}$. In the TPFA method the material properties are modeled to be constant within a cell resulting in a discontinuity at the interface (grey dot), for which different averages are possible.

continuous at that interface. To give a direct example of this we define two adjacent cells A, B with degrees of freedom $u_a, u_b \in \mathbb{R}$, scalar diffusivities $D_a, D_b \in \mathbb{R}$ and a shared tumor density value $\bar{u} \in \mathbb{R}$ at their interface (see Fig. 9). We demand consistency of the flux densities $f = \mathbf{D}(x)\nabla u(x, t)$ at the interface, so that

$$f_{A \rightarrow B} = f_{B \rightarrow A}, \quad (3.3)$$

where $f_{A \rightarrow B}$ denotes the flux approximation from cell $A \in \tau_h$ to cell $B \in \tau_h$. The flux approximation from both sides then reads

$$D_a \frac{\bar{u} - u_a}{\frac{h}{2}} = -D_b \frac{\bar{u} - u_b}{\frac{h}{2}}. \quad (3.4)$$

From this equation the density value at the interface can be calculated as

$$\bar{u} = \frac{D_a u_a + D_b u_b}{D_a + D_b} \quad (3.5)$$

and after re-insertion of (3.5) into (3.4) one finds that the flux density has to be

$$f_{A \rightarrow B} = \underbrace{\frac{2}{D_a^{-1} + D_b^{-1}}}_{\text{harmonic average}} \underbrace{\frac{u_b - u_a}{h}}_{\text{discrete gradient}}, \quad (3.6)$$

where we identified the diffusivity average at the interface and a canonical gradient discretization. In this basic example, the contributions to the flux integral (3.2) are discretized by a midpoint rule at each interface, taking a canonical gradient discretization at the interface midpoints and using a *harmonic average* of the diffusivities of the two adjacent cells. The harmonic average will force the flux to zero if any of the two material diffusivities D_a, D_b is impermeable. This average is known to be superior to an arithmetic mean of

the two diffusivities, especially in the presence of strong discontinuities (Droniou, 2014). The question of whether this choice is *optimal* is discussed in (Liu and Ma, 2004). The flux is also symmetric by construction. Because of this symmetry, the resulting numerical method will be discretely mass preserving. This two-point flux approximation is sufficient, as long as the diffusive properties are isotropic so that the diffusion coefficients associated with the cells are scalars.

However, if the underlying material is anisotropic, the diffusive properties have to be expressed by a diffusivity matrix $\mathbf{D}(x) \in \mathbb{R}^{d \times d}$ with possibly off-diagonal entries. In this case, we may find two different anisotropic materials on both sides of a connecting face and it is not obvious how the flux across a control volume surface ought to be constructed. The presented two-point gradient discretization approximates the gradient in the direction perpendicular to the cell surface. If $\mathbf{D}(x)$ includes off-diagonal entries, the gradient amplitude parallel to the cell surface needs to be defined to calculate all contributors to the flux density $\mathbf{D}(x)\nabla u(x, t)$. The two point gradient approximation across the interface would lead to a flux discretization which, in the worst case, disregards these off-diagonal entries completely. Further, it is not clear which choice of average between the two diffusivity matrices is an appropriate choice at the interface.

The problem of the gradient discretization can be solved by including more degrees of freedom from the neighboring cells into the gradient reconstruction, hence the name multipoint flux approximation (MPFA). The question of the appropriate matrix averaging method in the flux reconstruction is more involved and is the subject of the numerical investigations we present shortly.

3.2 Diffusivity averaging

We will now reformulate assumptions that are made in the diffusivity averaging in a more general framework. We begin by formulating the harmonic average of the TPFA method in the language of Riemann manifolds. We rely in large parts on the results of (Moakher, 2005; Dryden et al., 2009), who studied different matrix means in depth. The notation via Riemann manifolds is overly complex in the TPFA homogeneous cases, but allows us to extend the formulation directly to inhomogeneous and anisotropic media.

3.2.1 Scalar averaging in flux discretizations

In the following, a scalar framework for averaging diffusivities within discretization cells is presented. We assume that the diffusivities are given at the vertices of the primary grid \mathcal{T}_h , and present an expression how to calculate meaningful approximations in between data points.

Definition 3.2.1 (Scalar Hölder mean)

For a given set of scalar vertex diffusivities $\mathcal{D} = \{D_1, \dots, D_{N_v}\}$ with $D_i \in \mathbb{R}_+$ and $N_v \in \mathbb{N}$ as the number of vertices of cell $\tau_j \in \mathcal{T}_h$, we define the scalar Hölder mean value $D_\alpha(x) \in \mathbb{R}$ at any $x \in \tau_j$ with the scalar weights $w_i(x) : \mathbb{R}^d \rightarrow \mathbb{R}$ as

$$\begin{aligned} D_\alpha(x) &= \left(\arg \min_{D'} \sum_{i=1}^{N_v} w_i(x) d_\alpha(D', D_i)^2 \right)^{\frac{1}{\alpha}} \\ &= \left(\sum_{i=1}^{N_v} w_i(x) D_i^\alpha \right)^{\frac{1}{\alpha}}, \end{aligned} \quad (3.7a)$$

$$d_\alpha(a, b) = |a^\alpha - b^\alpha| \quad \text{with } \alpha \in \mathbb{R}; a, b \in \mathbb{R}_+, \quad (3.7b)$$

$$\sum_{i=1}^{N_v} w_i(x) = 1, \quad \forall x \in \tau_j. \quad (3.7c)$$

Expression (3.7a) selects that representative $D_\alpha(x) \in \mathbb{R}_+$ which minimizes the sum of distances given by the metric $d_\alpha(\cdot, \cdot)$ from the set of vertex diffusivities (Dryden et al., 2009). One of the main practical advantages of the Hölder means is, that this minimum can be directly computed everywhere within the primary grid cell τ_j . The Hölder parameter $\alpha \in \mathbb{R}$ controls the exact distance metric and therefore also the resulting average value. Here, $w_i(x) : \mathbb{R}^d \rightarrow \mathbb{R}$ are the scalar weights of the contributors which we define shortly. This framework is not strictly necessary in simple low dimensional cases, but will provide more context when we extend it to SPD matrices and higher dimensions in Section 3.2.2. The distance metric $d_\alpha(\cdot, \cdot)$ is the generalization of the standard Euclidean distance. Expression (3.7a) generalizes many ways to average a number of scalar values with given weights. For certain values of $\alpha \in \mathbb{R}$ the Hölder mean coincides with well known means in

the following way:

$$\textbf{minimum: } \alpha \rightarrow -\infty \quad D_\alpha = \min(w_1 D_1, \dots, w_{N_v} D_{N_v}), \quad (3.8a)$$

$$\textbf{harmonic mean: } \alpha = -1 \quad D_\alpha = \left(\sum_i^{N_v} \frac{w_i}{D_i} \right)^{-1}, \quad (3.8b)$$

$$\textbf{log-Euclidic mean: } \alpha \rightarrow 0 \quad D_\alpha = e^{\left(\sum_i^{N_v} w_i \ln(D_i) \right)} \quad \text{with } w_i = \frac{1}{N_v}, \quad (3.8c)$$

$$\textbf{geometric mean: } \alpha = 0 \quad D_\alpha = \prod_{i=1}^{N_v} D_i^{w_i}, \quad \text{with } w_i = \frac{1}{N_v}, \quad (3.8d)$$

$$\textbf{arithmetic mean: } \alpha = 1 \quad D_\alpha = \sum_{i=1}^{N_v} w_i D_i, \quad \text{with } w_i = \frac{1}{N_v}, \quad (3.8e)$$

$$\textbf{maximum: } \alpha \rightarrow \infty \quad D_\alpha = \max(w_1 D_1, \dots, w_{N_v} D_{N_v}). \quad (3.8f)$$

Here N_v is the number of contributing vertex values $D_i \in \mathcal{D}$. We added the log-Euclidian mean, which is equivalent to the geometric mean for later reference (Crawley, 2014). The scalar Hölder mean satisfies the following inequality.

Remark 3.2.1 (*Power mean inequality*)

For a given set of vertex diffusivities $\mathcal{D} = \{D_1, \dots, D_{N_v}\}$, the two Hölder means D_α with $\alpha = a, b$ follow the power mean inequality

$$\min(\mathcal{D}) \leq D_a \leq D_b \leq \max(\mathcal{D}), \quad \text{with } a, b \in \mathbb{R}; a < b \quad (3.9)$$

For a proof of this inequality in the scalar case we refer to (Bullen, 2003). The stated inequality has direct implications for the flux discretizations, as the concrete choice of α may result in systematic over- or underestimation of the diffusivity at the control volume surfaces and thereby the flux integrals. This effect is most relevant where we expect strong fluctuations of diffusivity including regions of diminishing diffusivity. Figure 10 shows a schematic of what effect the parameter α has on the interpolated diffusivities in-between 3 exemplary datapoints. Here, the interpolation results from employing linear weights $w(x)$ in between any two datapoints and calculating the mean accordingly. For negative values of α the flux is effectively suppressed in case one of the two contributors D_i is small. This case is visible in the right side of Figure 10. With this notation, we may rephrase the result from (Aavatsmark, 2002) and state that a good choice of diffusivity mean in isotropic TPFA finite volume methods is the Hölder mean with $\alpha = -1$, i.e. the harmonic

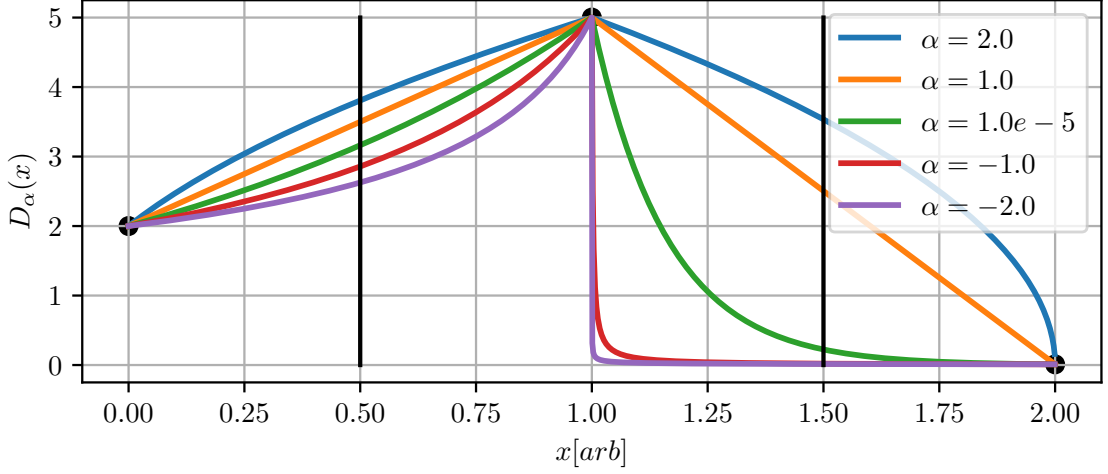


Figure 10: 1D schematic of scalar Hölder diffusivity interpolation $D_\alpha(x)$ for different Hölder parameters between the datapoints $D(0) = 2$, $D(1) = 5$ and $D(2) = 10^{-2}$ shown as black dots. Vertical black lines mark midpoints between datapoints at which the flux is often integrated. We employ linear weights $w(x)$ in between any two datapoints. The influence of the choice of $\alpha \in \mathbb{R}$ is especially pronounced where one contributor D_i diminishes as seen on the right hand side.

mean given in Equation (3.8b).

3.2.2 Matrix Hölder mean

In the case where the diffusivity field is a set of symmetric positive definite (SPD) matrices, we can use an extension of the scalar Hölder mean (3.7a) to matrices. Introducing the manifold of symmetric $n \times n$ SPD matrices $\text{Sym}^+(n)$ with the Frobenius inner product $\langle \mathbf{A}, \mathbf{B} \rangle = \text{tr}(\mathbf{A}^T \mathbf{B})$ and the induced norm $\|\mathbf{A}\|_F = \sqrt{\langle \mathbf{A}, \mathbf{A} \rangle}$ we now define the corresponding Hölder mean in analogy to Definition (3.2.1). We follow the notation of (Dryden et al., 2009; Bhagwat and Subramanian, 1978), where the following mean is introduced as ‘power-euclidian’.

Definition 3.2.2 (Matrix Hölder mean)

For a given set of vertex diffusivities $\mathcal{D} = \{\mathbf{D}_1, \dots, \mathbf{D}_{N_v}\}$ with $\mathbf{D}_i \in \text{Sym}^+(d)$ of cell $\tau_j \in \mathcal{T}_h$ we define the matrix Hölder mean $\mathbf{D}_\alpha(x) : \mathbb{R}^d \rightarrow \mathbb{R}^{d \times d}$ at any $x \in \tau_j$ with the scalar weights

$w_i(x) : \mathbb{R}^d \rightarrow \mathbb{R}$ as

$$\mathbf{D}_\alpha(x) = \arg \min_{\mathbf{D}'} \left(\sum_{i=1}^{N_v} w_i(x) d_\alpha(\mathbf{D}', \mathbf{D}_i)^2 \right)^{\frac{1}{\alpha}} = \left(\sum_{i=1}^{N_v} w_i(x) \mathbf{D}_i^\alpha \right)^{\frac{1}{\alpha}}, \quad (3.10a)$$

$$d_\alpha(\mathbf{A}, \mathbf{B}) = \|\mathbf{A}^\alpha - \mathbf{B}^\alpha\|_F, \quad \forall \mathbf{A}, \mathbf{B} \in \text{Sym}^+(d), \quad (3.10b)$$

$$\sum_{i=1}^{N_v} w_i(x) = 1. \quad (3.10c)$$

The matrix Hölder mean again selects that matrix \mathbf{D}_α that minimizes the sum of the distances d_α to the contributors $\mathbf{D}_i \in \mathcal{D}$. We defined the matrix power in Equation (2.24). Dryden et al. (2009) state that the matrix Hölder mean becomes more resistant to outliers for small positive α , while the influence of outliers is increased for $\alpha \gg 0$. For the special case of $\alpha = 1$ we find the component-wise linear interpolation that is used in many production codes. However, this choice is problematic, because the arithmetic matrix mean is known to have a swelling effect where the determinant of the interpolant can be larger than the determinants of the other contributors (Arsigny et al., 2007). When the interpolated matrices are associated with covariance matrices, as is the case for diffusion matrices describing brownian motion, then the swelling of the determinant would correspond to an unphysical increase in total dispersion (Arsigny et al., 2007). For $\alpha = -1$ we find, analogously to the scalar case, a mean that diminishes whenever the Frobenius norm of one of the contributing \mathbf{D}_i is zero. For $\alpha \rightarrow 0$ it is known that the Hölder mean approaches the log-Euclidian mean (Dryden et al., 2009). It is defined as follows.

Definition 3.2.3 (Log-Euclidian mean)

For a given set of vertex diffusivities $\mathcal{D} = \{\mathbf{D}_1, \dots, \mathbf{D}_{N_v}\}$ and $\mathbf{D}_i \in \text{Sym}^+(n)$ of cell $\tau_j \in \mathcal{T}_h$ we define the matrix Hölder-mean value $\mathbf{D}_\alpha(x) \in \mathbb{R}^{d \times d}$ at any $x \in \tau_j$ with the scalar weights $w_i(x) \in \mathbb{R}$ as

$$\mathbf{D}_\alpha = \exp \left(\arg \min_{\mathbf{D}'} \sum_{i=1}^{N_v} w_i d_{\text{Log}}(\mathbf{D}', \mathbf{D}_i)^2 \right) = \exp \left(\sum_{i=1}^{N_v} w_i \ln(\mathbf{D}_i) \right), \quad (3.11)$$

$$d_{\text{Log}}(\mathbf{A}, \mathbf{B}) = \|\ln(\mathbf{A}) - \ln(\mathbf{B})\|_F \quad (3.12)$$

The above definition uses matrix-exponentiation and matrix-logarithm, which we defined in (2.22) and (2.23) (Dryden et al., 2009; Bhagwat and Subramanian, 1978; Audenaert and

Hiai, 2013). There is some discussion in the literature whether the mean for $\alpha \rightarrow 0$, i.e., the log-Euclidian mean can be seen as the extension of the scalar geometric mean and what properties a matrix-geometric mean should have (Moakher, 2006; Arsigny et al., 2007). It was also investigated by Arsigny et al. (2007) which mean might be appropriate for the reconstruction of DTI data sets. They suggest to use a log-Euclidian interpolation.

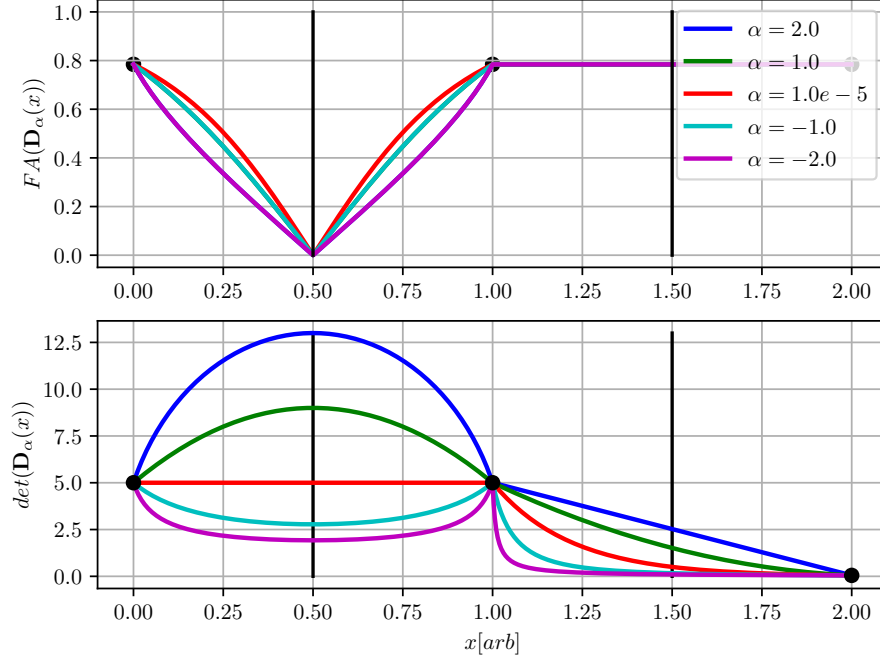


Figure 11: Visualization of the Fractional Anisotropy (FA) and determinant of Hölder-interpolated matrices along three datapoints, with linear weights. The three matrices are: $\mathbf{D}(0) = \begin{pmatrix} 5 & 0 \\ 0 & 1 \end{pmatrix}$, $\mathbf{D}(1) = \begin{pmatrix} 1 & 0 \\ 0 & 5 \end{pmatrix}$, $\mathbf{D}(2) = \begin{pmatrix} 0.1 & 0 \\ 0 & 0.5 \end{pmatrix}$. Vertical black lines mark midpoints between datapoints at which the flux is often integrated. The sample matrices are rotated between the first and the second datapoint, and linearly scaled in amplitude between the second and the third. A swelling of the determinant is visible for $\alpha \geq 0$ between datapoints 1 and 2.

Definition of weights

In order to make use of the general form of the introduced Hölder means, the weights $w_i(x) \in \mathbb{R}$ used in equations (3.10a, 3.11) need to be specified. We assume that the diffusion matrices are given at the nodes of the primal grid cells. We choose the weights

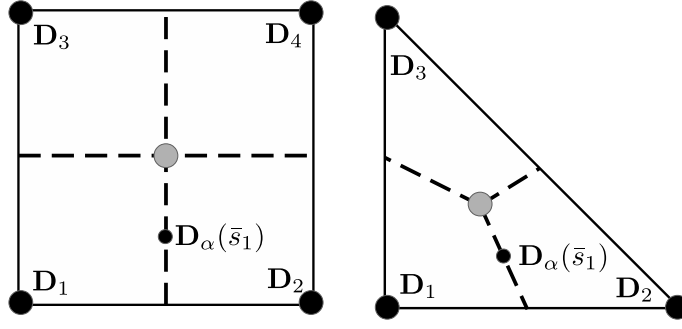


Figure 12: Quadrilateral and simplicial element with degrees of freedom (black dots) resting on the edges, dashed lines indicate dual grid subinterfaces connecting the center of mass (grey dots) with the primal grids interface midpoints. The small dots indicate two sample subinterface midpoints $\bar{s}_1 \in \mathbb{R}^d$ where the diffusion matrix $\mathbf{D}_\alpha(x)$ may be evaluated for subflux discretization.

to be the evaluation of the d-linear basis functions for the given data points introduced in Equation (2.17a). In our case of a hexahedral grid this is the canonical Q_1 Lagrange base.

Definition 3.2.4 (Hölder weights)

Let $\mathbf{D}_i \in \mathcal{D}$ be a contributor in the Hölder mean $\mathbf{D}_\alpha(x)$ with $x \in \tau_j$ (3.10a). We then define the corresponding weight as the evaluation of the Lagrange base function $\phi_i(x) : \mathbb{R}^d \rightarrow \mathbb{R}$ as defined in Equation (2.17a).

$$w_i(x) = \phi_i(x). \quad \forall x \in \tau_j, i = 1, \dots, N_v \quad (3.13)$$

The interpolation is later evaluated at the subinterface midpoints but evaluation at any other point within the cells would lead to reasonable interpolants. Figure 12 illustrates how the Hölder mean may be evaluated at the subinterface midpoints within the primary grid cell. The choice $w_i(x) = \phi_i(x)$ is suitable, as it provides for the weights at the data points to be 1 (see Eq. (2.17c)) and also ensures that the sum of the weights equal one irrespective of where the Hölder mean is evaluated within the primal cell (see Eq. (2.17b)). It therefore provides a geometrically intuitive weight in the area between the data points. These arguments can be generalized to 3D as well as tetrahedral cell geometries.

3.3 Hölder finite volume method

We will now derive the fully discretized approximation to the spatial residual $r^s(u, v)$ introduced in Equation (2.4). We recall that the test function $v \in V_h$ is piecewise constant on each *dual* grid cell and begin by subdividing the global residual integration over the dual grid tessellation,

$$r^s(u, v) = \sum_{i=1}^{N_d} \left(v \int_{\chi_i} \nabla \cdot ((\mathbf{D} \nabla u) + bu) \, dx + \int_{\chi_i} f(u)v \, dx \right), \quad (3.14)$$

where we pulled $v \in V_h$ out of the integral. We apply the Gauss theorem for the flux terms to express them as a surface integral

$$r^s(u, v) = \sum_{i=1}^{N_d} \oint_{\partial\chi_i} ((\mathbf{D} \nabla u) + bu)v \cdot n \, dS + \int_{\chi_i} f(u)v \, dx, \quad (3.15)$$

where n denotes the outer unit normal. The application of the Gauss theorem over the dual grid cells χ_i indicates the finite volume character of this method. We shortly define symmetric fluxes over the surfaces of the dual grid cells via the subinterfaces, and therefore may expect discrete mass conservation for the discretization of the diffusive and advective terms assuming $\nabla \cdot b(x) = 0$.

Since we may rearrange the summation of the global residual, we will collect all residual contributions of a single *primal* grid cell $\tau_k \in \mathcal{T}_h$ and denote them by $r_k^s(u, v)$. This notation will slightly obfuscate how the discrete mass conservation is achieved. In this notation, the control volumes encased by the dual grid surfaces are not as obvious as in notations of other finite volume methods. However, this notation is more expressive than maintaining summation over contributions from both tessellations, and is closer to the actual implementation. The residuum contribution from a primary grid cell is given by

$$r_k^s(u, v) = \int_{\Gamma_k} ((\mathbf{D} \nabla u) + bu)v \cdot n \, dS + \int_{\tau_k} f(u)v \, dx. \quad (3.16)$$

The flux integral is no longer encasing a full dual grid cell surface (control volume) as we now integrate over the dual grid skeleton Γ_k overlapping the primal grid, defined in Equation (2.11). This is without detriment. We break the integrals into even smaller parts by summing the flux integrals over all subinterfaces $s_i \in \mathcal{S}$ within τ_k and the volume

integrals over all subvolumes $\theta_j \in \Theta$,

$$r_k^s(u, v) = \sum_{i=1}^{N_s} \int_{s_i} (\mathbf{D} \nabla u + bu)v \cdot n \, dS + \sum_{j=1}^{N_\theta} \int_{\theta_j} f(u)v \, dx. \quad (3.17)$$

Here N_s, N_θ are the number of subinterfaces and subvolumes within τ_k . We recall the piecewise d-linear approximation of the tumor density $u_h(x) = \sum_{l=1}^{N_d} u_l \phi_l(x)$ on the primary grid from Equation (2.18) and the piecewise constant representation of the test function $v_h(x) = \sum_{m=1}^{N_d} \xi_m(x)$ on the dual grid. We now express (3.17) via theses finite dimensional bases (see Eqs. (2.18, 2.19)).

$$\begin{aligned} r_k^s(u_h, v_h) &= \sum_{i=1}^{N_s} \sum_{l=1}^{N_v} \sum_{m=1}^{N_v} \int_{s_i} (\mathbf{D}(x) (z_l \nabla \phi_l(x))) + b(x) z_l \phi_l(x) \xi_m(x) \cdot n \, dS \\ &\quad + \sum_{j=1}^{N_\theta} \sum_{m=1}^{N_v} \int_{\theta_j} f \left(\sum_{l=1}^{N_v} z_l \phi_l(x) \right) \xi_m(x) \, dx. \end{aligned} \quad (3.18)$$

Here, the new summation iterates over all local base functions $\phi_l(x), \xi_m(x)$. We now use a midpoint rule to integrate the flux on the subinterfaces, i.e., evaluate both the diffusion tensor and the gradient at the subinterface midpoints \bar{s}_i with the subinterface area of $|A_s|$. We use a Gauss quadrature rule with quadrature points x_k and weights w'_k on the subvolumes θ of volume $|\theta|$ for the volume terms. To not complicate the notation further we assume that all subvolumes and subinterfaces are of equal size. Finally, we make use of the matrix Hölder mean $\mathbf{D}_\alpha(\bar{s}_i)$ to estimate the diffusivity tensor field at the quadrature points.

$$\begin{aligned} r_k^s(u_h, v_h) &= \sum_{i=1}^{N_s} \sum_{l=1}^{N_v} \sum_{m=1}^{N_v} ((\mathbf{D}_\alpha(\bar{s}_i) (z_l \nabla \phi_l(\bar{s}_i))) + b(x) z_l \phi_l(\bar{s}_i)) \xi_m(\bar{s}_i) \cdot n \, |A_s| \\ &\quad + \sum_{m=1}^{N_v} \sum_{k=1}^{N_v} f \left(\sum_{l=1}^{N_v} z_l \phi_l(x_k) \right) w'_k \xi_m(x_k) \, |\theta|. \end{aligned} \quad (3.19)$$

Remark 3.3.1 *Special attention has to be paid to the sign of the subinterface normals. In the actual assembly of the numerical residual vector one should take care to implement the normals as outward pointing from the perspective of the subvolume which is assembled.*

3.4 Numerical convergence results

The presented HFVM method was numerically investigated to study the effect of the Hölder parameter $\alpha \in \mathbb{R}$. We employed the technique of manufactured solutions as introduced in Section 2.6. We now present the convergence results of the HFVM in comparison to the MPFA-O method and a conforming finite element method (CFEM) for selected parameterizations of the manufactured solution. The MPFA-O method was described in Section 2.7. The CFEM method uses a Q_1^2 Lagrange base on the primary grid. In our numerical setup, the finite element method evaluated the underlying diffusivity field *analytically* and should be seen as a gold standard and not a fair competitor. For the test with inhomogeneous isotropic diffusion and the one with homogeneous anisotropic diffusion perfect second order convergence was observed, for all schemes we implemented. The considered parameterizations of the manufactured solution each focus on one particular aspect of difficulty of the underlying data set. For the sake of conciseness, we omit the simplest case of homogeneous isotropic diffusion as it does not present additional information. The simulations were conducted on a square domain discretized with a quadrilateral mesh, which is successively refined from 32^2 to 1024^2 cells. We present the L_2 -errors (2.6.1) plotted against the mesh size $h \in \mathbb{R}$. Table 4 gives an overview of the four considered test cases.

Homogeneous	Isotropic	Description	Section
✗	✓	diffusivity varies in amplitude	3.4.1
✓	✗	hom. directional preference	3.4.2
✗	✗	rotating directional preference	3.4.3
✗	✗	fully inhomogeneous	3.4.4

Table 4: Overview of the considered test cases in the following sections. The test most relevant to the tumor simulation is the one in Section 3.4.3, where the dominant direction of diffusion rotates much like within curved fiber bundles.

We want to draw special attention to the case presented in Section 3.4.3, where the diffusivity stays constant in its Frobenius norm and determinant, but the preferred direction of diffusive transport is rotating. Within the human brain there are white matter tracts consisting of fiber bundles. Within these bundles we may expect that the diffusivity in the fiber directions and the perpendicular directions remains mostly constant in space, but the orientation of these white matter tracts may change. It is known that glia-cells,

and therefore also the cancer cells, migrate predominantly along these tracts (Giesse and Westphal, 1996; Gritsenko et al., 2012; Engwer et al., 2015, 2016). For the simulation of GBM it is therefore most important how well a chosen numerical method responds to underlying diffusivity fields of this kind. We chose that value of α which performed best within this numerical test for all subsequent two and three dimensional GBM simulations. We now present the convergence results for the four different parameterizations of the manufactured solution.

3.4.1 Inhomogeneous isotropic case (eigenvalue)

In this test we consider an isotropic inhomogeneous diffusion field $\mathbf{D}_a(x)$ which simply varies in the eigenvalues of the permeability (inhomogeneous) throughout the domain, but has no preferred direction (isotropic). In this simple case, a TPFA discretization would still produce reasonable results as there are no off-diagonal entries within the diffusion tensor field.

Parameter	Value
p_d	2
p_β	0
a_{xx}	10^{-10}
a_{yy}	10^{-10}

Table 5: Altered parameters of the manufactured solution defined in Section 2.6 for the inhomogeneous isotropic test case. The fixed parameters were listed in Table 3.

Figure 13 shows the L2-error of different numerical discretizations for the manufactured solution at successively reduced cell spacings. A linear and a quadratic function are provided for orientation. The log-Euclidian Hölder interpolation produces slightly better results than other Hölder methods and the MPFA-O method. The CFEM and DG method use the *analytical* diffusivity field (gold standard). All implemented methods show perfect second order convergence.

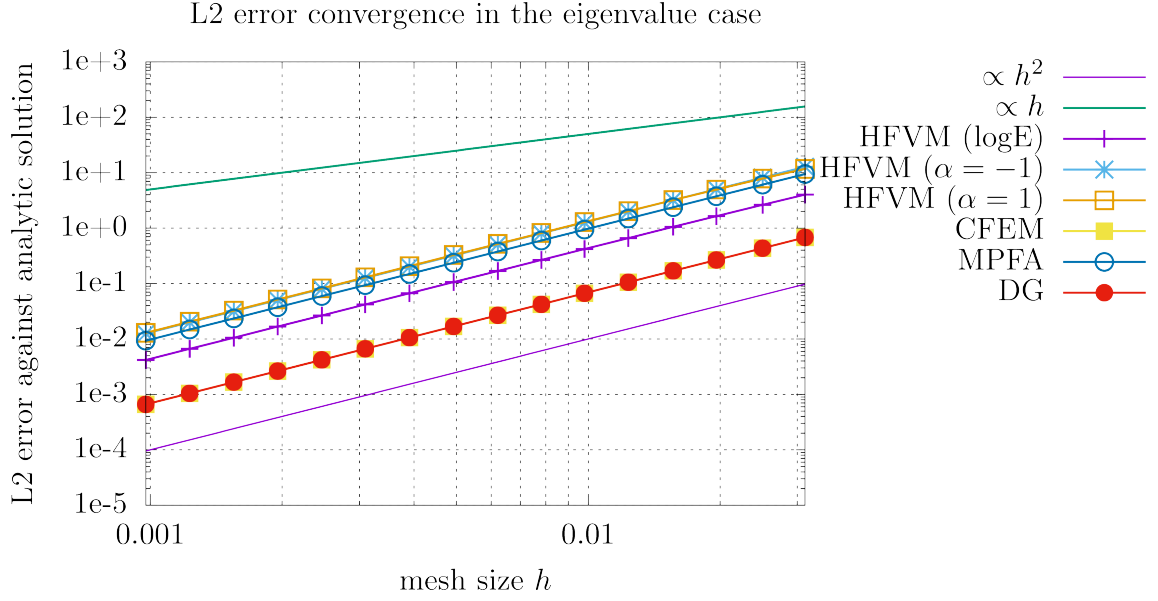


Figure 13: Inhomogeneous isotropic case (eigenvalue variation): convergence of global L2-error over grid spacing h . Expected convergence order 2 is observed for all discretization methods. We denote the Hölder interpolation with $\alpha \rightarrow 0$ with 'logE'. The grid resolution sufficiently resolves the manufactured solution and diffusivity throughout all refinements. The CFEM and discontinuous galerkin (DG) discretizations use analytic evaluations of $\mathbf{D}_a(x)$

With a simple solution parameterization as this, the test is essentially a convergence test that indicates correct implementation of the discretizations within the DUNE-glio module, as described in Section 5. The altered parameterization for the manufactured solution can be found in Table 5.

3.4.2 Homogeneous anisotropic case

In this numerical test, the diffusivity field of the manufactured solution is anisotropic in the sense that the diffusivity is two orders of magnitude higher in horizontal direction ($a_{xx} = 10^{-10}$) than in vertical direction ($a_y = 10^{-12}$), but is still ' K -aligned', i.e. the eigenvectors of the diffusivity matrices are aligned with the grid geometry. The altered parameters can be found in Table 6.

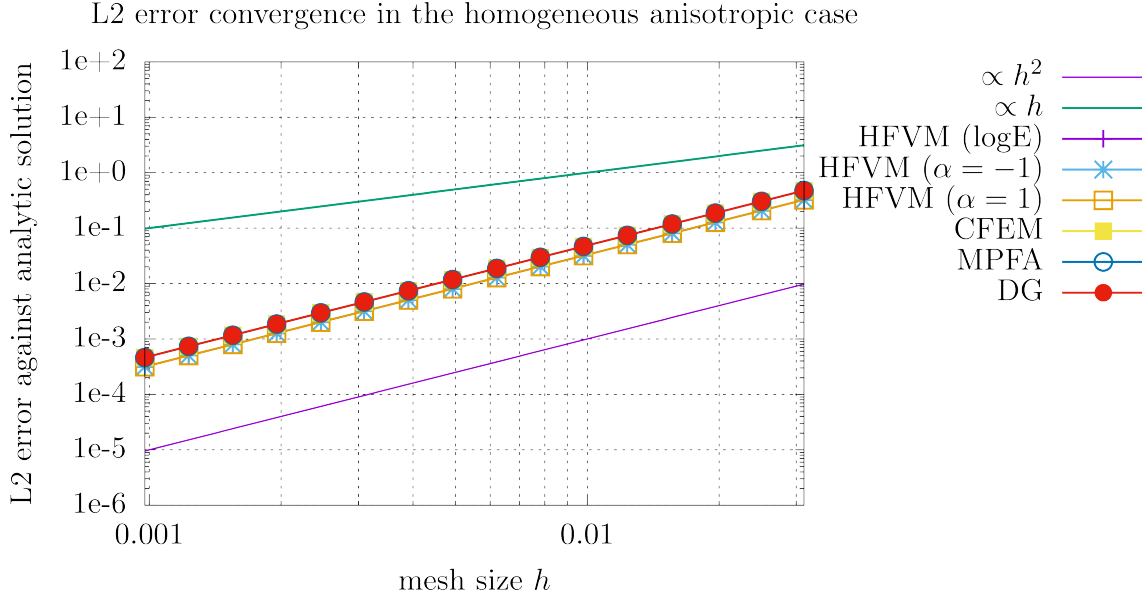


Figure 14: Homogeneous anisotropic case: convergence of global error over grid spacing h . HFVM-alpha methods are identical as no spatial variance exists in $\mathbf{D}(x)$ and therefore all matrix Hölder means result in equivalent interpolations. Expected convergence order 2 is observed for all discretization methods. The grid resolution sufficiently resolves the manufactured solution and diffusivity throughout all refinements.

Parameter	Value
p_d	0
p_β	0
a_{xx}	10^{-10}
a_{yy}	10^{-12}

Table 6: Altered parameters of the manufactured solution defined in Section 2.6 for the homogeneous anisotropic test case. The fixed parameters were listed in Table 3.

Figure 14 again presents the errors over the grid spacings. In this test case the CFEM discretization performs similarly to the finite volume methods (HFVM, MPFA-O) as no advantage is gained by analytical evaluation of \mathbf{D}_a at the quadrature points. In this corner case, all Hölder methods produce identical results.

3.4.3 Inhomogeneous anisotropic case (rotation)

In this test, we rotate the diffusivity field throughout the domain, while its principal axis amplitudes remain constant ($a_{xx} = 10^{-10}$, $a_{yy} = 10^{-12}$). Since the diffusivity field is merely rotated, the determinant and the fractional anisotropy remain constant throughout the domain. In this test, we observe drastically different errors for the different Hölder matrix interpolations.

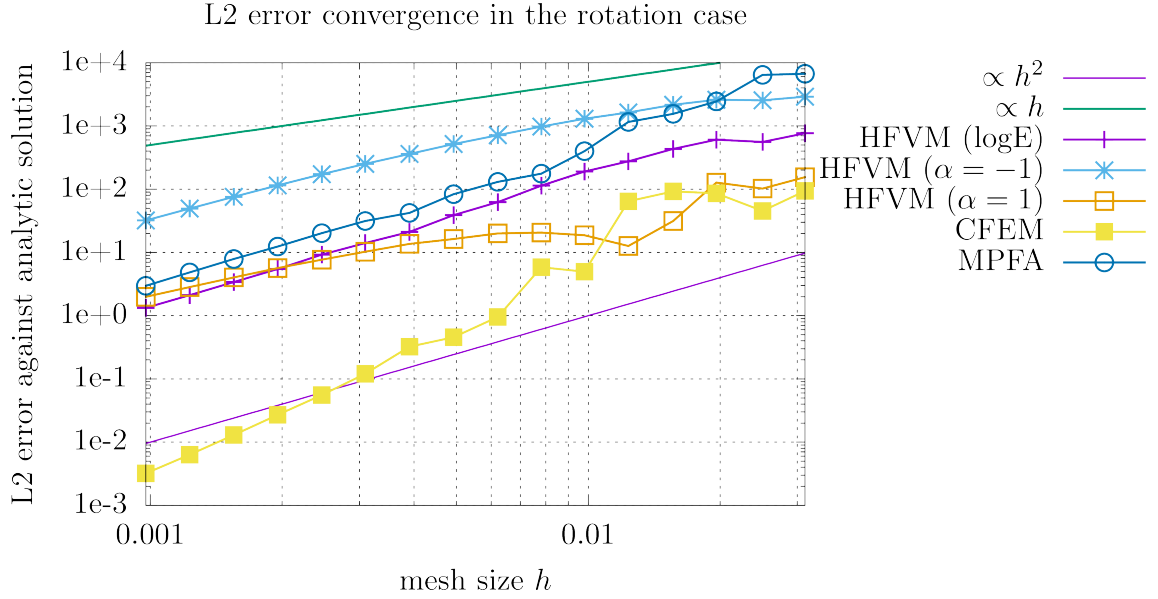


Figure 15: Inhomogeneous anisotropic case (rotation): convergence of global error over grid spacing h . Expected convergence order 2 is observed for all discretization methods in the well-resolved cases. The grid resolution sufficiently resolves the manufactured solution and diffusivity at approximately $h < 0.01$. The particular choice of Hölder average has a significant effect on the absolute errors.

Parameter	Value
p_d	0
p_β	6
a_{xx}	10^{-10}
a_{yy}	10^{-12}

Table 7: Parameters of the manufactured solution defined in Section 2.6 for the inhomogeneous anisotropic (rotation) test case.

The CFEM method we use as gold standard performs orders of magnitudes better than the methods using the matrix interpolation due to its analytical evaluation of $\mathbf{D}_a(x)$. The Hölder method with $\alpha = 1$ with its arithmetic mean performs well in the under resolved domain but shows only linear convergence rates at the highest refinements. The good performance in the underresolved cases might be due to coincidence.

In comparison to the two earlier tests Figure 15 shows increased absolute errors. The test shows that the Hölder method with $\alpha = -1$, which is the analog to the harmonic mean performs worse than the MPFA-O method. We also see that the log-Euclidian mean ($\alpha \rightarrow 0$) performs consistently better than the MPFA-O method.

3.4.4 Inhomogeneous anisotropic case (combined)

In this test the diffusivity field is inhomogeneous and anisotropic, and we combined the effects of spatially varying eigenvalues and rotations of the diffusivity field. A visual representation of the solution $u_a(x)$ and several properties of the constructed diffusivity field $\mathbf{D}_a(x)$ can be found in Figure 17.

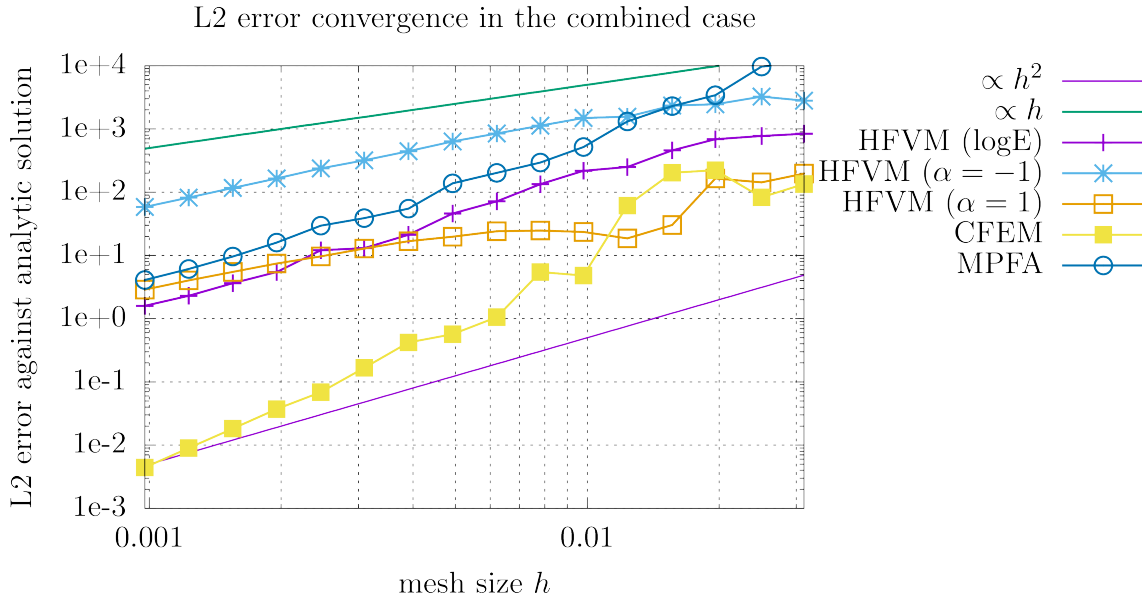


Figure 16: Inhomogeneous anisotropic case (combined): convergence of global error over grid spacing h . A convergence order between one and two is observed for the HFVM and the MPFA-O method. The log-Euclidian interpolation consistently outperforms the MPFA-O method .

Figure 16 shows similar results to the testcase with pure rotation indicating that the numerical error seems to be primarily due to the rotation of the principal axes of the diffusivity. We again find that the Hölder method with the log-Euclidian interpolation ($\alpha \rightarrow 0$) produces best results, while the interpolation for $\alpha = 1$ shows significantly higher errors.

Parameter	Value
p_d	4
p_β	6
a_{xx}	10^{-10}
a_{yy}	10^{-12}

Table 8: Parameters of the manufactured solution defined in Section 2.6 for the inhomogeneous anisotropic test case.

3.5 Conclusion

We used the method of manufactured solutions, to firstly (numerically) establish convergence and correct implementation of the considered discretizations schemes and secondly to optimize the HFVM method for our use case. We used the *a priori* information that the tumor cells migrate predominantly along white matter fiber tracks within the brain to optimize the method.

As a result we found that the Hölder finite volume method with the log-Euclidian interpolation ($\alpha \rightarrow 0$) is firstly the appropriate choice for our use case, and secondly outperforms the industry standard MPFA-O method in all considered cases. Hölder methods with $\alpha \geq 1$ suffer from the swelling effect as visible in the left side of Figure 11 and also showed unfavorable error scaling in the well resolved cases (see Figures 15, 16). It should be remarked that for the presented results, we let the conforming finite element method (CFEM) evaluate the diffusivity field *analytically* to serve as a gold standard that should be considered a lower error bound. Without this advantage the CFEM discretization performs similar to the MPFA/HFVM methods, but would be inappropriate when significant advective effects are included in the tumor models. All following two and three dimensional numerical results presented in this document have been calculated by the HFVM method with log-Euclidian interpolation ($\alpha \rightarrow 0$).

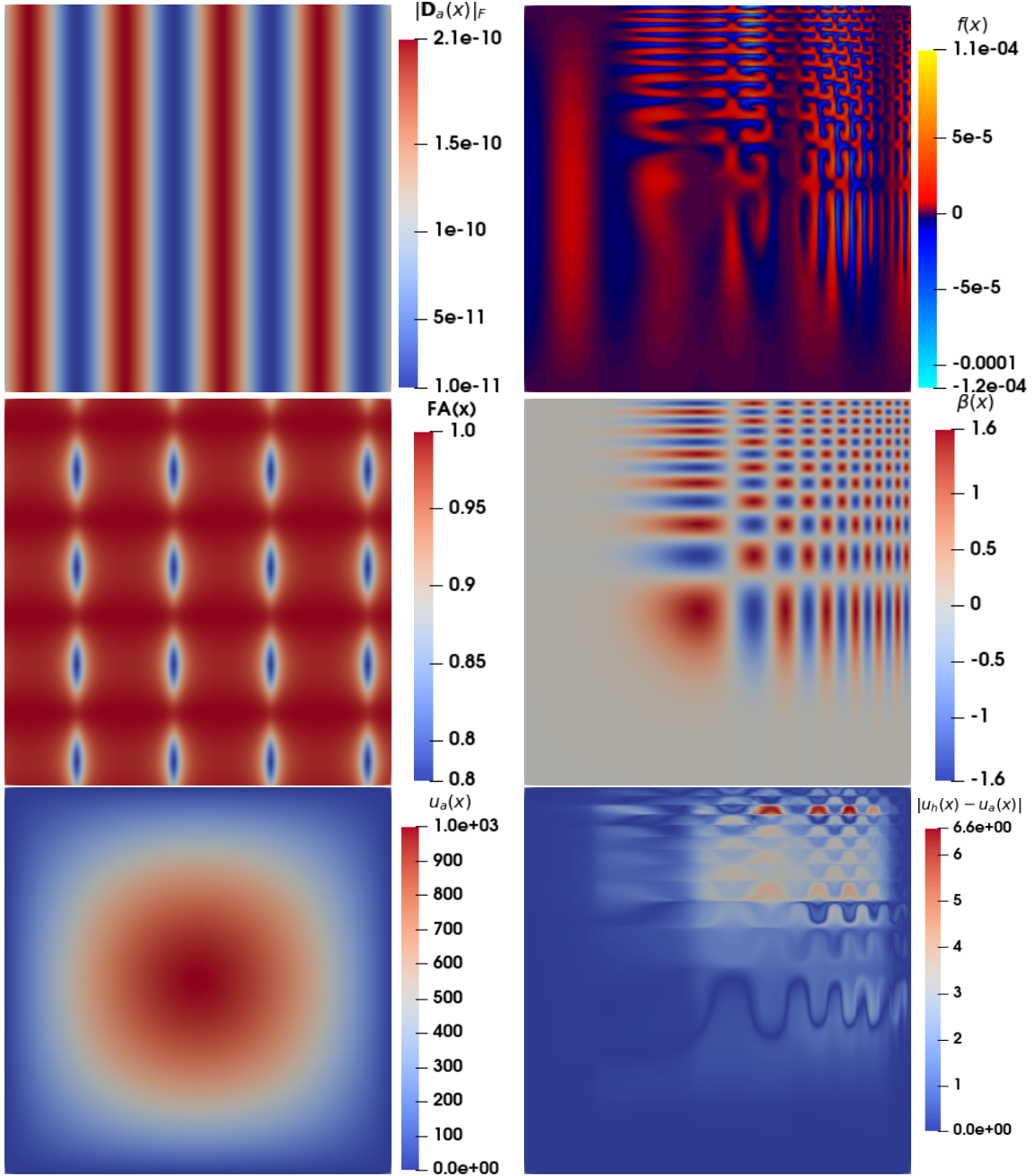


Figure 17: Visual representation of the manufactured solution properties for the spatial domain $[0, 1]^2$ with combined rotation and scaling (see Table 3). The parameterized manufactured solution, once implemented, allows to investigate different aspects of the diffusivity field influencing the numerical errors, simply by changing its parameterization. Top left: Frobenius norm of the diffusion field $\mathbf{D}_a(x)$. Top right: analytical reaction term $f(x)$ calculated from the given fields $u_a(x)$ and $\mathbf{D}_a(x)$ (2.28, 2.33). The spatial variance of the reaction term increases towards the top right of the domain. Middle left: Fractional anisotropy (Eq. (2.27)) of the diffusion field. Middle right: rotation angle of the diffusion field. Bottom Left: analytical solution $u_a(x)$. Bottom right: absolute error field for the HFVM with $\alpha \rightarrow 0$, i.e, log-Euclidian interpolation.

4 Stationalization

In the introductory Section 1.3 we discussed some of the challenges of bringing numerical modeling in tune with the available data sets. In this section we present a stationalization approach which allows us to make use of knowledge gained from the forward tumor modeling and reconcile it with the available data.

We begin by introducing three PDE forward models in Section 4.1. These are specializations of the general class of anisotropic diffusion advection reaction equations defined in Equation (2.1a). The three models can be seen as extensions of the simple Fisher-KPP equation with increasing complexity. We will later use them to investigate how well the stationalization performs for more and more complex tumor models.

We introduce a stationalization procedure in Section 4.2, which allows the approximation of the most likely state of an advancing tumor front *outside* of the region visible on medical images. We do this by deriving a nonlinear penalty term which allows the reconstruction of the infinite time limit of the Fisher-KPP equation, i.e., the shape of the propagating front. This penalty term approximates the advection term resulting from a transformation into the comoving frame in which the propagating invasion front has stationary solutions. We use that part of the tumor that is visible on the medical images as a pinning side condition in the stationary problem formulation. This stationary problem formulation is better aligned with data sets captured solely at the time of diagnosis.

We present the stationalized counterparts to the three forward models in Section 4.3. We then state how we investigated the applicability of the stationalization in 4.4. These tests are set up to determine whether or not the stationalization remains a viable approximation to the tumor front in the presence of anisotropy and advective terms. In Section 4.5 we present the results of the numerical investigation.

This part of the document contains previous work on the subject from the publication Engwer and Wenske (2020). The derivation via the limit solution of the Fischer equation is reproduced from there, and the subsequent numerical tests are set up similarly with some extensions.

4.1 Forward tumor models

We now state the three specializations of the anisotropic advection diffusion equation (2.1a). We first state the well studied Fisher-KPP equation. We then define a myopic diffusion model that incorporates inhomogeneous diffusion and myopic drift terms. Finally we state a tumor model which includes inhomogeneous diffusion, the myopic drift terms as well as haptotactic effects (Engwer et al., 2015, 2016). These three models belong to the group of anisotropic advection diffusion reaction equations and differ merely in their definition of advective effects or recognition of anisotropy.

4.1.1 1D Fisher-Kolmogorov-Petrovsky-Piscounov equation

The simplest variant of Equation (2.1a) which is still interpretable as a tumor model is the one-dimensional Fisher-KPP equation. In it the material properties are assumed to be isotropic and homogeneous and no advective effects are included. The Fisher equation is a special case of the more general Kolmogorov-Petrovsky-Piscounov (KPP) model (Kolmogoroff et al., 1988; Fischer, 1937). The model combines a diffusive term, which may be interpreted as a passive spread of the cells due to a random walk, and a logistic proliferation term, as often encountered in biological contexts.

Definition 4.1.1 (1D Fisher-Kolmogorov-Petrovsky-Piscounov Equation)

Let $x \in \mathbb{R}$ be spatial coordinate, $t \in T = [t_0, t_e] \subset \mathbb{R}$ a temporal coordinate, $u(x, t) : \mathbb{R} \times T \rightarrow \mathbb{R}$ a tumor density, $\rho \in \mathbb{R}$ the logistic growth rate and $D \in \mathbb{R}$ a scalar homogeneous diffusion constant. In the one-dimensional Fisher-KPP equation we seek $u(x, t)$ so that

$$\frac{\partial u(x, t)}{\partial t} = D \Delta u(x, t) + \rho u(x, t)(1 - u(x, t)) \quad \forall (x, t) \in \mathbb{R} \times T. \quad (4.1)$$

Many tumor models can be seen as extensions of this prototype diffusion reaction equation. It is also used to describe other propagating fronts, e.g., in the context of chemical reactions, or wildfire modeling.

Properties of the Fisher-KPP equation

We will now reproduce some of the facts that are known about the one-dimensional Fisher-KPP equation. For the initial conditions

$$\lim_{x \rightarrow -\infty} u(x, t_0) = 1, \quad \lim_{x \rightarrow \infty} u(x, t_0) = 0,$$

the Fisher equation allows traveling wave solutions (Kolmogoroff et al., 1988). These solutions converge over asymptotically long timescales to a wave front which is constant in shape, moving laterally with a globally constant limit velocity $v \in \mathbb{R}$.

For large times t , the temporal dynamics are dominated by lateral advection, and scarcely by changes of the invasion profiles shape. The formation of these traveling fronts happens quite rapidly, with only miniscule corrections to its shape at larger times. We will later make use of precisely this property.

In higher spatial dimensions, the Fisher-KPP equation has related sigmoid-like traveling wave solutions with spherically shaped expansion.

There are also less obvious stable wave front patterns in higher dimensions (Brazhnik and Tyson, 1999). One of them describes a v-shaped waveform propagating through the two-dimensional medium, which can be interpreted as two straight wave fronts collapsing into each other at a given angle. Observed in the direction of a bisecting line, this combined wave front is indeed stationary at certain speeds. There also exist spatially oscillating front shapes, but these profiles are only possible for the extension of $u(x)$ out of the relevant range $u \in (0, 1)$ (Brazhnik and Tyson, 1999). We focus on cases where the wave propagation occurs as a radial expansion from a centered mass.

Nondimensionalization

We will use a nondimensionalized formulation of the Fisher-KPP equation to make our statements more general with regard to the parameter ranges of the diffusivity $D \in \mathbb{R}$ and the growth parameter $\rho \in \mathbb{R}$. We do this *only* for the derivation of the penalty term and return to dimensional form in the numerical tests when we investigate spatially varying diffusivity fields that are generated or given by datasets.

Since the long-term behavior of the one-dimensional Fisher equation equals a simple lateral movement, it is possible to state Equation (4.1) in equivalent form by introducing the

dimensionless variables

$$\tilde{t} = \rho t, \quad (4.2)$$

$$\tilde{x} = \sqrt{\frac{\rho}{D}} x - \tilde{v} \tilde{t}, \quad (4.3)$$

$$\tilde{v} = \frac{1}{\sqrt{\rho D}} v. \quad (4.4)$$

The transformation of the spatial coordinate can be understood as a scaled comoving reference frame, where $v \in \mathbb{R}$ is the limit propagation speed. Seen from this co-moving reference frame, the wavefront will not move laterally. Over a long period of time the wave front will converge to its limit shape, which we are seeking to reconstruct. After insertion of the new parameters, we find the nondimensionalized formulation

Definition 4.1.2 (1D Comoving Fisher-Kolmogorov-Petrovsky-Piscounov equation) Let $\tilde{x} \in \mathbb{R}$ be a nondimensional spatial coordinate, $\tilde{t} \in \tilde{T} = [\tilde{t}_0, \tilde{t}_e]$ temporal coordinates, $u(\tilde{x}, \tilde{t}) : \mathbb{R} \times \tilde{T} \rightarrow \mathbb{R}$ a tumor density and $\tilde{v} \in \mathbb{R}$ the limit propagation speed. We seek $u(\tilde{x}, \tilde{t})$ so that

$$\frac{\partial u(\tilde{x}, \tilde{t})}{\partial \tilde{t}} = \Delta u(\tilde{x}, \tilde{t}) + u(\tilde{x}, \tilde{t})(1 - u(\tilde{x}, \tilde{t})) + \underbrace{\tilde{v} \nabla u(\tilde{x}, \tilde{t})}_{\text{stationalization}} \quad (4.5)$$

The advective term $\tilde{v} \nabla u(\tilde{x}, \tilde{t})$ stems from the coordinate transformation into the comoving frame. We will use the comoving Fisher-KPP equation to derive a stationary problem formulation in Section 4.2.

4.1.2 Myopic forward model

The next step up in complexity from the Fisher-KPP model is the following anisotropic tumor model which includes the effects of inhomogeneous anisotropic diffusion and a (myopic) drift term that is a macroscopic effect of the biased random walk of the individual cells. For details on this we refer to (Hillen and Painter, 2013). The model is again a specialization of the FAAD Equation (2.1a) with the advection field $b(x) = \nabla \cdot \mathbf{D}(x)$ given by the tensor divergence (see Painter and Hillen (2018); Hillen and Painter (2013)).

Definition 4.1.3 (Myopic forward model)

Let $\Omega_b \subset \mathbb{R}^d$ be a bounded domain (brain). For $x \in \Omega_b$ and $t \in T = [t_0, t_e]$ as spatial and temporal coordinates we again describe the diffusive material properties by $\mathbf{D}(x) \in \mathbb{R}^{d \times d}$. We seek the tumor density profile $u(x, t) : \mathbb{R} \times T \rightarrow \mathbb{R}$ for which

$$\begin{aligned} \frac{\partial u(x, t)}{\partial t} &= \nabla \cdot (\mathbf{D}(x) \nabla u(x, t) + (\nabla \cdot \mathbf{D}(x)) u(x, t)) \\ &\quad + \rho u(x, t)(1 - u(x, t)) \end{aligned} \quad \forall (x, t) \in \Omega_b \times T, \quad (4.6a)$$

$$0 = (\mathbf{D}(x) \nabla u(x, t) + (\nabla \cdot \mathbf{D}(x)) u(x, t)) \cdot n, \quad \forall (x, t) \in \partial \Omega_b \times T, \quad (4.6b)$$

$$u(x, t_0) = g(x) \quad \forall x \in \Omega_b. \quad (4.6c)$$

$$(4.6d)$$

The myopic diffusion has been identified as superior in the description of cell dynamics compared to the common Fickian diffusion term $\nabla \cdot (\mathbf{D}(x) \nabla u(x, t))$. The introduced drift term allows for structure formation like local maxima at places where cells aggregate (Painter and Hillen, 2018). We will use this tumor model to investigate the applicability of the stationalization in the presence of anisotropic diffusion and weak advective effects.

4.1.3 Haptotactic tumor model

As a representative for more complex forward tumor models we use the model developed in Engwer et al. (2015, 2016), including a logistic proliferation term. It is one example of the multiscale modeling approach. Both the anisotropic diffusion terms as well as the haptotactic effects can be traced back to microscopic assumptions made for the individual tumor cells.

Definition 4.1.4 (Haptotactic forward model)

Let $\Omega_b \subset \mathbb{R}^d$ be a bounded domain (brain), $x \in \Omega_b$ be spatial coordinate, $t \in T = [t_0, t_e]$ a temporal coordinate and $u(x, t) : \Omega_b \times T \rightarrow \mathbb{R}$ a tumor density. Further, let $\mathbf{D}_t(x) \in \mathbb{R}^{d \times d}$ be the tumor diffusion tensor reconstructed from the water diffusion tensor $\mathbf{D}_w(x) \in \mathbb{R}^{d \times d}$, $b(x) \in \mathbb{R}^d$ the advective field defined shortly and $g(x) \in \mathbb{R}$ the initial tumor density. The

model by Engwer et al. (2015, 2016) is then given by

$$\begin{aligned} \frac{\partial u(x, t)}{\partial t} &= \nabla \cdot (\mathbf{D}_t(x) \nabla u(x, t)) + \nabla \cdot (b(x)u(x, t)) \\ &\quad + \rho u(x, t)(1 - u(x, t)) \end{aligned} \quad \forall (x, t) \in \Omega_b \times T, \quad (4.7a)$$

$$0 = (\mathbf{D}_t(x) \nabla u(x, t) + (\nabla \cdot \mathbf{D}_t(x))u(x, t)) \cdot n, \quad \forall (x, t) \in \partial\Omega_b \times T, \quad (4.7b)$$

$$u(x, t_0) = g(x) \quad \forall x \in \Omega_b. \quad (4.7c)$$

Where the contributing terms are

$$\mathbf{D}_t(x) = \frac{s^2}{\lambda_0(d+2)} \left(\mathbf{1} + 2 \frac{\mathbf{D}_w(x)}{\text{tr } \mathbf{D}_w(x)} \right), \quad (4.8a)$$

$$b(x) = v(x) - g(A(x))\mathbf{D}_t(x)\nabla A(x), \quad (4.8b)$$

$$v(x) = \frac{2s^2}{\lambda_0(n+2)} \left(\frac{\nabla \cdot \mathbf{D}_w(x)}{\text{tr } \mathbf{D}_w(x)} - \frac{\mathbf{D}_w(x) \cdot \nabla \text{tr } \mathbf{D}_w(x)}{(\text{tr } \mathbf{D}_w(x))^2} \right), \quad (4.8c)$$

$$g(A(x)) = \frac{\lambda_1 f'(A(x))}{(k^+ A(x) + k^- + \lambda_0)}, \quad (4.8d)$$

$$f'(A) = \frac{k^+ k^- R_0}{k^+ A(x)}, \quad (4.8e)$$

$$A(x) = \text{FA}(\mathbf{D}_w(x)) \quad (4.8f)$$

The above model contains parameters $s, \lambda_0, \lambda_1, k^+, k^-, R_0 \in \mathbb{R}$ from the microscopic scale, that are carried through the upscaling into the macroscopic model. For some of these parameters it is possible to define reasonable bounds from in-vitro experiments. The water diffusion tensors $\mathbf{D}_w(x)$ are given by the DTI datasets. Engwer et al. (2015) modeled the receptor binding availability to be proportional to the fractional anisotropy (FA) of the tissue (see Eq. (2.27)). The resulting haptotactic advective field is proportional to $\nabla \text{FA}(x)$, which has the effect that tumor density is transported towards regions of high anisotropy which in our case are the white matter tracts of the brain. This haptotactic advection is the main contributor to the observed heterogeneity in this model, with the myopic drift term diminishing in comparison.

4.2 Stationalization of Fisher-KPP equation in 1D

Earlier we introduced a *comoving* formulation of the Fisher Equation (4.5). For large times \tilde{t} the rate of change $\frac{\partial u(\tilde{x}, \tilde{t})}{\partial \tilde{t}}$ within Equation (4.5) will tend to zero, and the solution will be effectively stationary. The limit speed of the traveling wave solutions has been derived to be $v = 2\sqrt{\rho D}$, and in nondimensional coordinates $\tilde{v} = 2$ (Kolmogoroff et al., 1988). Within this formulation appears an advective term $\tilde{v}\nabla u(\tilde{x}, \tilde{t})$ which results from the coordinate transformation into the comoving frame. It can be understood as counteracting the lateral movement of the propagating front (Ablowitz and Zeppetella, 1979; Kolmogoroff et al., 1988). We will refer to this advective term and its approximations as the *stationalization term*.

Remark 4.2.1 *In the original publication by Kolmogoroff et al. (1988) it is stated that there are solutions for speeds higher than \tilde{v} . This fact is due to the reaction term acting independently of the local environment. For the limit of diminishing diffusion, the reaction term alone can induce very high traveling wave speeds for initial conditions which are close to horizontal. For initial conditions with compact support, which is the relevant case here, the speed tends to $2\sqrt{D\rho}$ as time goes to infinity (Kolmogoroff et al., 1988). In the context of glioma invasion only the very rapid spatial decay of tumor density is relevant and we expect no extended density distributions as initial conditions.*

We will now propose an alternative form of that term, which is exact only in the infinite time limit. We do this via an analytical limit solution $u_s(\tilde{x}) : \mathbb{R} \rightarrow \mathbb{R}$ of the comoving Fisher-KPP equation (4.5). With this analytical solution $u_s(\tilde{x})$ we calculate an analytical expression for $\nabla u_s(\tilde{x})$. We then express this gradient in terms of the *amplitude* of $u_s(\tilde{x})$. This is possible because the solution is invertible in the relevant range $u_s(\tilde{x}) \in (0, 1)$. The resulting expression $p(\cdot) = \tilde{v}(\nabla u_s(\tilde{x}))(\cdot) : \mathbb{R} \rightarrow \mathbb{R}$ is a mapping from the amplitude of the limit solution $u_s(\tilde{x})$ to its gradient. With this, we may express the problem of finding the stationary limit solution u_s in the following way,

$$0 = \Delta u_s + u_s(1 - u_s) - \underbrace{p(u_s)}_{\text{stationalization}}. \quad (4.9)$$

We will now derive the approximation $p(u_s(\tilde{x})) : \mathbb{R} \rightarrow \mathbb{R}$ to the advection term within Equation (4.5) via the analytical solution stated by Ablowitz and Zeppetella (1979). For

long time scales and no boundary conditions, a comoving wave form can be given in explicit form for the special wave speed of $\tilde{v} = \frac{5}{\sqrt{6}}$,

$$u_s(\tilde{x}) = \frac{1}{\left(1 + \exp\left(\frac{\tilde{x}}{\sqrt{6}}\right)\right)^2}. \quad (4.10)$$

We call the analytical limit profile (4.10) the *equilibrated* wave-form or limit solution (Ablowitz and Zeppetella, 1979). A stationalization term $p(u_s)$ can be directly derived from it. The gradient of the analytical solution (4.10) is

$$\nabla u_s(\tilde{x}) = \frac{-\sqrt{\frac{2}{3}} \exp\left(\frac{\tilde{x}}{\sqrt{6}}\right)}{\left(1 + \exp\left(\frac{\tilde{x}}{\sqrt{6}}\right)\right)^3}. \quad (4.11)$$

The inverse of the analytical solution in the range $u_s \in (0, 1)$ is given by

$$\tilde{x}(u_s) = \sqrt{6} \ln\left(\frac{1}{\sqrt{u_s}} - 1\right). \quad (4.12)$$

and represents the mapping from a given amplitude $u_s \in \mathbb{R}$ to the corresponding position $\tilde{x} \in \mathbb{R}$ within the limit solutions profile (4.10). Substituting the inverse (4.12) into the gradient expression (4.11) yields an analytical term for $(\nabla u_s)(u_s)$

$$\nabla u_s(u_s) = \sqrt{\frac{2}{3}}(1 - \sqrt{u_s})u_s, \quad (4.13)$$

This term is only dependent on the local amplitude of $u_s(x)$ providing the gradient of the wave fronts profile upon evaluation. We can state a closed form for the stationalization term

$$p(u_s) = |\tilde{v}| \sqrt{\frac{2}{3}}(1 - \sqrt{u_s})u_s,$$

where we used the absolute value of \tilde{v} to not be dependent on the direction of the traveling front. We have essentially calculated a nonlinear penalty term, which is only dependent on the local amplitude, and not the local gradient and has the same effect on the solution as the advective term in the comoving formulation in Equation (4.5). For this simple one-dimensional and homogeneous case the problem of finding the limit solution to the comoving Fisher-KPP equation (4.5) can be formulated either with $p(u_s)$ as a penalty term, or the advective term $-\tilde{v}\nabla u_s(x)$.

Remark 4.2.2 *The strict equivalence between $p(u_s)$ and the stationalizing term $-\tilde{v}\nabla u_s(x)$*

only holds for the limit case $t \rightarrow \infty$, initial conditions that lead to the solution given by Ablowitz and Zeppetella (1979) and $\tilde{v} = \frac{5}{\sqrt{6}}$, in which the analytical solution is known and in absence of boundary conditions, i.e., $\Omega \equiv \mathbb{R}$. In all other cases it should be considered an approximation.

Although this formulation is only strictly equivalent in case of a completely equilibrated wave form, we will use the derived penalty term $p(u_s(x))$ as an *approximation* allowing us to define stationary wave-pinning type models. In higher dimensions, the transformation into a comoving frame, and an unambiguous inversion pose nontrivial challenges.

The Fisher-KPP equation is one representative out of a family of KPP-type equations which combine a diffusive term with a nonlinear reaction term $f(u)$. The reaction term is often chosen in a manner so that it dynamically connects two fixed points of amplitude: $f(0) = 0, f(1) = 0$ and $f(u) > 0$ for $u \in (0, 1)$. Although an exact analytical description of the limit solutions proves difficult, the rough characteristic of propagating fronts found in nature (combustion, bacterial growth etc.) is often s-shaped (sigmoid). The gradient distribution of any sigmoid-like traveling wave front will have a simple shape, very similar to $p(u_s)$. For any sigmoidal wave-form $|\nabla u|$ will be zero for $u = 0$ and $u = 1$ and of higher amplitude for $0 < u < 1$. The underlying idea of the stationalization procedure is, that the gradient distribution $|\nabla u|(u)$, and therefore the penalty term necessary to calculate the stationary wave front, may be approximated to a good degree of accuracy even for those cases where an analytical solution is not at hand.

It was proven by (Huang, 2008), that all (planar or nonplanar) traveling wave front solutions to the Fisher equation are stable, given that the perturbations have compact supports. The shape of the wave front is therefore robust in the sense that a profile which is flatter than the limit solution would approach the analytically predicted one from below due to the nonlinear growth terms, and a profile, which is steeper than the limit shape, will flatten through diffusion. The stability result carries over to the stability of the predicted gradient distribution. The general shape of the gradient profile $(\nabla u_s)(u_s)$ is robust in the sense that the gradient distribution of a profile which is flatter than the limit solution would approach the analytically predicted one from below due to the exponential growth terms and a profile which is steeper than the limit shape will flatten through diffusion. It is this stability that may make the stationalization a viable approach for more elaborate tumor models.

4.3 Stationalized tumor models

We now define stationary problems with the help of the penalty term derived in the previous section. We define the problems within a finite domain and they are intended to *approximate* the tumor progression at finite times. The assumptions of an infinite domain and $t \rightarrow \infty$ which we used to derive the term are not given anymore (see Remark 4.2.2).

There is one more component to formulating the stationary formulations. The limit solution to the comoving formulation given in Equation (4.10) is not unique. With $u_s(\tilde{x})$ as an limit solution to (4.5) any laterally shifted profile $u_s(\tilde{x} - \delta)$, with a constant offset $\delta \in \mathbb{R}$ is also a solution to (4.5). That implies that in order to define the approximative problem formulations to estimate the tumor density additional side conditions are necessary.

We now define the stationary models which correspond to the forward models we introduced in Equations (4.1, 4.6, 4.7a). We define the stationary Fisher model in nondimensionalized form, and the other two models which incorporate inhomogeneous diffusion fields in dimensional form. Since the infinite time assumption is not valid anymore, the value $v \in \mathbb{R}$ should be considered a free penalty parameter in these models.

Definition 4.3.1 (1D Stationary Fisher model)

Let $\Omega_b \subset \mathbb{R}$ be the one-dimensional domain (brain), and $\tilde{x} \in \Omega_b$ a spatial coordinate. Within Ω_b we define a smaller enclosed domain $\Omega_i \subset \Omega_b$ representing the border of the visible tumor on the medical images. We then seek the tumor density profile $u_s(\tilde{x}) : \mathbb{R} \rightarrow \mathbb{R}$ for which

$$0 = \underbrace{\Delta u_s(\tilde{x}) + u_s(\tilde{x})(1 - u_s(\tilde{x}))}_{\text{tumor model prototype}} - \underbrace{|\tilde{v}| \sqrt{\frac{2}{3}}(1 - \sqrt{u_s(\tilde{x})})u_s(\tilde{x})}_{\text{stationalization}} \quad \forall \tilde{x} \in \Omega_b, \quad (4.14a)$$

$$\nabla u_s(\tilde{x}) \cdot n = 0 \quad \forall \tilde{x} \in \partial\Omega_b, \quad (4.14b)$$

$$u_s(\tilde{x}) = 0.16 \quad \forall \tilde{x} \in \partial\Omega_i. \quad (4.14c)$$

At the border of the visible tumor $\partial\Omega_i$ we imposed an *internal* Dirichlet boundary condition, assuming that the visibility threshold of the tumor is at 16% volumetric tumor density (Swanson et al., 2008). The additional boundary at $\partial\Omega_i$ is used to localize the

stationary solutions.

The two stationary formulations (4.15a, 4.7a) of the myopic- and the haptotactic forward models given in Equations (4.6a) and (4.7a) are modeled analogously to the above. They are modeled by adding the stationalizing penalty term $p(u_s)$, setting the temporal derivative to zero and imposing the internal Dirichlet constraints at the visibility threshold.

Definition 4.3.2 (Myopic stationary model)

Let $\Omega_b \subset \mathbb{R}^d$ be a bounded domain (brain) with $\Omega_i \subset \Omega_b$ a smaller enclosed domain (tumor), $x \in \Omega_b$ a spatial coordinate, $\mathbf{D}(x) : \mathbb{R}^d \rightarrow \mathbb{R}^{d \times d}$ a diffusivity field, $\rho \in \mathbb{R}$ a growth rate and $v \in \mathbb{R}$ the penalty parameter. We then seek the tumor density $u_s(x) : \mathbb{R}^d \rightarrow \mathbb{R}$ for which

$$0 = \nabla \cdot ((\mathbf{D}(x)\nabla u_s(x)) + (\nabla \cdot \mathbf{D}(x))u_s(x)) \\ + \rho u_s(x)(1 - u_s(x)) - |v| \rho \sqrt{\frac{2}{3}} \left(1 - \sqrt{u_s(x)}\right) u_s(x) \quad \forall x \in \Omega_b, \quad (4.15a)$$

$$0 = (\mathbf{D}(x)\nabla u_s(x) + (\nabla \cdot \mathbf{D}(x))) \cdot n, \quad \forall x \in \partial\Omega_b, \quad (4.15b)$$

$$u_s(x) = 0.16 \quad \forall x \in \partial\Omega_i. \quad (4.15c)$$

Here, $\partial\Omega_i$ is the visibility border of the tumor on the medical images, and Ω_i the tumor volume. The stationary myopic model includes the effects of anisotropic diffusion and myopic drift just as in the forward model. They were also investigated in Engwer and Wenske (2020).

Definition 4.3.3 (Haptotactic stationary model)

Let $\Omega_b \subset \mathbb{R}^d$ be a bounded domain (brain) with $\Omega_i \subset \Omega_b$ a smaller enclosed domain (tumor), $x \in \Omega_b$ a spatial coordinate, $\mathbf{D}_t(x) : \mathbb{R}^d \rightarrow \mathbb{R}^{d \times d}$ the tumor diffusivity field reconstructed from the medical data (see Eq. (4.8a)), $\rho \in \mathbb{R}$ a growth rate and $v \in \mathbb{R}$ the penalty parameter. We then seek the tumor density $u_s(x) : \mathbb{R}^d \rightarrow \mathbb{R}$ for which

$$0 = \nabla \cdot (\mathbf{D}_t(x)\nabla u_s(x) + b(x)u_s(x)) \\ + \rho u_s(x)(1 - u_s(x)) - |v| \rho \sqrt{\frac{2}{3}} \left(1 - \sqrt{u_s(x)}\right) u_s(x) \quad \forall x \in \Omega_b, \quad (4.16a)$$

$$0 = (\mathbf{D}_t(x)\nabla u_s(x) + b(x)u_s(x)) \cdot n, \quad \forall x \in \partial\Omega_b, \quad (4.16b)$$

$$u_s(x) = 0.16 \quad \forall x \in \partial\Omega_i. \quad (4.16c)$$

4.3.1 Notes on uniqueness

The limit solutions to the forward Fisher-KPP equation (4.1) allow for traveling wave solutions moving in both the positive and negative direction. In the stationalized (comoving) formulation we find a similar situation.

Since we use an internally constrained surface given by the visible tumor surface, we may expect two possible solutions to the comoving formulation (4.5) or its approximation (4.14a). The first stationary solution corresponds to the a traveling wave which moves outwards from the tumor center, at that point in time where it satisfies the Dirichlet constraint (see Eqs. (4.16c, 4.15c, 4.14c)). This solution is the relevant one for the given application. We call this the outwards moving solution branch (OMS). The second possible solution corresponds to a traveling wave moving into the constrained region, i.e., the inwards moving solution (IMS). This solution branch is *irrelevant* to tumor growth modeling. The stationary solutions of the two branches are sketched in the left side of Figure 18. When

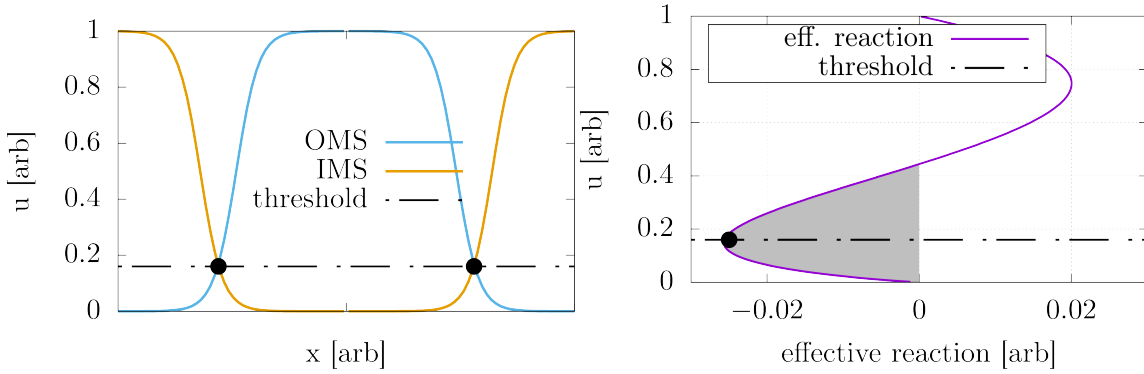


Figure 18: Left: schematic of outward and inward moving solutions (OMS, IMS), both fulfilling the internal Dirichlet constraints (black dots) at the visibility threshold at $u = 0.16$. Right: plot of combined reactive terms, i.e.: $u_s(1 - u_s) - \sqrt{\frac{2}{3}}(1 - \sqrt{u_s}u_s)$. The penalizing regime is indicated in gray. The visibility threshold is within the penalizing regime.

considering the effective reaction term consisting of the logistic growth combined with the penalty term (Figure 18), we find that it has a penalizing regime for $0 < u < \frac{4}{9}$ and a growth regime for $\frac{4}{9} < u < 1$.

Any diffusive process transports mass from regions of high concentration to those with lower concentration. The combined reaction term sketched in the r.h.s. of Figure 18 counteracts this process. The visibility threshold, and therefore the internal dirichlet constraints, lie within the penalizing regime. In order to select the OMS solution branch, which is the rel-

evant one for the medical case, we supply the Newton iteration of the variational problem (2.4) with initial guesses $u_s(x) \ll 1, \forall x \notin \Omega_i$ which are well within the purely penalizing regime, so that the newton iteration converges to the outward moving solution reliably.

4.4 Numerical methods

In order to test the validity of the stationalization approach, a series of numerical experiments was conducted. We will now describe their setup and the error quantization before presenting the results. In these tests the solutions to the forward and the stationary problems are compared. The numerical setup of these comparisons follow three steps:

1. The forward simulations are started from a small Gaussian initial condition up to a given time and represent the tumor growth predicted by the forward model.
2. Then, the forward solution is used to mimic the thresholded information of the medical images by defining a level set on the forward solution as the internal Dirichlet constraint for the stationalized problem formulations.
3. Then, the corresponding stationary problem is solved and compared against the predictions of the forward model.

In Section 4.5 we will investigate the stationalization via direct comparison. Given a (forward) reference solution $u(x, t)$ and a stationary approximation $u_s(x)$ within $\Omega_b \subset \mathbb{R}^d$ (brain) and a threshold (level set) value $\theta \in \mathbb{R}$ we define two domains A and B as

$$A = \{x \in \Omega_b | u(x, t) \geq \theta\}, \quad B = \{x \in \Omega_b | u_s(x) \geq \theta\}.$$

The medically relevant information is the spatial discrepancy between two level set surfaces $(\partial A, \partial B)$ of these density profiles. One possible measure for this error is the symmetric difference $|A \oplus B|$, as depicted in Figure 19. It describes those volumes, which are either included in A but not in B , or vice versa. That way, both over- and underestimations of the approximation $u_s(x)$ are represented. The symmetric difference is, however, not comparable between 1D, 2D and 3D simulations.

The most expressive information in the medical context is the distance *between* the two

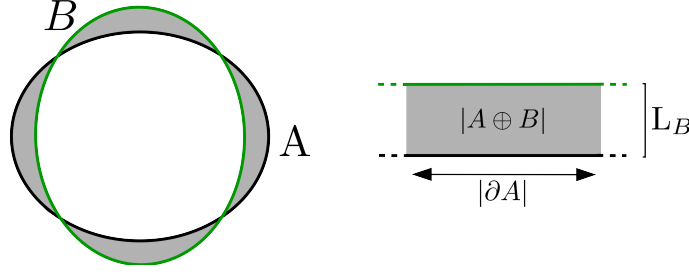


Figure 19: Left: Symmetric difference region between the two level sets $|A \oplus B|$: gray regions. Right: localized sketch of the symmetric difference region, the surface of the level set volume $|\partial A|$ and the approximate distance between the two level sets L_B .

level sets. We therefore introduce the global characteristic level set distance.

Definition 4.4.1 (Global characteristic level set distance)

For a given level set value $\theta \in \mathbb{R}$, we define the characteristic level set distance between ∂A and ∂B as

$$L_B := \frac{|A \oplus B|}{|\partial A|}.$$

It quantifies the average distance between the two level sets. Assuming a spherical reference geometry for A we can approximate this expression in the following way. Given the radius r_A of a reference sphere, L_B simplifies to

$$L_B^{1d} = \frac{|A \oplus B|}{2}, \quad L_B^{2d} = \frac{|A \oplus B|}{2\pi r_A} \quad \text{and} \quad L_B^{3d} = \frac{|A \oplus B|}{4\pi r_A^2}. \quad (4.17)$$

We will state this error for the numerical 2D and 3D examples where forward simulations are compared to stationary simulations.

The presented tests increase in complexity from the 1D homogeneous Fisher-KPP Equation and its stationalization in Section 4.5.1 to the 2D inhomogeneous test case with the myopic diffusion model in Section 4.5.3. Subsequently, an investigation of the gradient profiles in both 1D and 2D is presented in Section 4.5.4. There, we directly compare the penalty term with the observed gradient statistics. Finally, we present comparisons between forward simulations and stationary approximations on a healthy patient dataset in Section 4.5.5. We present the application to real patient data sets separately in Section 6 where the internal constraints are given directly by the medical segmentation.

We want to stress that the stationalization approach is independent of the choice of numerical discretization method. No significant differences of the results were observed when

other numerical schemes were used (MPFA-O, CFEM, HFVM). For the 1D examples we used a conforming finite element discretization with piecewise linear base functions. For the 2D and 3D examples, we used the Hölder finite volume method as introduced in Section 3, with the log-Euclidian matrix interpolation ($\alpha \rightarrow 0$).

The temporal discretization was an implicit Euler method for all tests conducted. The grid resolutions and initial conditions are stated next to the examples.

4.5 Numerical results

The following numerical results represent an investigation of the applicability of the stationalization. For this purpose we set up 1D comparisons for both homogeneous and inhomogeneous media in Sections 4.5.1 and 4.5.2. We then present 2D results of the myopic forward and stationary model to investigate whether the stationary approximations retain sufficiently precise for inhomogeneous media and in higher dimensions (see Section 4.5.3). This testcase is also easily reproducible for other researchers. We investigate the validity of the stationalization term approximation via gradient statistics in Section 4.5.4. Finally we show a direct comparison of 3D results on a data set of a healthy subject for the haptotactic tumor model (see Eq. (4.7a)). Similar tests were conducted with a conforming finite element discretization for Engwer and Wenske (2020).

4.5.1 1D homogeneous Fisher-KPP equation

We now present 1D simulations for the homogeneous Fisher-KPP equation and its stationalized counterpart. The numerical test is set up as follows. We begin a forward simulation of the Equation (4.1) from a Gaussian initial condition imitating carcinogenesis. We chose $D = 1$ and $\rho = 1$ so that we may directly compare the forward results to those of the nondimensionalized stationary formulation. We conduct the forward simulation imitating the tumor growth phase. In this growth phase the tumor grows outward forming a propagating front. We then use the result of the forward simulation after a given time $t_e = 20$ to define the pinning side condition stated in Equation (4.14c) for the stationalized Fisher-KPP formulation (4.14a). The side condition is found by assuming a visibility threshold of $u(x, t_e) \geq 0.16$. With this side condition, the stationalized problem with $\tilde{v} = v = \frac{5}{\sqrt{6}}$ is solved to approximate the underlying tumor distribution. Figure 20 illustrates the numer-

ical setup and the result.

In the top plot of Figure 20 we see the Gaussian initial condition at $x = 50$. From this

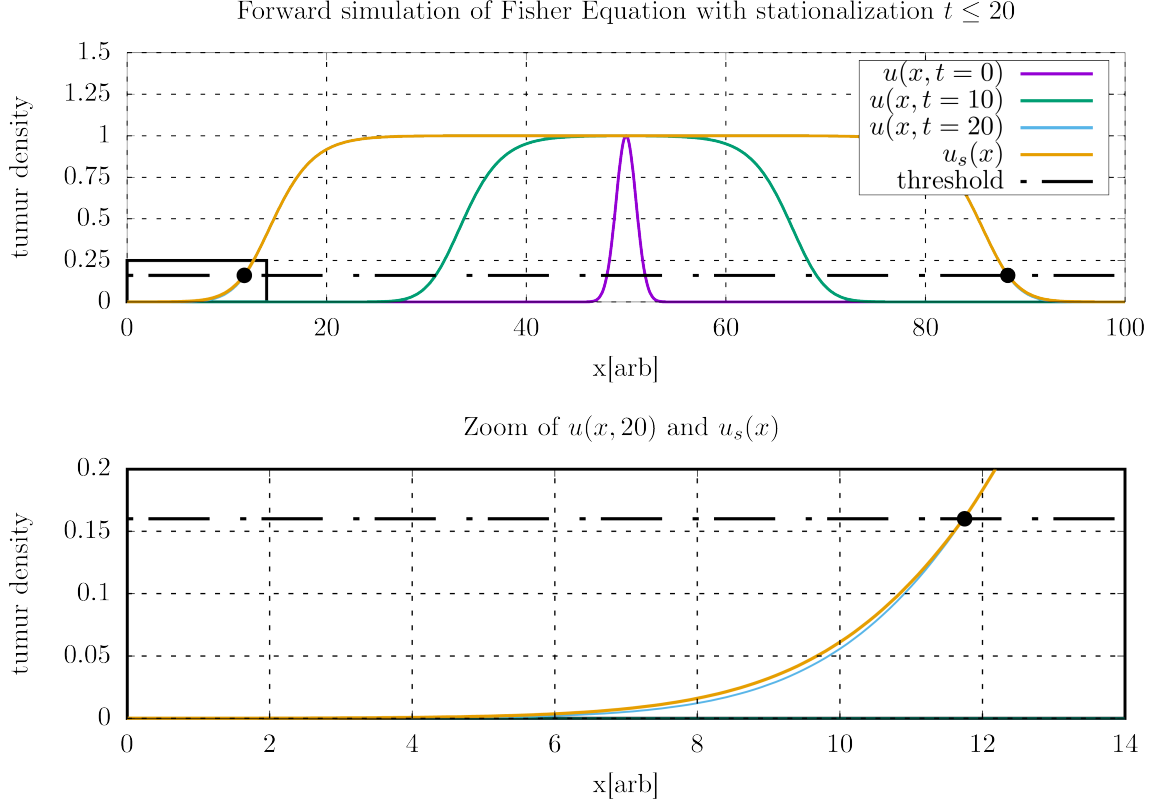


Figure 20: Top: forward simulations of the homogeneous Fisher-KPP equation ($D = 1, \rho = 1$), and the stationalized formulation given in Equation (4.14a) with $\tilde{v} = v = \frac{5}{\sqrt{6}}$. At $t_e = 20$ the internal pinning side condition for the stationalized formulation is set at the locations where $u(x, t_e) = 0.16$ (black dots). Bottom: zoom of the forward simulations profile (lower left rectangle in upper plot), which would not be visible in a thresholded imaging modality, and the stationalized approximation to it. The two profiles show near perfect agreement.

central peak the tumor grows outward over time. One important observation is, that the rough shape of the tumor invasion front is formed *rapidly*. This implies that the difference between the finite time wave front and the limit profile is small even early in the tumor progression.

The bottom part of Figure 20 shows the left part of the forward solution which is outside of the presumed imaging threshold ($u(x, t) < 0.16$) in detail. The assumed visibility threshold is marked by a dashed horizontal line. The profile below this threshold would not be visible on the medical images but is that information which is most important in

the treatment planning. The solution to the stationary problem formulation and that of the forward solution show near perfect agreement. The remaining difference between the two could be further diminished by altering the penalty parameter v .

The one-dimensional Fisher equation is not suited to predict tumors in real patients. We continue by presenting how the stationalization works in the presence of inhomogeneous diffusion.

4.5.2 1D myopic testcase

We now present results for a testcase similar to the previous one, with the important distinction that we include myopic drift and diffusion effects. The forward model is given by Equation (4.6a) and the stationary model by Equation (4.15a). We assume a pseudorandom diffusivity field $D_\beta(x) \in \mathbb{R}$ as defined in Equation (2.25). We again start the forward simulation from a centered Gaussian initial condition.

The top of Figure 21 indicates the three states of the forward simulation. The grey background profile shows the local diffusivity perturbations. The bottom of Figure 21 shows the final state of the forward simulation, as well as the stationary approximation to it. Both the forward and the stationary result show local perturbations away from a smooth sigmoidal front shape. The effect of statistical scattering of the diffusive properties on the macroscopic front speed is non-trivial. In cases that include anisotropic diffusion, we no longer know the limit speed exactly, and the penalty parameter v has to be chosen manually. The results give an indication of the effect that diffusivity perturbations of realistic data sets have on the stationary solution. The diffusivity field in this example is only locally perturbed. In the next section we will present results with more long-range changes in diffusivity.

4.5.3 2D myopic diffusion model

To investigate if the stationalization may remain applicable for more complex situations, we set up a two-dimensional testcase. We numerically solve the 2D myopic tumor model given in Equation (4.6). The setup follows the same steps as in Section 4.5.1, but now the diffusivity field $\mathbf{D}(x)$ is inhomogeneous, leading to contributions of the myopic advection

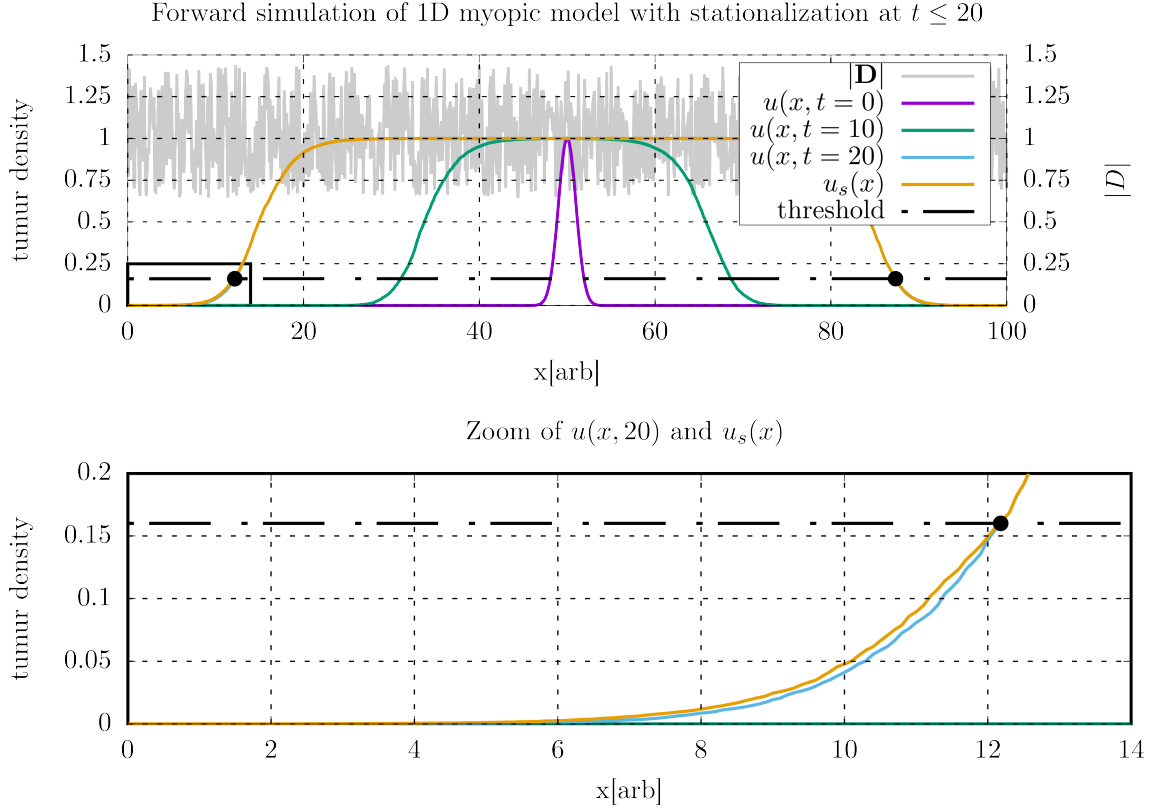


Figure 21: Top: Forward simulations of the anisotropic myopic tumor model ($\rho = 1$, D_β as defined in Equation (2.25), $\beta = 0.2$) at different time points and the solution to the stationalized formulation given in Equation (4.15a) with $v = \frac{5}{\sqrt{6}}$. At $t = 20$ the internal pinning side condition for the stationalized formulation is set at the locations where $u(x) = 0.16$ (black dots). Bottom: Zoom of the forward simulations profile, which would not be visible in a thresholded imaging modality, and the stationalized approximation to it. The two profiles show perturbations from the varying local diffusivity field.

terms. We set the diffusivity distribution for the simulation box to

$$\mathbf{D}(x) = \mathbf{1}_2 \begin{pmatrix} 1.0 + \sin\left(\frac{3\pi}{L_x}x_1\right) & 0.9 \end{pmatrix}, \quad (4.18)$$

with $L_x = 100$ and use the growth parameter $\rho = 1$. This diffusivity field effectively separates the domain into a region with low diffusivity (center) and two regions with high diffusivity (left and right). This can be thought of as artificial adjacent grey and white matter regions. The simulation domain is given by $x \in [0, 100]^2$ and discretized into 200×200 control volumes. We again start the forward simulation from a small Gaussian initial condition at the center. After the growth phase at $t = 20$, we use the forward solution to set

the internal boundary condition for the stationalized formulation of the myopic model (see Eq. (4.15a)). The solution of the forward model and the stationalized model ($v = \frac{5}{\sqrt{6}}$) is presented in Figure 22. Figure 22 compares the forward solution and its level sets to the

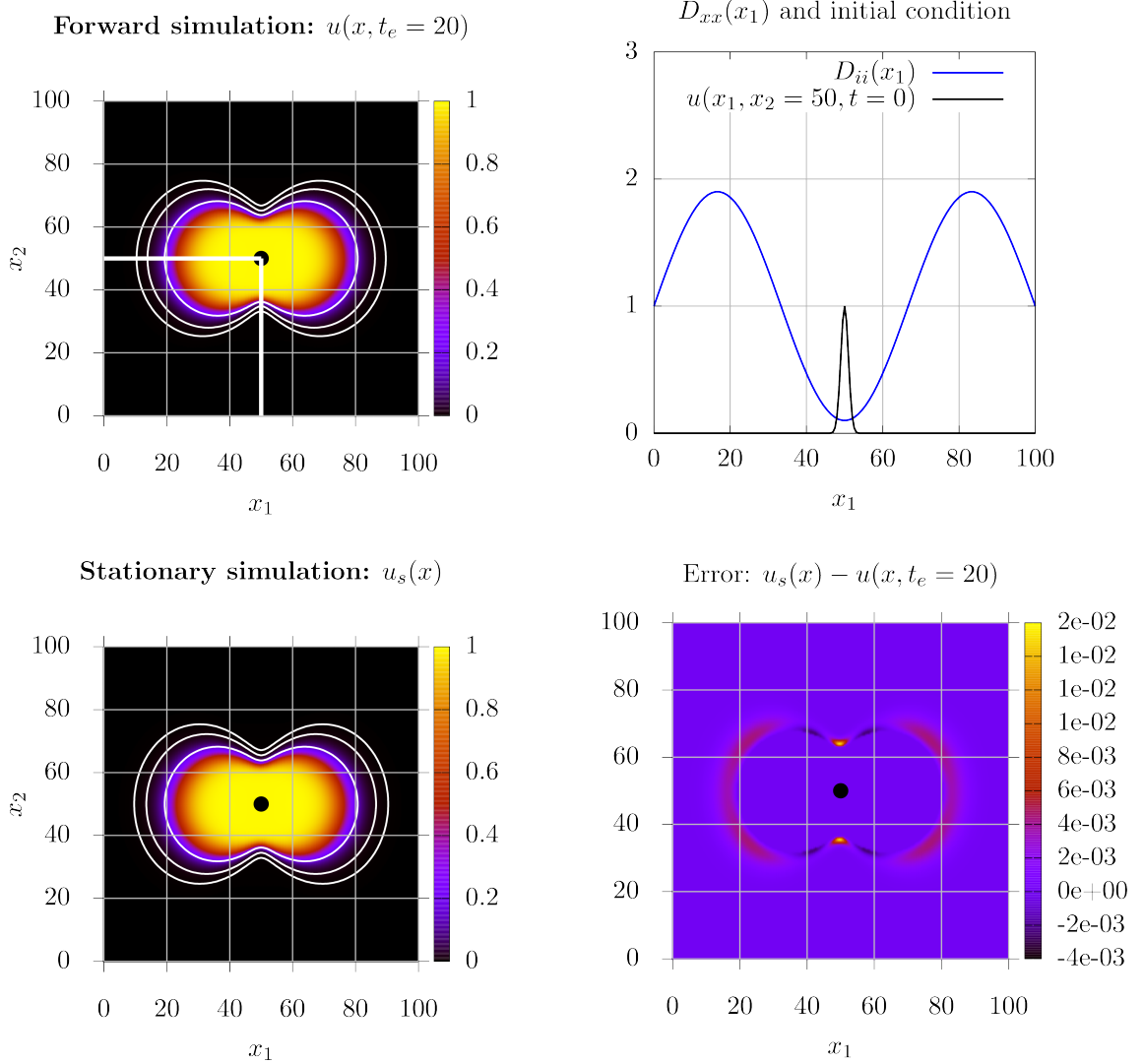


Figure 22: Level sets on both the forward and the stationary solution are set at $u(x, t_e), u_s(x) = 0.16, 10^{-2}, 10^{-3}$

. Top left: forward simulation of the myopic tumor model 4.6 from small Gaussian initial condition at $t = 20$. Top right: line plot through the initial condition and the diagonal elements \mathbf{D}_{xx} of the diffusivity field $\mathbf{D}(x)$, see Equation (4.18). Bottom left: solution to the stationary problem formulation with identical level sets. Bottom right: absolute error field of the stationary solution.

stationalized approximation visually. The general shape of the invasion profile predicted

by the forward model is correctly reproduced. In vertical direction through the location of the initial condition the predicted invasion extent is small, correspondingly in horizontal direction the invasive profile is larger. The stationalization therefore correctly produces an extended profile in those regions where the diffusivity is increased and a diminished intrusion where the diffusivity is low. This is a key property. If the stationalization should be applied to models with additional advective or diffusive effects, then the predicted deviation of the level sets will show correct extension or retraction, at least qualitatively.

4.5.4 Investigation of gradient statistics

In the derivation of the stationary models, we assumed that the gradient distribution of the front profiles may be approximated to a good degree of accuracy. To verify this, we investigate the quality of the approximation by directly comparing the analytically predicted gradient distribution of the Fisher-KPP Equation (see Eq. (4.13)) with the observed gradient amplitudes of our numerical forward simulations.

Figure 23 shows the observed gradient amplitudes of the forward simulations $|\nabla u(u)|$ (grey) next to the one assumed in the penalty term $|\nabla u_s(u_s)|$ (yellow). The results show that for the 1D homogeneous Fisher equation, the gradient statistic indeed approaches the predicted limit over time (top). In the middle of Figure 23 it is also visible that the influence of short-range inhomogeneity is limited to small deviations away from the correctly predicted baseline.

We also present the measurement of the absolute gradient along a horizontal and vertical line through the 2D solution presented earlier in Figure 22. In that numerical setup, the deviations in diffusivity were more long-range than in the 1D examples. The interpretation of these gradient statistic for the inhomogeneous 2D example is a bit more involved. The horizontal measurement is from the left border of the domain into the center of the initial condition. The vertical measurement was taken from the bottom of the domain to the center. The horizontal and vertical line are marked in white in Figure 22.

For the vertical measurement we see in Figure 23 that the derived gradient of the limit solution is considerably smaller in amplitude than the observed gradient, resulting in a comparatively strong overestimation of simulated tumor density along this path. This error can be directly observed at the two locations (50, 35) and (50, 65) in the error plot within Figure 22. For the horizontal measurement we find that the derived gradient serves a better approximation, resulting in only miniscule errors in this direction.

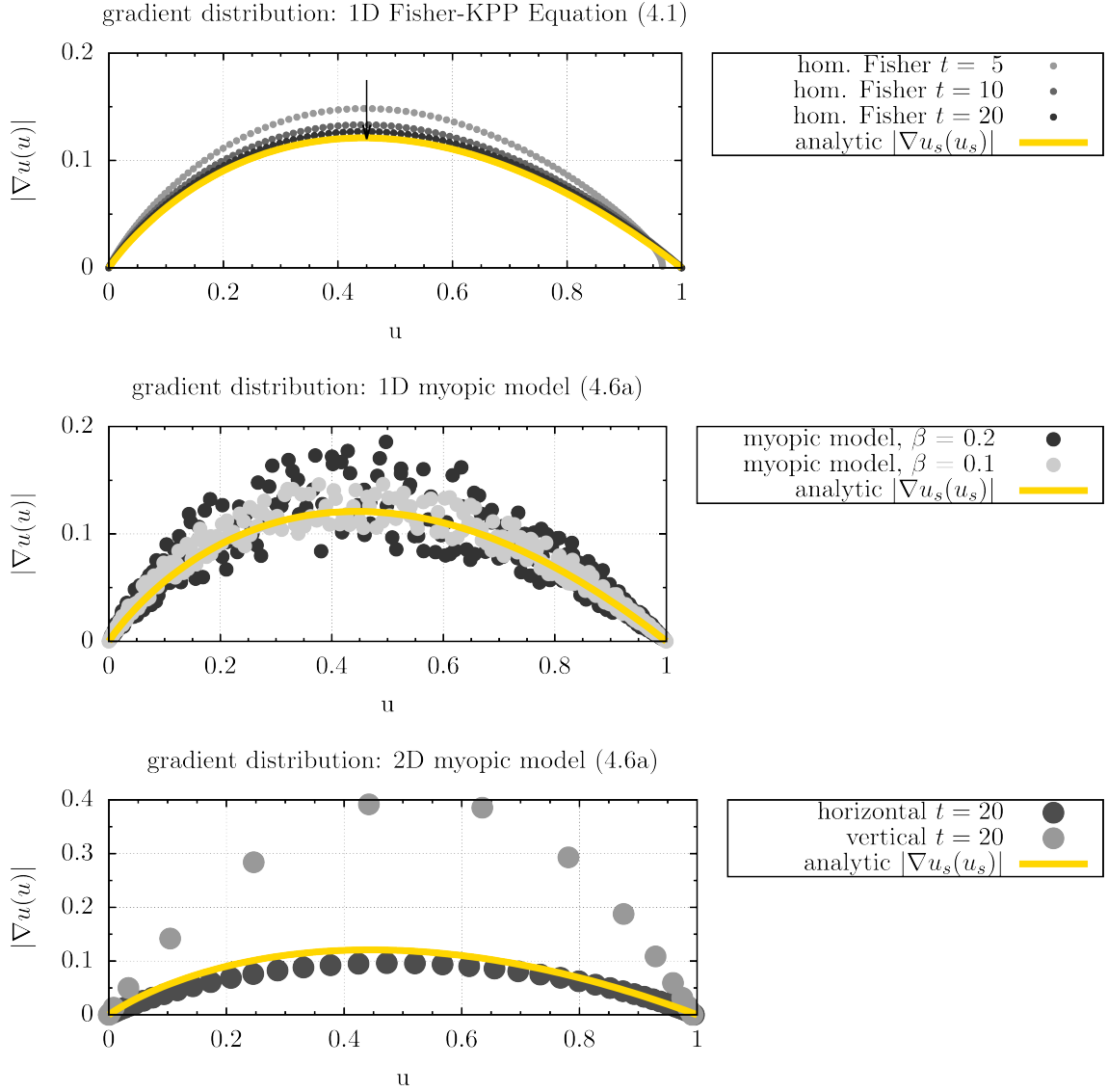


Figure 23: Top: Gradient distribution at three states of the 1D homogeneous numerical example (Fisher equation) from Section 4.5.1. The gradient distribution approaches the predicted curve given in Equation (4.13) as time increases (arrow). Middle: Final distribution ($t = 20$) for 1D simulations of the myopic diffusion model as given in Section 4.5.2 with different amounts of diffusive scattering ($\beta = 0.2, 0.1$, see Equation (2.25)). Bottom: gradient statistics along a vertical and a horizontal line through the 2D density profile of the 2D myopic test case from Section 4.5.3. The two lines along which the gradients were measured are indicated in the top left of Figure 22.

In this setting we have *not* optimized the penalty parameter. A simple adjustment of the parameter $v \in \mathbb{R}$ could improve the approximation further. The presentation of the

gradient statistic for the 2D testcase illustrates that the choice of a globally constant penalty parameter v becomes nontrivial as soon as spatially varying effective front speeds are expected.

4.5.5 3D comparison of forward and stationary solutions

We now present direct comparisons of forward simulations of the haptotactic model from Equation (4.7a) with its stationalized counterpart (4.16a). The model includes anisotropic inhomogeneous diffusion and haptotactic advective effects. The simulations are conducted on a data set of a healthy subject (*camino*) which is publicly available (Cook et al., 2006). In this setup, we artificially set the locations of carcinogenesis and simulate the invasions up

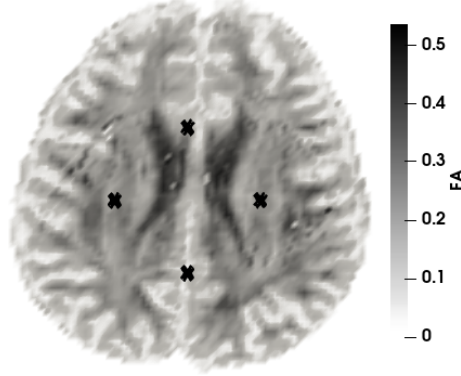


Figure 24: Axial slice of the dataset of a healthy subject (*camino*), with fractional anisotropy (FA) shading (Cook et al., 2006). Positions of small Gaussian peaks (initial conditions) for the comparison of forward and stationary simulations are marked with black crosses: Frontal: (0.11 m, 0.08 m, 0.05 m), Posterior: (0.11 m, 0.14 m, 0.05 m), Left: (0.08 m, 0.11 m, 0.05 m), Right: (0.14 m, 0.11 m, 0.05 m)

until a certain time $t_e = 30d$. At this end time we obtain the internal constraints necessary for the calculation of the stationary simulations by taking level sets of $u(x, t_e) = 0.16$ on the forward solutions. We then solve the stationary problem formulations and compare how well the stationary solutions correspond to the forward profiles. Figure 24 shows the chosen locations of carcinogenesis of the four separate simulations. We quantify the errors via the characteristic level set distance introduced in Equation (4.17). The errors can be interpreted as the average distance between the level sets on the forward simulations and the level sets on the stationary simulations. These results may illustrate that the stationalization provides good estimates on the state of the forward simulations even for more elaborate models.

It should be stressed that the tests may not give any insights on the validity of the tumor model itself. They merely quantify how well the stationalization performs against the forward model predictions.

The parameters that we use for the forward and stationary simulation are listed in Table

Parameter	Value
s	$1\text{e-}6 \left[\frac{m}{s}\right]$
ρ	$8.44\text{e-}7 \left[\frac{1}{s}\right]$
R_0	$1\text{e}3$
λ_0	$0.1 \left[\frac{1}{s}\right]$
λ_1	$1\text{e-}3 \left[\frac{1}{s}\right]$
k_+	$0.1 \left[\frac{1}{s}\right]$
k_-	$0.1 \left[\frac{1}{s}\right]$
v	$\frac{5}{\sqrt{6}}$

Table 9: Parameters used for the 3D stationary simulations of model (4.16a) resulting in a low effective Péclet number $Pe \approx 0.1$.

9. The average Péclet number throughout the brain for the chosen parameterization is approximately $Pe \approx 0.1$, indicating that the problem is diffusion dominated (see Eq. (2.2)).

Figure 25 presents level sets on the final states of the four forward solutions and their corresponding stationary solutions. The forward level sets $u(x, t_e) = 0.16, 10^{-2}, 10^{-3}$ are marked in green and the level sets on the stationary solutions are marked in red. The background is given by the fractional anisotropy (FA) defined in Equation (2.27). The indicated grid has a spacing of 1 cm. For this parameterization which results in low effective Péclet number, we find near-perfect agreement between the level sets on the forward solution and the level sets on the stationary solutions. It is also visible that the extensions of the predicted tumor profile into regions of high anisotropy (dark) are shared between both formulations. The chosen end time of $t_e = 30d$ seems to be sufficiently large for the infiltration fronts to build up.

The average level set distances of these four simulations are indicated in Figure 26. It shows the characteristic level set distance L_B for many possible level set values. In any practical application, only those level set values are relevant that reproduce the treatment radius of approximately 1.5 - 2 cm. The grey region indicates our chosen range of level sets. For these simulations, we have **not** systematically optimized the penalty parameter. Doing so might lower the errors further. The observed L_B error is largest for the simulation started from the frontal Gaussian peak, possibly due to the high anisotropy in that region.

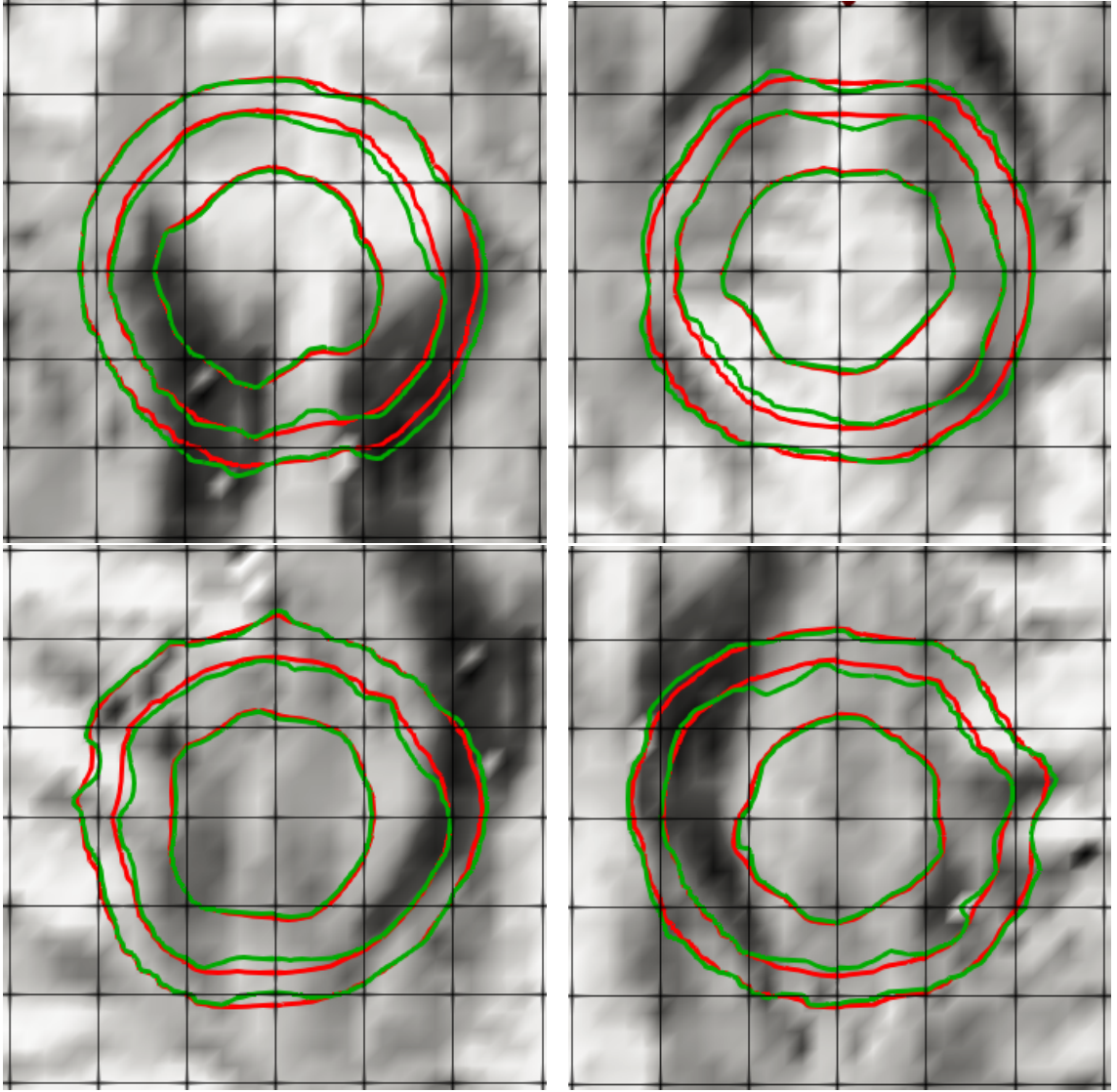


Figure 25: Comparison of level sets on forward solutions ($u(x, t_e) = 0.16, 10^{-2}, 10^{-3}$) shown in green and corresponding stationary solutions ($u_s(x) = 0.16, 10^{-2}, 10^{-3}$) shown in red. The background is given by the fractional anisotropy, color coded as in Figure 24. The indicated grid spacing is 1 cm. Four separate simulations were conducted with initial conditions in different positions (see Fig. 24). Top left: Final state of simulation with frontal initial condition. Top right: posterior initial condition. Bottom left : left initial condition. Bottom right : right initial condition.

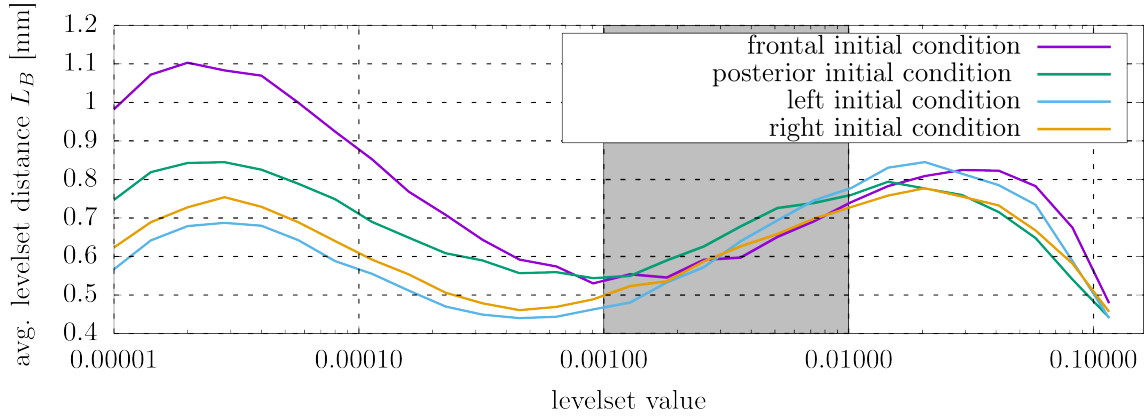


Figure 26: Logarithmic plot of the characteristic level set errors L_B as defined in Equation (4.17) for the four simulations presented in Figure 25. The grey region spans the two outer level set values used in this work of 10^{-3} and 10^{-2} . The error L_B should be interpreted as the expected distance between the level sets on the stationary solution to identical level sets on the forward simulations.

5 Implementation: The DUNE-glio module

Throughout the glioMath project, we developed the software module DUNE-glio within the distributed and unified numerics environment (DUNE) (Blatt et al., 2016). The codebase was used to produce the numerical results for Engwer and Wenske (2020), Corbin et al. (2020) and this document. One of the initial goals of the glioMath Project was to validate or falsify PDE tumor models with real patient data sets. The software project DUNE-glio was conceived to optimize for this use case. We now give a short overview over its capabilities, and the design decisions that were made in its implementation.

5.1 Features of DUNE-glio

The initial goal of validating forward models via medical dataset was considerably extended during the project. DUNE-glio is currently capable of:

- Reading DTI and SEG data sets from medical data formats (e.g., .nii, .dcm)
- Conducting forward simulations of PDE tumor models on real patient data sets
- Easy extension with new tumor models or numerical methods
- Switching between or comparing of different discretization schemes (MPFA, CFEM, DG, HFVM)
- Switching between implicit and explicit time-stepping schemes of different orders (e.g., implicit/explicit Euler, Runge Kutta methods (PDELab))

- Conducting stationary simulations as presented in Section 4
- Conducting automated comparisons between forward- and stationary formulations, as presented in Section 4.5.5
- Exporting simulation results back to medical data formats (.nii/.dcm)
- Conducting *automated* parameter and grid refinement studies via the `Study<...>` class
- Numerical verification of *all* implemented discretizations via time-dependent analytical solutions (e.g., comoving Gaussian diffusion kernel).
- Numerical verification of *all* implemented discretizations via stationary manufactured solutions, as presented in Section 3.4.

5.2 Software architecture

We now describe some design decisions that were made in the layout of the module. We limited our implementation to structured grids, as the medical data sets were available in structured voxel-based file formats. Since a typical data sets total number of voxels is approximately 1-5 million, a performant implementation was necessary. We made extensive use of static polymorphism via template programming. Also, the code is parallelized via functionality from DUNE-PDELab and the template solver library DUNE-istl.

The implementation of numerical methods was held modular in the sense that new discretizations can be easily added to the project, and one may conveniently switch between them to compare results. Similarly the implementation is separated into templated model-classes to allow more models to be implemented as soon as they are published. The interfaces of the numeric implementation classes (`LocalOperator`) and the classes defining the tumor model (`ModelCore`) have also been extended to systems of coupled PDE's for Corbin et al. (2020). Figure 27 provides an incomplete diagram of the most important classes within the module.

The DUNE-glio module is config-controlled via two external config files that need to be

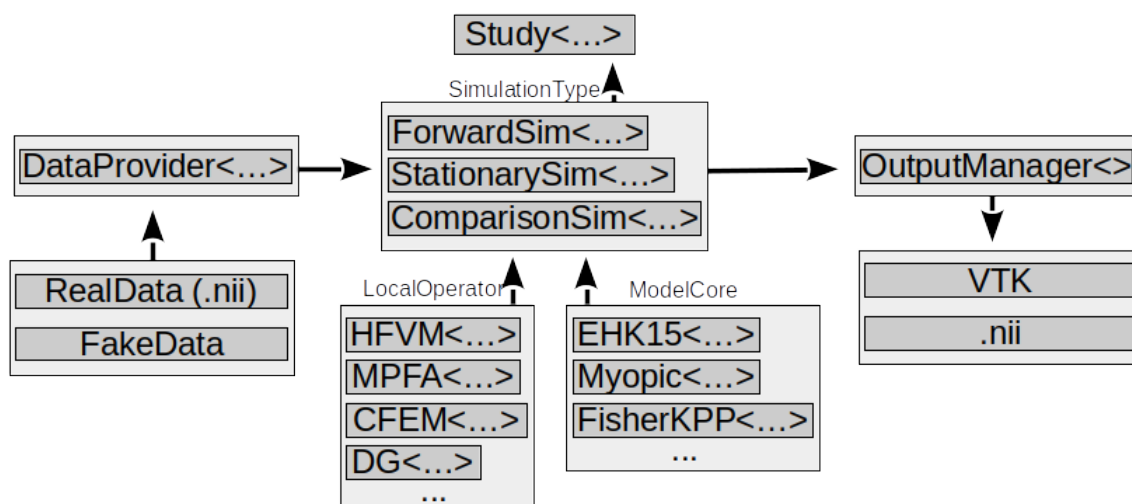


Figure 27: Schematic of the most important components of the DUNE-glio software module. The study class is templated with one of three simulation types, which themselves are templated by the used numerical discretization and the underlying physics (tumor) model. The DataProvider handles the the medical data set input (DTI, SEG), and the OutputManager handles the functionality of writing different file formats (.vtk , .nii).

provided as command line arguments. The first configuration file (`simConfig`) includes all information necessary to parameterize the tumor models, to state the intended simulation time and step-width, configure the solvers and select which output fields should be written. The second config (`dataConfig`) includes information on the underlying medical data set , e.g., total dimensions, voxel sizes and selected slice for 2D simulations.

The top-most class is the class `Study<SimType>`, templated with one of three simulation types. The `Study<SimType>` class offers the possibility to run parameter studies on model parameters, to successively refine the grid for convergence tests, or do simple forward runs or stationary simulations. The three currently implemented simulation types are a classical forward run (`ForwardSimulation<LOP, ...>`), a single stationary simulation (`StationarySimulation<LOP, ...>`) and a comparison of the two (`ForwardStationaryComparison<LOP, ...>`). Here, the template parameter `LOP` represents the local assembly procedure defining the numerical method (`LocalOperator`) . This numerical implementation is held separate from the tumor model definition (`ModelCore`) , to allow further extension with new models or discretizations. A class (`DataProvider<... , ...>`) allows easy switching from real patient data set scenarios to the numerous test cases with artificial underlying data. We will give a brief overview of the necessary preprocessing steps in Section 6.1.

The program layout, as just presented, allows to conveniently set up numerical experiments by providing the necessary components as template parameters. The following short example shows how a study may be set up, for a forward simulation, using the HFVM method and the haptotactic tumor model (EHK15Model, see (Engwer et al., 2015, 2016)).

```
1 //Define numerical discretization type (LocalOperator) and tumor model:
2 using HFVM_EHK15_LOP = HFVM_LOP<QKFEM1,EHK15Model,L2Op,GridType>;
3 //Define simulation type to be conducted:
4 using HFVM_EHK15_SIM = ForwardSimulation<EHK15Model,MBE,DataProvider,Grid
    ,1>;
5 //Create study object:
6 Study<HFVM_EHK15_SIM> study1(simConfigPath, dataConfigPath, mpiHelper);
7 //Start
8 study1.doStudy();
```

Dependencies

Many of these features are made possible by the inclusion of existing software packages. DUNE-glio uses the DUNE-grid module as a structured grid implementation (yasp-grid) (Bastian et al., 2008b,a). The module uses the assembler and the Newton implementation of the DUNE-PDELab module, as well as the constraints interface which was slightly extended to allow internal volume Dirichlet constraints (Bastian et al., 2010). The solver library DUNE-istl was used to allow convenient switching between parallel iterative solvers (Blatt and Bastian, 2007). Further we used components of DUNE-common, DUNE-geometry and DUNE-typetree.

There are some necessary external dependencies. We used the library ITK (McCormick et al., 2014), to allow handling of the medical data formats (.nii). For the implementation regarding the matrix Hölder mean and the log-Euclidian mean, we used the C++ template library **armadillo** for convenient matrix exponentiation and matrix-logarithms (Sanderson and Curtin., 2016; Sanderson and Curtin, 2018). We also used parts of the **Boost** C++ template libraries (Schling, 2011).

6 Application to real data sets

In this section, we present 3D results for the stationalized haptotactic model given in Equation (4.16a) on two real patient data sets. The results serve as a template of how the stationalization can be used in medical practice at the time of diagnosis.

First, the necessary pipeline to leverage the medical data set as well as the glioMath data set itself will be presented (Section 6.1). After this, numerical results for a parameterization with a low effective Péclet number will be presented in Section 6.2. The level set on the results for this low-Péclet parameterization effectively reproduce the current medical treatment recommendations of treating a fixed size radius. They illustrate how automated assistance in the treatment radius planning which is based on PDE models may look like. In Section 6.3 these results are compared with solutions for an altered parameterization with higher effective Péclet-Number. This direct comparison indicates what effect increasingly strong advective effects have on the prediction radii of the level sets. It also proves that the stationalization approach could offer *new* qualitative information to medical practitioners that extends the current recommendations.

6.1 The glioMath data set

The data sets for the glioMath project were kindly provided by the *Klinik für Strahlentherapie und Radioonkologie (Universitätsklinikum des Saarlandes)* in the course of the glioMath project (Surulescu, 2016). They were selected from a large pool of patient data by Sven Knobe. The data set consists of 15 patient DTI scans and their corresponding medical segmentations that were automatically generated (see Section 1.1). They allow to run forward simulations in both the *ab initio* and the post-diagnostic setting mentioned in Section 1.3 and are fully accessible to the DUNE-glio module. The data sets also allow for calculations of the stationary approximations. Table 10 indicates the data set labels, their

sizes via total number of voxels as well as the volume of the segmented tumor. The total number of voxels includes the background outside of the brain.

Data set	Voxel	Tumorous seg. volume [cm ³]
#3	2236520	200.5
#5	1905396	40.3
#8	2083770	174.1
#12	1702362	96.9
#14	1286775	140.1
#17	1085952	105.6
#21	1298830	69.8
#22	1974357	117.3
#25	2442600	53.3
#29	5293746	122.1
#31	3691464	113.7
#37	2314656	226.3
#40	2027718	219.1
#42	2039512	34.4
#43	1428546	51.6

Table 10: The glioMath data set consisting of 15 pairs of DTI and corresponding segmentation data. Gender and age of subjects is unknown.

6.1.1 Data preparation

The resolutions of the raw MRI data sets from which the segmentations are derived, are typically higher than the resolutions of the raw DTI data sets. The reason for this is that the time necessary to take a DTI data set is significantly longer than for a single MRI scan. Within the medical data sets there are metadata fields describing additional information. These data fields can include the handling practitioner, the institution, dates and time, information on the scan sequence, the image resolutions and most importantly information on the machine coordinate system and the offset of the scanned region. However, many of the metadata entries are anonymized. Each DTI data sets consist of 12 low resolution MRI scans, each measuring the approximately water diffusivity in one spatial direction.

For these data sets great care has to be taken that the information describing the orientations ('*b-vectors*') in which each of the 12 or 16 individual scans are taken is correct and fits the machine coordinate system. Out of this raw data, the best fit approximation for the local water diffusion tensor is reconstructed. We made use of the software *camino* for the purpose of DTI reconstruction (Cook et al., 2006). Unfortunately, the bounding boxes of the measured domains, as well as the data set resolutions generally do not match from patient to patient, or between the two modalities. This resulted in considerable effort to preprocess the raw data into useful formats. To bring the DTI and segmentation data sets onto grids with equal resolution the DTI and segmentation data sets were interpolated individually onto an equally spaced grid. We made heavy use of the C++ library ITK (McCormick et al., 2014) to read, write and rescale the medical data formats. After this step, the segmentation data was registered with the DTI data sets and not vice versa to not disturb the relationship between the DTI grid orientation and the measurement orientations ('*b-vectors*') used in the DTI reconstruction. After the reconstruction both the DTI data sets and the segmentation information are aligned and on equal grid spacings. We used the software Slicer (Kikinis R., 2014) for 3D visualization and, more importantly, the linear registration of any two medical data sets. Slicer offers the functionality to register two data sets residing in different grid orientations and resolutions with each other. This makes it possible to find, save and exchange the relative coordinate transformations so that the numerical simulation results are useful to the medical practitioners. In practice it was important to replicate the data orientation and file formats originally used by the medical institution. The transformations mapping the numerical results back to the coordinate system used by the project partners are part of the glioMath data set.

The numbering of the data sets is non-consecutive. This is because in the selection process several data sets had to be excluded from the set. The reasons for exclusion were stated by our project partners to be prevalent imaging artifacts or missing segmentation information. The preprocessing differed slightly for each pair of DTI + SEG, but it can be grouped into roughly five steps. For each step, the software that was used is indicated.

1. Interpolation of raw data (DTI + SEG) onto equal resolutions: ITK, (McCormick et al., 2014).
2. Reconstruction of the water diffusion tensors from raw images: *camino*, (Cook et al., 2006).

3. Alignment of medical segmentation with reconstructed DTI data set: *Amide*, (Loening and Gambhir, 2003).
4. Cropping the background of aligned DTI and segmentation data sets : *Amide*, (Loening and Gambhir, 2003).
5. Reconstruction of the transformation necessary to map numerical results back to segmentation machine coordinates: *Slicer*, (Kikinis R., 2014).

In the glioMath dataset, we provide all preprocessed anonymized files with individual notes on how each of them was reconstructed. As of now, the resulting DTI + SEG combinations are all readable by the DUNE-glio module and accessible for numerical simulations.

6.2 Numerical results

We now present numerical results on two real patient data sets. To keep the presentation concise, we chose two data sets with good resolution and reconstruction quality (#29, #31), and discuss them in detail. For these simulations, we set up a domain with the grid spacings and the dimensions of the medical data sets (DTI, SEG). Here, the simulation domain Ω_b is the brain with no-flux boundary conditions at the outer brain border. We use the tumor surface of the medical segmentations as the internal Dirichlet side condition (Eq. (4.16c)) for the stationary simulation and calculate the solution to the stationalized haptotactic model (4.16a) directly. For these simulations we used the parameters from Table 9. No forward simulations are conducted here, for the reasons stated in Section 1.3. It is assumed that the outer extent of the medical segmentations represents the visibility threshold. As an internal Dirichlet constraint we assign the approximate tumor density values of the different segmented tissue types (see Table 1). To visually present the tumor density at the border and outside of the segmentation, we indicate three level sets on the solution at $u_s(x) = 0.16$ (blue), $u_s(x) = 10^{-2}$ (red) and $u_s(x) = 10^{-3}$ (green), so that the innermost level set indicates the Dirichlet constraint in most cases, and the outer two level sets may be interpreted as suggested treatment radii (CTV as defined in Section 1.1). The rare cases where the internal Dirichlet constraint and the level set at $u_s(x) = 0.16$ do not align will be discussed in Section 7.2. The two sample results of the data sets #29

and #31 are shown in Figures 28,29, 30 and 31 . We selected two data sets with good resolution and reconstruction quality, as we mainly want to present the capabilities of the stationalization method, and not make any statements about the whole cohort. Figure 28

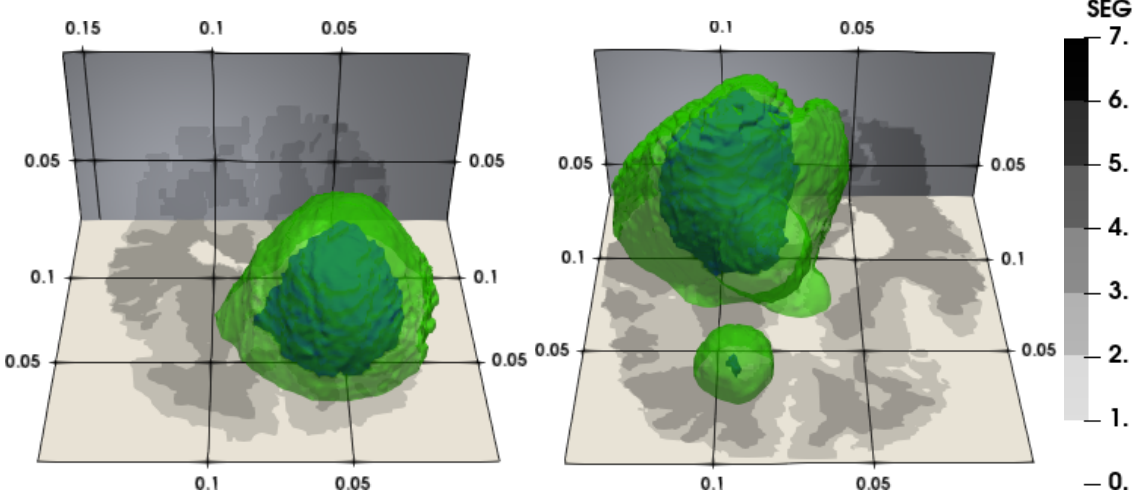


Figure 28: 3D frontal top down view of data sets #29 (left) and #31 (right) with level sets on the numerical solution to the stationalized problem formulation (4.16a) with parameters from Table 9. The axial and frontal planes indicate the medical segmentation as defined in Table 1. For better visibility we show only two level sets at $u_s(x) = 0.16$ (blue) and $u_s(x) = 10^{-3}$ (green). Data set #31 contains distinct metastatic volumes that are not connected. Indicated scale is in meters.

presents 3D level sets on the stationary solutions for two data sets in a frontal view. The two flat surfaces cutting through the tumor volume are the axial plane and a frontal plane indicating the tumor segmentation data. For visibility reasons we only show two level set surfaces. The blue inner level set $u_s(x) = 0.16$ describes the surface enclosing Ω_i where we assigned Dirichlet conditions. The green level set $u_s(x) = 10^{-3}$ has a smooth surface encircling the bulk tumor. In the 3D view of data set #31 on the right it is visible that the outer level set encloses both the primary tumor volume, as well as a secondary metastasis in the foreground. This indicates that the stationalization for this low-Péclet number parameterization is robust even for quite eccentric tumor geometries. We will discuss the increased modelling error for small metastatic cases in Section 7.2.

Figure 29 shows 2D axial slices through the simulated tumors. In these 2D representations we show three level sets. The innermost blue level set again indicates the internal constraint, and the red $u_s(x) = 10^{-2}$ and green $u_s(x) = 10^{-3}$ level sets indicate the diminishing tumor cell density away from the bulk. For the chosen set of parameters, the invasion radius indicated by the level sets is quite smooth. Our particular choice of level

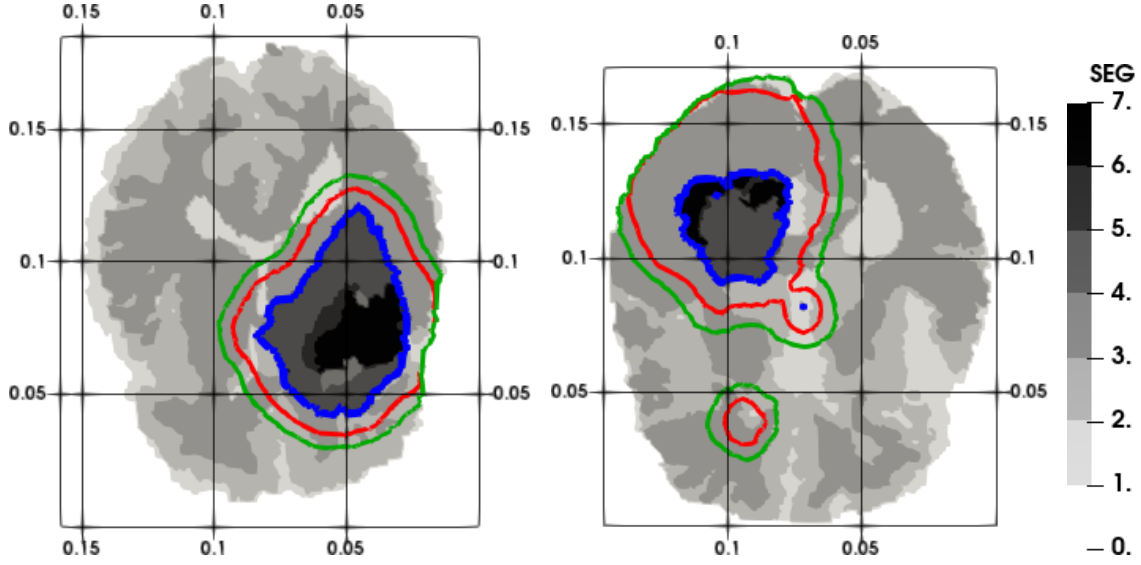


Figure 29: Axial view of the medical segmentation (gray), level sets at the internal constraint $u_s(x) = 0.16$ (blue), at $u_s(x) = 10^{-2}$ (red) and at $u_s(x) = 10^{-3}$ (green). The volume encircled by the level sets approximately reproduces the 2 cm radius used in medical practice (Chang et al., 2007). Left: patient #29. Right: patient #31, the medical segmentation includes distinct metastases which are not connected.

set values is somewhat arbitrary but helps to assess the relative risk of tumor progression. Contrary to the forward scenarios, the information they provide can be interpreted. They mark the locations at which the stationalized tumor model formulations predict a particular volumetric tumor cell density at the time of diagnosis, so in our case that location where 1% and 1‰ of the volume is filled with tumorous cells.

On the left side of Figure 29 showing data set #29 one may observe that the level sets touch the outer boundary of the brain. Here, no gain is to be expected in advising the treatments but it is assuring that there are no artifacts at the boundary of the brain. It is also visible that the segmentation classifies a high density region (Enhancing, Non-Enhancing) up until the border of the bulk tumor.

In the right side of Figure 30 one may observe how distinct metastatic tumor volumes influence the stationary solution. The effects of a metastasis lying exactly within this slice (right) and closely below the slice are visible (middle). In situations like this the internal surface $\partial\Omega_i$ is not connected, and the Dirichlet constraints have to be applied accordingly. In the frontal view of the results presented in Figure 31 one may observe how strongly any two tumors may differ. While the center of the tumor bulk in data set #29 has a distinct

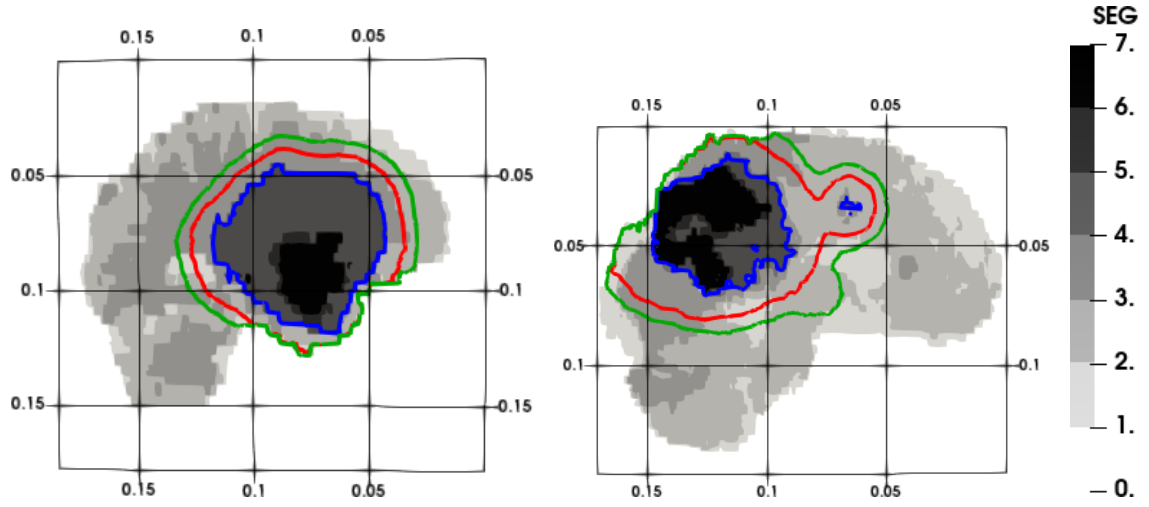


Figure 30: Sagittal view of the medical segmentation (gray), level sets at the internal constraint $u_s(x) = 0.16$ (blue), at $u_s(x) = 10^{-2}$ (red), $u_s(x) = 10^{-3}$ (green). Left: results for patient #29. Right: results for patient #31, where the medical segmentation includes a distinct metastasis which is not connected to the bulk.

core of tumorous tissue segmented as enhancing or non-enhancing, the center of the bulk of the tumor visible in data set #31 shows a clear necrotic core. The results presented here were calculated for a parameterization which resulted in comparatively weak advective effects.

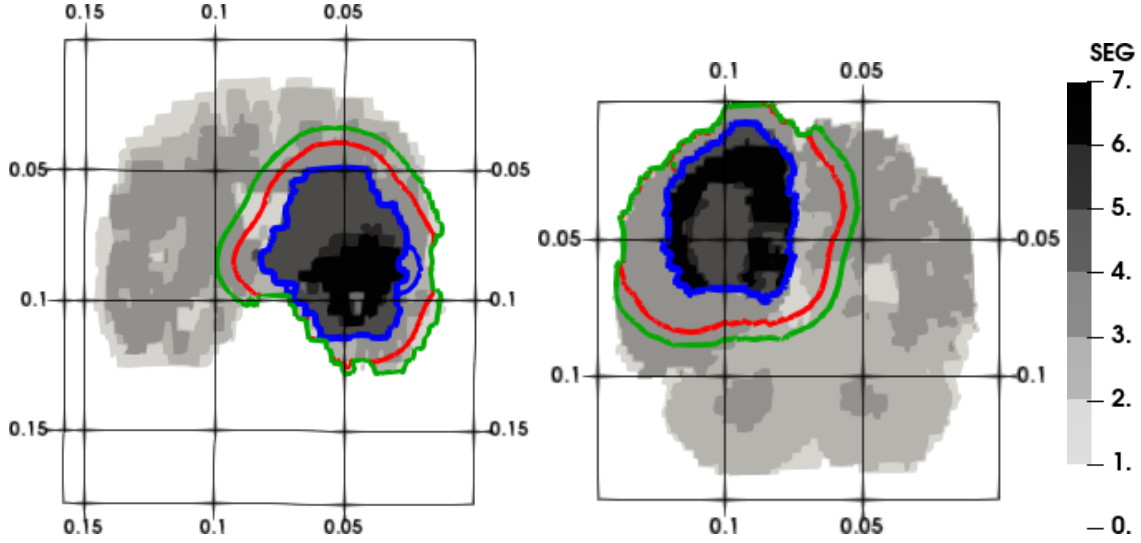


Figure 31: Frontal view of the medical segmentation (gray), together with level sets at the internal constraint $u_s(x) = 0.16$ (blue), at $u_s(x) = 10^{-2}$ (red) and at $u_s(x) = 10^{-3}$ (green). Left: stationary Simulation results for patient #29, at the right side of the tumor, the density assigned via the segmentation is higher than the assumed visibility threshold resulting in an extension of the blue level set. The volume encircled by the level sets mostly reproduces the 2 cm radius used in medical practice. Right: results for patient #31

6.3 Comparison via Péclet numbers

The results from Section 6.2 indicated relatively smooth level set surfaces surrounding the tumor and the level set predictions were similar to those recommended to the medical practitioners (1.5 - 2 cm radius). To present how the stationalization could actually offer *improved* recommendations compared to the current practice we now present a direct comparison using a parameterization that is changed towards a higher influence of the haptotactic and myopic advective terms.

We will critically discuss the applicability of the stationalization in the presence of significant advection in Section 7.2. We again show results from data sets #29 and #31 as there the resolution and DTI reconstruction quality is of high quality, and the effects are most visible. The parameterization for the case with higher effective Péclet number is listed in Table 11. For the simulation with low effective Péclet number we reuse the parameters from Table 9. A direct comparison of the two results is presented in Figure 32 where the level sets on the solution to the problem with a low-Péclet number parameterization ($u_s(x) = 10^{-2}$ and $u_s(x) = 10^{-3}$) are shown in white. Here the innermost level set has a higher value with the outer one having the lower one. The level sets on the high-Péclet

parameter	value
s	1e-6 [$\frac{m}{s}$]
ρ	8.44e-7 [$\frac{1}{s}$]
R_0	5e3
λ_0	0.1 [$\frac{1}{s}$]
λ_1	1e-2 [$\frac{1}{s}$]
k_+	0.1 [$\frac{1}{s}$]
k_-	0.1 [$\frac{1}{s}$]
v	$\frac{5}{\sqrt{6}}$

Table 11: Parameters used for the 3D stationary simulations of model (4.16a) resulting in an effective Péclet number $Pe \approx 1$.

number solution of same values are presented in black. The level set $u_s(x) = 0.16$ marking the shared internal constraint is marked in blue. By comparing the inner black and white suggested radii we may observe the *additional* information the stationalization can offer. Wherever the black lines overextend the more conservative white configuration the treatment radii could be extended, and more importantly, wherever the black lines lie inside of it, tissue might be spared the destructive effects of treatment. The same holds true for the black and white level sets of lower amplitude lying more distant from the tumor core.

An important result in this regard is, that the retraction or the extension recommended by the level sets is plausible, even though the derivation of the penalty term did not include them. When comparing the results for the two parameterizations, we see that the high-Péclet level sets recommend extension of the treatment radius in regions with high fractional anisotropy like white-matter tracts, and also recommend retraction of the treatment radius where the diffusivity and FA is reduced (e.g., gray matter). These results seem to prove that the stationalization may offer *qualitative* information to the medical practitioner even if we overextended our initial assumptions.

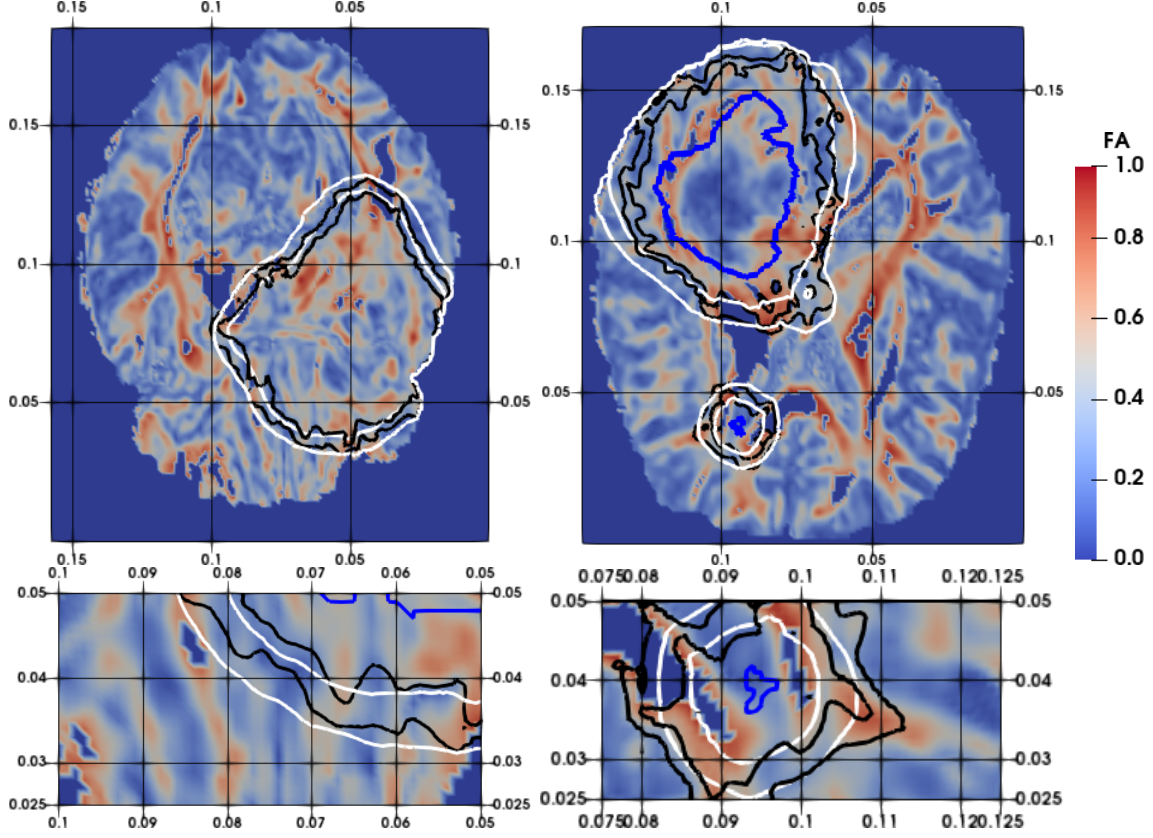


Figure 32: Top: axial slices of data sets #29 ($z = 0.089$ m, left), #31 ($z = 0.06$ m, right). The coloring indicates the local fractional anisotropy (FA), see Equation (2.27). Level sets $u_s(x) = 10^{-2}$ and $u_s(x) = 10^{-3}$ of the low Péclet number parameterization (Table 9) (white) and the high Péclet number parameterization (Table 11) (black), as well as the internal constraint (blue) are overlayed. Bottom: Zoomed view of smaller regions with the two level sets. The stronger the influence of the advective terms of the haptotactic model, the more pronounced are the extensions and retractions of the treatment radii suggested by the level sets.

7 Discussion and outlook

In this work we addressed the research question of how mathematical modeling and numerical simulations may aid in the treatment of GBM. In the following we discuss the two approaches we presented. Following the order of the document, we first discuss the Hölder finite volume method and formulate directions of possible further research in Section 7.1. We discuss the stationalization procedure, its applicability and shortcomings in Section 7.2 and also suggest avenues of further improvement for the stationalisation procedure.

7.1 Hölder finite volume method

7.1.1 Discussion

We introduced the generalized matrix Hölder mean into the flux discretization of a vertex-centered finite volume method and investigated which Hölder parameter $\alpha \in \mathbb{R}$ is optimal for our use case of GBM modeling. The vertex-centered finite volume construction was mostly canonical with the main novelty being the inclusion of the matrix Hölder means. For the numerical investigation of the method we used parameterized manufactured solutions which allowed the measurement of how the spatial variance of the diffusivity field influences the numerical precision of the resulting schemes. The results suggest that the choice of average has significant impact on the accuracy of the solution, depending on the underlying diffusion tensor field. The convergence plot of the combined inhomogeneous anisotropic case (Fig. 16) indicates that in certain situations the error may be reduced by orders of magnitudes by simply adjusting the Hölder parameter α . The convergence results for the manufactured solutions show that the Hölder method with $\alpha \rightarrow 0$ resulting in a log-Euclidian matrix interpolation *outperforms* the industry standard MPFA-O method in all nontrivial test cases we investigated. In direct comparison the HFVM method also offers

other advantages over the MPFA-O method. The MPFA-O method is essentially bound to grids with solely hexahedral *or* tetrahedral elements which are not mixed with other cell geometries. In a mesh with mixed elements, the construction of the interaction region and consequently the setup of the local system of equations would be severely complicated. In that case many special combinations of adjacency would have to be considered.

The Hölder finite volume method does not have these restrictions. The only prerequisite for a correct flux reconstruction within any primal grid cell is that the diffusivity matrices are known at the corner points of a local Lagrange base. That means that the presented method of estimating $\mathbf{D}_\alpha(x)$ can be used directly in conforming finite element methods as well as discontinuous galerkin methods. No information from the neighboring cells is needed. This allows for simple integration of the matrix Hölder average into software implementations that already use a cell-based assembly. The matrix Hölder mean is essentially independent of the particular discretization strategy. Since the Hölder averaging of the diffusion matrices leads to reasonable flux densities at *any* point within a primary cell the incorporation into cut-cell type discretizations should also be straight forward. Contrary to the MPFA-O method, the HFVM makes explicit statements about the interpolated diffusivity field, making it more suitable for further analysis.

We also see advantages from the more pragmatic perspective of software engineering. The Hölder averaging of $\mathbf{D}_\alpha(x)$ can be encapsulated into a single templated C++ method taking three arguments. These are the scalar Hölder parameter α , one variable length C++ container with the contributing matrices \mathbf{D}_i and one with their weights given by the base evaluations. It may therefore be added to existing codebases without significant changes to the software architecture. No extra work is needed for changing the dimension of the interpolation from 2D to 3D, or switching from hexahedral to tetrahedral geometries.

The numerical cost of the presented method is of same order as the MPFA-O method. In the MPFA-O method a local system is solved for every interaction region. In the HFVM one has to evaluate the matrix mean at the flux quadrature points, which generally entails the calculation of matrix exponentials. As an exception to the rule we find that for $\alpha = 1$, i.e., the arithmetic mean between the matrix components, no matrix exponentiation has to be performed. The effective stencil size is identical in both methods (2D: 9 row entries, 3D: 27 row entries). All Hölder averaging may be conducted in advance of time-dependent simulations given that the material properties and grid geometry do not change. The implementation of the matrix Hölder mean is comparatively simple as many linear algebra libraries provide efficient eigendecompositions.

The presented HFVM method includes important corner cases in a single framework. Even

if the question of the appropriate mean can be answered in the scalar diffusivity case, the straightforward extension of the harmonic mean to higher dimensions ($\alpha = -1$) does not provide optimal results. The results suggest that contrary to intuition the method with a Hölder parameter of $\alpha = -1$ does not perform well. For the d-linear weights we chose, a Hölder mean with $\alpha < 0$ suppresses *all* subfluxes within a voxel as soon as one contributing diffusion matrix has a diminishing Frobenius norm.

On the other hand, we confirmed the swelling effect for $\alpha \geq 1$ (see Fig. 11) where the determinant of the interpolated diffusion matrices swells in between the given datapoints. We have consistently observed the best performance of the HFVM for $\alpha \rightarrow 0$. This resulted in our choice of the log-Euclidian interpolation as given in Equation (3.11).

Some shortcomings of our numerical set up need to be pointed out. One problem of the manufactured solutions method is that the construction of analytical test cases with discrete steps in diffusivity is hard. We were able to construct analytical solutions for the imposed diffusivity field because we used smooth and easily differentiable trigonometric functions (see Section 2.6). If the diffusivity field had discontinuities, then the reconstruction of the necessary reaction term would be further impeded. Eigestad and Klausen (2005) claim to have found a radial analytical solution where homogeneous blocks of differing isotropic diffusivity touch. A numerical test based on such a solution could be beneficial in the choice of the optimal Hölder parameter for other numerical applications. In such a setup the HFVM could be investigated for cases with discontinuities that are not covered by our tests. The stated solution in Eigestad and Klausen (2005) however does not describe anisotropy. Analytical solutions of discontinuous diffusivity fields that are also anisotropic have not been identified to the best of our knowledge. Consequently, it is questionable whether the inhomogeneous anisotropic manufactured solutions presented in this document and the conclusions made based on them are truly representative of *all* real world cases. We therefore refrain from making any general optimality statement for the log-Euclidian interpolation but want to conclude that it outperforms the MPFA-O method and other Hölder interpolations for smooth underlying diffusivity fields. At this point we also make no statements about the stability regions of the two methods.

7.1.2 Outlook

Intuitively, one might expect that since the choice of the harmonic average is so common in the isotropic TPFA discretizations, the optimal choice for the matrix Hölder mean

should be that of $\alpha = -1$. In our construction this choice would lead to the total suppression of all subfluxes within a cell, as soon as one corner diffusivity vanishes. This could be overcome by modeling a piecewise constant weight function $w(x)$ instead of the d-linear version we chose earlier. With such a weight function, only the diffusivities of the vertices closest to a subinterface would contribute and not all vertex diffusivities of a given primary discretization cell.

In the testcases presented in this document the Hölder parameter was always set globally. There should be room for improvement when the Hölder parameter is adjusted locally to reflect *a priori* knowledge of a certain part of the simulation domain. In some applications it is known *a priori* that the underlying diffusivity field can be modeled as smooth and relatively homogeneous in some regions of the domain, while it is expected to have strong inhomogeneities at some internal interfaces. Examples of this could be a diffusing chemical passing through a sudden jump between two otherwise homogeneous materials or liquid flow through cracked rocks. In a geological settings where the interest lies in fluid flow close to an impermeable layer (groundwater flow), one may employ a restrictive $\alpha = -1$ method at these interfaces. In a case where the diffusive coefficients vary comparatively slowly, we may choose a $\alpha \geq 0$ method.

It should be possible to codify these assumptions into a local function $\alpha(x)$. Doing that would allow for maximum use of a-priori information on the simulation domain.

In our use case, it should be possible to adjust the parameter wherever jumps in segmentation label occur, so that the method is more robust in those regions of strongly varying diffusivity. There should also be no danger of loss of convergence since for finite α the mean will still be between the minimum and maximum of the set of diffusion matrices and should therefore converge to the same solution upon dataset refinement.

7.2 Stationalization

7.2.1 Discussion

We derived a nonlinear penalty term for the 1D Fisher-KPP equation, that allows to calculate a limit wavefront at the location of pinning constraints. Since this derivation was done in nondimensionalized form it is valid for all reasonable ratios of diffusivity and growth rate.

We extended the stationalization to an anisotropic model to investigate its applicability for non-homogeneous media. The results presented in this work as well as in (Engwer and Wenske, 2020) strongly suggest that the stationalizations derived by our method might provide good approximations even in these inhomogeneous anisotropic cases. We compared the prediction of a recent tumor forward model including haptotactic effects with its stationalized formulation on a data set of a healthy subject and established that the errors are acceptable ($L_b < 2$ mm). Finally, we presented numerical results on real 3D patient data sets. We first presented results for two real patients for a low-Péclet parameterization. These results indicate that as a first step the method may be used to reproduce the marking of a 2 cm treatment radius.

One important aspect is, that the indicated radius can be calculated *automatically* from the medical data, is reproducible and does not suffer from human or institutional biases. We also presented a comparison with results for a parameterization with higher effective Péclet number that suggested how the stationalization may be used to advise retraction or extension of the treatment radius. This qualitative information is currently not available in medical practice.

For the numerical simulation of forward PDE models for GBM, many intermediate states have to be calculated to make a prediction on the final state of tumor invasion. If one were to use the forward model to make actual predictions in a medical case, then the stepwidth would have to be chosen sufficiently small, so that the cumulative error arising throughout the sum of the steps remained justifiable. This constraint on the timestep, which depends on the tumor model, its parameterization and data set resolution could make the calculations prohibitively expensive to run on consumer hardware. The fact that for the stationalized problem formulation only *one solution* has to be calculated makes the procedure orders of magnitude cheaper in computation. This means that treatment radius recommendations can be made within minutes on a consumer hardware vs. several hours on a research cluster. This performance advantage could have significant impact on possible clinical studies or subsequent application.

Even if the presented form of stationalization is well aligned with the available data, we want to discuss some of the shortcomings of the procedure. In the presented stationalization approach we made maximal use of the information encoded in the medical segmentation. This information is invaluable, but may itself introduce inconsistencies. A rough estimate of the tumor volume percentage attributed to the different compartments is listed in Table 1. This attribution may lead to the following situation. In the case of tissue segmented as non-enhancing or enhancing we assign the densities 0.8 or 1.0. If these segmented volumes touch the outer surface of the bulk tumor and are not encircled by edema (density: 0.16),

then we have assigned the outer visibility surface with a density value much higher than the previously assumed visibility threshold of $u_s(x) = 0.16$. In that case we may still calculate a solution to the stationalized problem formulations, but their predictions will result in the level set surface of the visibility threshold outside of the internal Dirichlet boundary condition. This would mean that the stationalized problem formulation will place the visibility threshold outside of its internal constraint, which we previously assumed to be the visibility threshold.

This inconsistency can almost certainly be attributed to malperformance of the automatic segmentation algorithms in conjunction with the limited imaging resolution. It seems unlikely to have discrete steps in tumor density from 0.8 to below 0.16 within real patients. A sample of this artifact is visible in the frontal slice of the tumor bulk in Figure 31. Here, the innermost blue level set represents the internal constraint at the tumor border, and the outer a the level set $u_s(x) = 0.16$ of the numerical solution.

We presented a comparison between solutions for two different problem formulations in Section 6. Increasing the influence of advective effects allowed us to make qualitative predictions about where the treatment radius might be retracted or extended. At this point we can not quantify how large the advective effects can be before the predictions become invalid. We expect bifurcations leading to more solution branches than the OMS/IMS discussed in Section 4.3.1 when the advective amplitudes are increased even further. The reason for this is that the advective fields $b(x) \in \mathbb{R}^d$ in many of the multiscale models are not solenoidal, i. e., $\nabla \cdot b(x) \neq 0$. If the vector fields exhibit sources with $\nabla \cdot b(x) > 0$ then the advection alone may allow new localized peaks of tumor density next to the trivial solution. The lack of the solenoidal property is also problematic outside of the context of the presetned stationalization, as without it the vector fields spuriously destroy or create tumor mass even in absence of reaction terms. The problem is intrinsic to the tumor models, and can not be remedied by the numerical discretization. We therefore advise caution when extending the procedure to advection dominated parameterizations and models.

7.2.2 Outlook

Our primary focus in this work was to investigate the viability of the stationary approximations of the tumor densities outside of the visible center. So far all numerical tests we conducted for low-Péclet parameterizations indicated that the resulting errors are reasonable, i.e., $L_b \leq 2$ mm.

With the applicability established, the logical next step seems to be to firstly compare the

predictions of more models against each other and secondly, to directly compare the delineation of treatment radii gained from the level sets with those that are used in medical practice. The presented approach allows to calculate numerical results that are *interpretable* as an expected tumor density distribution outside of the visible region at the time of diagnosis. This is exactly the information that the treatment recommendations of the medical institutions encapsulate in their recommended 2 cm treatment radii. It would be interesting to receive feedback from medical doctors about this new approach. In the future it might be possible to advise medical treatment on an automated patient-by-patient basis via the presented methods. All the necessary computational steps have been established as a proof-of-concept.

In our stationary numerical simulations, we have set the penalty parameter $v \in \mathbb{R}$ to a globally constant value. It may be possible to produce even better reconstructions of the forward profile when adjusting this penalty depending on the local diffusivity $\mathbf{D}(x)$. Since we expect the invasion to be faster in regions of high diffusivity, the penalty parameter could be adjusted accordingly. We have not conducted tests in this direction, but believe that such an extension may be beneficial.

We have presented the stationalization in the context of tumor invasion but it might be applicable in other fields as well. The problems most closely related are other invasive tumors like liver or lung cancer. The possible applications are essentially all those problems that can be modeled via the Fisher-KPP equations and include some form of thresholded imaging data, examples of which are bacterial growth, invasive species, chemical reactions (combustion) and wildfire modeling.

In the introduction we mentioned a series of publications on the stationary modeling of brain tumors (Konukoglu et al., 2006, 2010, 2007). Their mathematical approach via anisotropic eikonal equations was quite different from our forward modeling, but not less promising. So far, we were not able to reproduce their results due to the necessity of another numeric implementation. However, it should be quite interesting to compare their approach to the one we presented. It might also be fruitful to investigate the differences and commonalities of these two approaches from a purely mathematical perspective.

The limit wavespeed of the analytical solution used to derive the analytical penalty term is $\tilde{v} = \frac{5}{\sqrt{6}}$. For the inhomogeneous cases the question of an optimal penalty, i.e. one that minimizes the distance of the stationalized solution and the real underlying tumor density distribution, is not straightforward. This is because the effect of the anisotropic inhomogeneous diffusion on the limit wave speed is nontrivial. So far, we have not made systematic efforts to optimize the penalty parameter on a case-by-case basis but the errors we presented could be reduced further by optimizing the penalty parameter v to minimize

the level set errors L_B .

One of the assumptions that makes the stationalization viable is that we assume that the tumor invasion front is close to equilibrium. When that is the case the gradient statistic will be close to that one which we may derive from the Fisher-KPP equation. Considering the two small metastases outside of the bulk tumor visible in Figure 31, we have to admit that for these small volumes this condition is probably not met. Strictly speaking, we may not assume that the front shape has reached its quasi-stationary sigmoidal form for small and isolated metastases and therefore must assume that for them the predictions will have increased systematic error.

One of the underlying effects delaying the convergence to the limit propagation speed is due to curvature. The radial part of the Laplace operator in spherical coordinates is $\Delta_r = \frac{\partial^2}{\partial r^2} + \frac{2}{r} \frac{\partial}{\partial r}$. The second term can only be neglected for large radii r which in the case of radial expansion correspond to large times t . The problem was addressed by Konukoglu et al. (2010). They improved the estimation of the front speed from the constant limit value $v = 2\sqrt{D\rho}$ by including a time dependent correction term $v(t) = 2\sqrt{D\rho} - \frac{3}{2t}\sqrt{\frac{D}{\rho}}$. The inclusion of such a correction into the stationalization should be straightforward. However, this correction would reintroduce the problem of having to quantify the elapsed time since carcinogenesis, one of the problems which motivated our stationary modeling in the first place.

In future studies, it should be possible to establish practical bounds for the applicability of the stationalization in the presence of advection. We expect that the procedure will give good results if the advective fields within the models are comparatively small but expect some form of breakdown for completely advection-dominated cases. In the derivation of the penalty term we implicitly assumed that the tumor front shape is approximately sigmoidal. For advection dominated problems the assumption may break down. These practical bounds of applicability could essentially come down to an upper bound for the effective Péclet number of any given model and parameterization.

The cohort study done by Stensjøen et al. (2015) indicated that the observed growth rate is slower for larger tumors than it is for smaller ones. They interpreted this result in favor of a Gompertz growth law $f_g(u) = -\rho u \ln(u)$ describing the tumor growth rate which is different to the logistic one $f(u) = \rho u(1 - u)$ we used in this document. The different growth terms for tumor models are discussed in (Patel and Hathout, 2017). We see no argument why a similar stationalization should not be possible for tumor models with this growth law. The reason for this is that the Gompertzian reaction term has the properties demanded of the Fisher-KPP model class with limit solutions, i.e., $f'(0) \geq 0, f(u) > 0 \forall x \in (0, 1), f(1) = 0$. The theoretical results for the Fisher-KPP equa-

tions predict a limit solution of constant speed. If the tumor models show invasion profiles that stay constant in shape, then the necessary penalty term should also be accessible for derivation or numerical estimation. Unfortunately, we are not aware of any analytical solutions for the Fisher-KPP equation with Gompertzian reaction term that would allow the analytical derivation of the penalty. However this should be no obstacle to numerically *measure* the analogous penalty term. To do this one would only need to record the observed gradient distribution of the limit shape for a Gompertzian model at large simulation times.

8 Bibliography

- I. Aavatsmark, T. Barkve, Ø Bøe, and T. Mannseth. Discretization on non-orthogonal, quadrilateral grids for inhomogeneous, anisotropic media. *Journal of Computational Physics*, 127(1):2 – 14, 1996. ISSN 0021-9991. doi: <https://doi.org/10.1006/jcph.1996.0154>. URL <http://www.sciencedirect.com/science/article/pii/S0021999196901540>.
- I. Aavatsmark, G. T. Eigestad, R. A. Klausen, M. F. Wheeler, and I. Yotov. Convergence of a symmetric mpfa method on quadrilateral grids. *Computational Geosciences*, 11(4): 333–345, Dec 2007. ISSN 1573-1499. doi: 10.1007/s10596-007-9056-8.
- Ivar Aavatsmark. An introduction to multipoint flux approximations for quadrilateral grids. *Computational Geosciences*, 6(3):405–432, Sep 2002. ISSN 1573-1499. doi: 10.1023/A:1021291114475.
- Mark J. Ablowitz and Anthony Zeppetella. Explicit solutions of fisher’s equation for a special wave speed. *Bulletin of Mathematical Biology*, 41(6):835–840, Nov 1979. ISSN 1522-9602. doi: 10.1007/BF02462380.
- Andrew L. Alexander, Jee Eun Lee, Mariana Lazar, and Aaron S. Field. Diffusion tensor imaging of the brain. *Neurotherapeutics : the journal of the American Society for Experimental NeuroTherapeutics*, 4(3):316–329, July 2007. ISSN 1878-7479. URL <https://pubmed.ncbi.nlm.nih.gov/17599699>.
- JCL Alfonso, Talkenberger K, Seifert M, Klink B, Hawkins-Daarud A, Swanson KR, Hatzikirou H, and Deutsch A. The biology and mathematical modelling of glioma invasion: a review. *J. R. Soc. Interface.*, pages –, 2017.
- Douglas N. Arnold, Franco Brezzi, Bernardo Cockburn, and Donatella Marini. Discon-

- tinuous galerkin methods for elliptic problems. In Bernardo Cockburn, George E. Karniadakis, and Chi-Wang Shu, editors, *Discontinuous Galerkin Methods*, pages 89–101, Berlin, Heidelberg, 2000. Springer Berlin Heidelberg. ISBN 978-3-642-59721-3.
- Vincent Arsigny, Pierre Fillard, Xavier Pennec, and Nicholas Ayache. Geometric means in a novel vector space structure on symmetric positive-definite matrices. *SIAM Journal on Matrix Analysis and Applications*, 29(1):328–347, 2007. doi: 10.1137/050637996. URL <https://doi.org/10.1137/050637996>.
- S.W. Atlas. *Magnetic Resonance Imaging of the Brain and Spine*. Number Bd. 1 in LWW medical book collection. Wolters Kluwer Health/Lippincott Williams & Wilkins, 2009. ISBN 9780781769853.
- Koenraad M.R. Audenaert and Fumio Hiai. On matrix inequalities between the power means: Counterexamples. *Linear Algebra and its Applications*, 439(5):1590 – 1604, 2013. ISSN 0024-3795. doi: <https://doi.org/10.1016/j.laa.2013.04.012>. URL <http://www.sciencedirect.com/science/article/pii/S0024379513002747>.
- Timothy Barth, Raphaële Herbin, and Mario Ohlberger. *Finite Volume Methods: Foundation and Analysis*, pages 1–60. American Cancer Society, 2017. ISBN 9781119176817. doi: 10.1002/9781119176817.ecm2010. URL <https://onlinelibrary.wiley.com/doi/abs/10.1002/9781119176817.ecm2010>.
- Peter J. Basser. Inferring microstructural features and the physiological state of tissues from diffusion-weighted images. *NMR in Biomedicine*, 8(7):333–344, 1995. doi: 10.1002/nbm.1940080707. URL <https://onlinelibrary.wiley.com/doi/abs/10.1002/nbm.1940080707>.
- Peter J. Basser and Carlo Pierpaoli. Microstructural and physiological features of tissues elucidated by quantitative-diffusion-tensor mri. *Journal of Magnetic Resonance*, 213(2): 560 – 570, 2011. ISSN 1090-7807. doi: <https://doi.org/10.1016/j.jmr.2011.09.022>. URL <http://www.sciencedirect.com/science/article/pii/S109078071100334X>. Magnetic Moments.
- P.J. Basser, J. Mattiello, and D. Lebihan. Estimation of the effective self-diffusion tensor

- from the nmr spin echo. *Journal of Magnetic Resonance, Series B*, 103(3):247 – 254, 1994. ISSN 1064-1866. doi: 10.1006/jmrb.1994.1037.
- P. Bastian, M. Blatt, A. Dedner, C. Engwer, R. Klöfkorn, R. Kornhuber, M. Ohlberger, and O. Sander. A Generic Grid Interface for Parallel and Adaptive Scientific Computing. Part II: Implementation and Tests in DUNE. *Computing*, 82(2–3):121–138, 2008a. doi: 10.1007/s00607-008-0004-9.
- P. Bastian, M. Blatt, A. Dedner, C. Engwer, R. Klöfkorn, M. Ohlberger, and O. Sander. A Generic Grid Interface for Parallel and Adaptive Scientific Computing. Part I: Abstract Framework. *Computing*, 82(2–3):103–119, 2008b. doi: 10.1007/s00607-008-0003-x.
- P. Bastian, F. Heimann, and S. Marnach. Generic implementation of finite element methods in the Distributed and Unified Numerics Environment (DUNE). *Kybernetika*, 46:294–315, 2010.
- K. V. Bhagwat and R. Subramanian. Inequalities between means of positive operators. *Mathematical Proceedings of the Cambridge Philosophical Society*, 83(3):393–401, 1978. doi: 10.1017/S0305004100054670.
- M. Blatt and P. Bastian. The iterative solver template library. In B. Kagström, E. Elmroth, J. Dongarra, and J. Wasniewski, editors, *Applied Parallel Computing – State of the Art in Scientific Computing*, pages 666–675, Berlin/Heidelberg, 2007. Springer.
- M. Blatt, A. Burchardt, A. Dedner, Ch. Engwer, J. Fahlke, B. Flemisch, Ch. Gersbacher, C. Gräser, F. Gruber, Ch. Grüninger, D. Kempf, R. Klöfkorn, T. Malkmus, S. Müthing, M. Nolte, M. Piatkowski, and O. Sander. The Distributed and Unified Numerics Environment, Version 2.4. *Archive of Numerical Software*, 4(100):13–29, 2016. ISSN 2197-8263. doi: 10.11588/ans.2016.100.26526.
- Pavel K. Brazhnik and John J. Tyson. On traveling wave solutions of fisher’s equation in two spatial dimensions. *SIAM Journal on Applied Mathematics*, 60(2):371–391, 1999. ISSN 00361399.
- P.S. Bullen. *Handbook of Means and Their Inequalities*. 560. Springer Netherlands, 2003. ISBN 978-1-4020-1522-9.

M. C. Chamberlain and P. A. Kormanik. Practical guidelines for the treatment of malignant gliomas. *The Western journal of medicine*, 168:114–20, Feb 1998.

Eric L. Chang, Serap Akyurek, Tedde Avalos, Neal Rebuena, Chris Spicer, John Garcia, Robin Famiglietti, Pamela K. Allen, K.S. Clifford Chao, Anita Mahajan, Shiao Y. Woo, and Moshe H. Maor. Evaluation of peritumoral edema in the delineation of radiotherapy clinical target volumes for glioblastoma. *International Journal of Radiation Oncology, Biology, Physics*, 68(1):144 – 150, 2007. ISSN 0360-3016. doi: 10.1016/j.ijrobp.2006.12.009.

Song Tao Timothy Cheo, Gek Hsiang Lim, and Keith Hsiu Chin Lim. Glioblastoma multiforme outcomes of 107 patients treated in two singapore institutions. *Singapore medical journal*, 58(1):41–45, January 2017. ISSN 0037-5675. URL <https://www.ncbi.nlm.nih.gov/pubmed/26915391>.

P. A. Cook, Y. Bai, S. Nedjati-Gilani, K. K. Seunarine, M. G. Hall, G. J. Parker, and D. C. Alexander. Camino: Open-source diffusion-mri reconstruction and processing, May 2006. URL http://www.cs.ucl.ac.uk/research/medic/camino/files/camino_2006_abstract.pdf.

G. Corbin, A. Hunt, A. Klar, F. Schneider, and C. Surulescu. Higher-order models for glioma invasion: From a two-scale description to effective equations for mass density and momentum. *Mathematical Models and Methods in Applied Sciences*, 28(09):1771–1800, 2018. doi: 10.1142/S0218202518400055.

G. Corbin, C. Engwer, A. Klar, J. Nieto, J. Soler, C. Surulescu, and M. Wenske. Modeling glioma invasion with anisotropy- and hypoxia-triggered motility enhancement: from subcellular dynamics to macroscopic pdes with multiple taxis. *Mathematical Models and Methods in Applied Sciences*, 2020.

Michael J. Crawley. *Statistics: An Introduction Using R, 2nd Edition*. Wiley, November 2014. ISBN ISBN: 978-1-118-94109-6.

R. M. deSouza, H. Shaweis, C. Han, V. Sivasubramiam, L. Brazil, R. Beaney, G. Sadler, S. Al-Sarraj, T. Hampton, J. Logan, V. Hurwitz, R. Bhangoo, R. Gullan, and K. Ashkan. Has the survival of patients with glioblastoma changed over the years? *British Journal*

- of Cancer*, 114(2):146–150, January 2016. ISSN 1532-1827. URL <https://doi.org/10.1038/bjc.2015.421>.
- Jerome Droniou. Finite volume schemes for diffusion equations: Introduction to and review of modern methods. *Mathematical Models and Methods in Applied Sciences*, 24(08):1575–1619, 2014. doi: 10.1142/S0218202514400041. URL <https://doi.org/10.1142/S0218202514400041>.
- Ian L. Dryden, Alexey Koloydenko, and Diwei Zhou. Non-euclidean statistics for covariance matrices, with applications to diffusion tensor imaging. *The Annals of Applied Statistics*, 3(3):1102–1123, 2009. ISSN 19326157.
- G. T. Eigestad and R. A. Klausen. On the convergence of the multi-point flux approximation o-method: Numerical experiments for discontinuous permeability. *Numerical Methods for Partial Differential Equations*, 21(6):1079–1098, 2005. doi: 10.1002/num.20079. URL <https://onlinelibrary.wiley.com/doi/abs/10.1002/num.20079>.
- C. Engwer and M. Wenske. Estimating the extent of glioblastoma invasion - approximate stationalisation of anisotropic advection-diffusion-reaction equations in the context of glioblastoma invasion. submitted 01/15/2020 at the Journal of Mathematical Biology (Springer), arXiv preprint at <https://arxiv.org/abs/2001.05369>, 2020.
- C. Engwer, T. Hillen, M. Knappitsch, and C. Surulescu. Glioma follow white matter tracts: a multiscale dti-based model. *J. Math Biol.*, 71:551–582, 2015.
- C. Engwer, A. Hunt, and C. Surulescu. Effective equations for anisotropic glioma spread with proliferation: a multiscale approach. *J. Math. Med. Biol.*, 33:435–459, 2016.
- Radek Erban and Hans G. Othmer. From signal transduction to spatial pattern formation in e. coli: A paradigm for multiscale modeling in biology. *Multiscale Modeling & Simulation*, 3(2):362–394, 2005. doi: 10.1137/040603565. URL <https://doi.org/10.1137/040603565>.
- Robert Eymard, Gérard Henry, Raphaële Herbin, Florence Hubert, Robert Klöforn, and Gianmarco Manzini. 3d benchmark on discretization schemes for anisotropic diffusion problems on general grids. In Jaroslav Fořt, Jiří Fürst, Jan Halama, Raphaële Herbin,

and Florence Hubert, editors, *Finite Volumes for Complex Applications VI Problems & Perspectives*, pages 895–930, Berlin, Heidelberg, 2011. Springer Berlin Heidelberg. ISBN 978-3-642-20671-9.

R. A. Fischer. The wave of advance of advantageous genes. *Annals of Eugenics*, 7(4): 355–369, 1937. doi: 10.1111/j.1469-1809.1937.tb02153.x.

Author comment: We cite this publication from the *Annals of Eugenics* as a historical document. The work of eugenicists was often pervaded by prejudice against racial, ethnic and disabled groups, and has also been misused as legitimization of horrible crimes against humanity. The citation should neither be seen as an endorsement of those views nor a promotion of eugenics in any way.

Alf Giese and Manfred Westphal. Glioma Invasion in the Central Nervous System. *Neurosurgery*, 39(2):235–252, 08 1996. ISSN 0148-396X. doi: 10.1097/00006123-199608000-00001. URL <https://doi.org/10.1097/00006123-199608000-00001>.

Pavlo G. Gritsenko, Olga Ilina, and Peter Friedl. Interstitial guidance of cancer invasion. *The Journal of pathology*, 226:185–99, Jan 2012.

S. Guzman, T. Herrada-Pineda, and Revilla-Pacheco F. *Surgical Management of Glioblastoma Glioblastoma*, chapter 12 - Surgical Management of Glioblastoma Glioblastoma. Codon Publications, 2017. URL <https://www.ncbi.nlm.nih.gov/books/NBK469999/>.

Brian C. Hall. The matrix exponential. In Brian C. Hall, editor, *Lie Groups, Lie Algebras, and Representations: An Elementary Introduction*, pages 31–48. Springer International Publishing, Cham, 2015. URL https://doi.org/10.1007/978-3-319-13467-3_2.

Hana L.P. Harpold, Ellsworth C. Alvord, Jr., and Kristin R. Swanson. The evolution of mathematical modeling of glioma proliferation and invasion. *Journal of Neuropathology Experimental Neurology*, 66(1):1–9, 2007. doi: 10.1097/nen.0b013e31802d9000. URL <http://dx.doi.org/10.1097/nen.0b013e31802d9000>.

Leith Hathout, Benjamin Ellingson, and Whitney Pope. Modeling the efficacy of the extent of surgical resection in the setting of radiation therapy for glioblastoma. *Cancer science*,

- 107(8):1110–1116, August 2016. ISSN 1347-9032. URL <https://pubmed.ncbi.nlm.nih.gov/27240229>.
- Haralampos Hatzikirou, Andreas Deutsch, Carlo Schaller, Matthias Simon, and Kristin Swanson. Mathematical modelling of glioblastoma tumour development: A review. *Mathematical Models and Methods in Applied Sciences*, 15(11):1779–1794, 2005. doi: 10.1142/S0218202505000960. URL <https://doi.org/10.1142/S0218202505000960>.
- Raphael Herbin and Florence Hubert. Benchmark on Discretization Schemes for Anisotropic Diffusion Problems on General Grids. In ISTE, editor, *Finite volumes for complex applications V*, pages 659–692, France, June 2008. Wiley. URL <https://hal.archives-ouvertes.fr/hal-00429843>.
- Thomas Hillen. M5 mesoscopic and macroscopic models for mesenchymal motion. *Journal of Mathematical Biology*, 53(4):585–616, Oct 2006. ISSN 1432-1416. doi: 10.1007/s00285-006-0017-y. URL <https://doi.org/10.1007/s00285-006-0017-y>.
- Thomas Hillen and Kevin J. Painter. *Transport and Anisotropic Diffusion Models for Movement in Oriented Habitats*, pages 177–222. Springer Berlin Heidelberg, Berlin, Heidelberg, 2013. ISBN 978-3-642-35497-7. doi: 10.1007/978-3-642-35497-7_7. URL https://doi.org/10.1007/978-3-642-35497-7_7.
- Rui Huang. Stability of travelling fronts of the fisher-kpp equation in \mathbb{R}^N . *Nonlinear Differential Equations and Applications NoDEA*, 15(4):599–622, December 2008. ISSN 1420-9004. URL <https://doi.org/10.1007/s00030-008-7041-0>.
- Alexander Hunt. *DTI-Based Multiscale Models for Glioma Invasion*. doctoralthesis, Technische Universität Kaiserslautern, 2018. URL <http://nbn-resolving.de/urn:nbn:de:hbz:386-kluedo-53575>.
- Alexander Hunt and Christina Surulescu. A multiscale modeling approach to glioma invasion with therapy. *Vietnam Journal of Mathematics*, 45(1):221–240, Mar 2017. ISSN 2305-2228. doi: 10.1007/s10013-016-0223-x. URL <https://doi.org/10.1007/s10013-016-0223-x>.
- Saâd Jbabdi, Emmanuel Mandonnet, Hugues Duffau, Laurent Capelle, Kristin Rae

- Swanson, Mélanie Péligrini-Issac, Rémy Guillevin, and Habib Benali. Simulation of anisotropic growth of low-grade gliomas using diffusion tensor imaging. *Magnetic Resonance in Medicine*, 54(3):616–624, 9 2005. ISSN 1522-2594. doi: 10.1002/mrm.20625. URL <https://doi.org/10.1002/mrm.20625>.
- Jayashree Kalpathy-Cramer, Elizabeth R. Gerstner, Kyrre E. Emblem, Ovidiu Andronesi, and Bruce Rosen. Advanced magnetic resonance imaging of the physical processes in human glioblastoma. *Cancer research*, 74:4622–4637, Sep 2014.
- A. B. Karim, B. Maat, R. Hatlevoll, J. Menten, E. H. Rutten, D. G. Thomas, F. Mascarenhas, J. C. Horiot, L. M. Parvinen, M. van Reijn, J. J. Jager, M. G. Fabrini, A. M. van Alphen, H. P. Hamers, L. Gaspar, E. Noordman, M. Pierart, and M. van Glabbeke. A randomized trial on dose-response in radiation therapy of low-grade cerebral glioma: European organization for research and treatment of cancer (eortc) study 22844. *International journal of radiation oncology, biology, physics*, 36:549–56, Oct 1996.
- Vosburgh K.G. Kikinis R., Pieper S.D. 3D Slicer: A platform for subject-specific image analysis, visualization, and clinical support, 2014. URL <https://www.slicer.org/>. 3D Slicer is an open source software platform for medical image informatics, image processing, and three-dimensional visualization.
- Runhild A. Klausen and Ragnar Winther. Convergence of multipoint flux approximations on quadrilateral grids. *Numerical Methods for Partial Differential Equations*, 22(6): 1438–1454, 2006. doi: 10.1002/num.20158. URL <https://onlinelibrary.wiley.com/doi/abs/10.1002/num.20158>.
- A. Kolmogoroff, I. Petrovsky, and N. Piscounoff. Study of the diffusion equation with growth of the quantity of matter and its application to a biology problem. In Pierre Pelcé, editor, *Dynamics of Curved Fronts*, pages 105 – 130. Academic Press, San Diego, 1988. ISBN 978-0-12-550355-6. doi: <https://doi.org/10.1016/B978-0-08-092523-3.50014-9>. URL <http://www.sciencedirect.com/science/article/pii/B9780080925233500149>.
- E. Konukoglu, O Clatz, Bjoern Menze, Bram Menze, Stieltjes, Marc-Andre Stieltjes B FAU Weber, Emmanuel Weber MA FAU Mandonnet, Herve Mandonnet E FAU Delingette, Nicholas Delingette H FAU Ayache, and Ayache N. Image guided per-

- sonalization of reaction-diffusion type tumor growth models using modified anisotropic eikonal equations. *IEEE Trans Med Imaging*, pages –, 2010.
- Ender Konukoglu, Olivier Clatz, Pierre-Yves Bondiau, Hervé Delingette, and Nicholas Ayache. Extrapolating tumor invasion margins for physiologically determined radiotherapy regions. In Rasmus Larsen, Mads Nielsen, and Jon Sporring, editors, *Medical Image Computing and Computer-Assisted Intervention – MICCAI 2006*, pages 338–346, Berlin, Heidelberg, 2006. Springer Berlin Heidelberg. ISBN 978-3-540-44708-5.
- Ender Konukoglu, Maxime Sermesant, Olivier Clatz, Jean-Marc Peyrat, Hervé Delingette, and Nicholas Ayache. A recursive anisotropic fast marching approach to reaction diffusion equation: Application to tumor growth modeling. *Information Processing in Medical Imaging*,, pages 687–699, 2007.
- Michel Lacroix, Dima Abi-Said, Daryl R. Fournay, Ziya L. Gokaslan, Weiming Shi, Franco DeMonte, Frederick F. Lang, Ian E. McCutcheon, Samuel J. Hassenbusch, Eric Holland, Kenneth Hess, Christopher Michael, Daniel Miller, and Raymond Sawaya. A multivariate analysis of 416 patients with glioblastoma multiforme: prognosis, extent of resection, and survival. *Journal of Neurosurgery*, 95(2):190 – 198, 2001. URL <https://thejns.org/view/journals/j-neurosurg/95/2/article-p190.xml>.
- Konstantin Lipnikov, Gianmarco Manzini, and Mikhail Shashkov. Mimetic finite difference method. *Journal of Computational Physics*, 257:1163 – 1227, 2014. ISSN 0021-9991. doi: <https://doi.org/10.1016/j.jcp.2013.07.031>. URL <http://www.sciencedirect.com/science/article/pii/S0021999113005135>. Physics-compatible numerical methods.
- Z. Liu and Chong-fang Ma. A new method for numerical treatment of diffusion coefficients at control-volume surfaces. *Numerical Heat Transfer, Part B: Fundamentals*, 47:491 – 505, 2004.
- Andreas Markus Loening and Sanjiv Sam Gambhir. Amide: A free software tool for multi-modality medical image analysis. *Molecular Imaging*, 2(3):15353500200303133, 2003. doi: 10.1162/15353500200303133. URL <https://doi.org/10.1162/15353500200303133>.
- MATLAB. (*R2016b*). The MathWorks Inc., Natick, Massachusetts, 2016.

Matthew McCormick, Xiaoxiao Liu, Luis Ibanez, Julien Jomier, and Charles Marion. Itk: enabling reproducible research and open science. *Frontiers in Neuroinformatics*, 8:13, 2014. ISSN 1662-5196. doi: 10.3389/fninf.2014.00013. URL <https://www.frontiersin.org/article/10.3389/fninf.2014.00013>.

Choukri Mekkaoui, Philippe Metellus, William J. Kostis, Roberto Martuzzi, Fabricio R. Pereira, Jean-Paul Beregi, Timothy G. Reese, Todd R. Constable, and Marcel P. Jackowski. Diffusion tensor imaging in patients with glioblastoma multiforme using the supertoroidal model. *PloS one*, 11(1):e0146693–e0146693, January 2016. ISSN 1932-6203. URL <https://pubmed.ncbi.nlm.nih.gov/26761637>.

M. Moakher. A differential geometric approach to the geometric mean of symmetric positive-definite matrices. *SIAM Journal on Matrix Analysis and Applications*, 26(3): 735 – 747, 2005.

Maher Moakher. On the averaging of symmetric positive-definite tensors. *Journal of Elasticity*, 82(3):273–296, 2006. ISSN 1573-2681. URL <https://doi.org/10.1007/s10659-005-9035-z>.

Diana Furst Nelson, Walter J. Curran, Charles Scott, James S. Nelson, Alan S. Weinstein, Khurshid Ahmad, Louis S. Constine, Kevin Murray, William D. Powlis, Mohammed Mohiuddin, and Jennifer Fischbach. Hyperfractionated radiation therapy and bis-chlorethyl nitrosourea in the treatment of malignant glioma—possible advantage observed at 72.0 gy in 1.2 gy b.i.d. fractions: Report of the radiation therapy oncology group protocol 8302. *International Journal of Radiation Oncology*Biology*Physics*, 25(2):193 – 207, 1993. ISSN 0360-3016. doi: [https://doi.org/10.1016/0360-3016\(93\)90340-2](https://doi.org/10.1016/0360-3016(93)90340-2). URL <http://www.sciencedirect.com/science/article/pii/0360301693903402>.

Ryo Nishikawa. Standard therapy for glioblastoma—a review of where we are. *Neurologia medico-chirurgica*, 50:713–9, 2010.

American Association of Neurological Surgeons (AANS). Glioblastoma multiforme, 2020. URL <https://www.aans.org/en/Patients/Neurosurgical-Conditions-and-Treatments/Glioblastoma-Multiforme>.

Evren Özarslan, Baba C. Vemuri, and Thomas H. Mareci. Generalized scalar measures

- for diffusion mri using trace, variance, and entropy. *Magnetic Resonance in Medicine*, 53(4):866–876, 2005. doi: 10.1002/mrm.20411. URL <https://onlinelibrary.wiley.com/doi/abs/10.1002/mrm.20411>.
- Kevin J. Painter and Thomas Hillen. *From Random Walks to Fully Anisotropic Diffusion Models for Cell and Animal Movement*, pages 103–141. Springer International Publishing, Cham, 2018. ISBN 978-3-319-96842-1. doi: 10.1007/978-3-319-96842-1_5. URL https://doi.org/10.1007/978-3-319-96842-1_5.
- K.J. Painter and T. Hillen. Mathematical modelling of glioma growth: The use of diffusion tensor imaging (dti) data to predict the anisotropic pathways of cancer invasion. *Journal of Theoretical Biology*, 323:25 – 39, 2013. ISSN 0022-5193. doi: <https://doi.org/10.1016/j.jtbi.2013.01.014>. URL <http://www.sciencedirect.com/science/article/pii/S0022519313000398>.
- Vishal Patel and Leith Hathout. Image-driven modeling of the proliferation and necrosis of glioblastoma multiforme. *Theoretical Biology and Medical Modelling*, 14(1):10, May 2017. ISSN 1742-4682. doi: 10.1186/s12976-017-0056-7. URL <https://doi.org/10.1186/s12976-017-0056-7>.
- Nicole Porz, Stefan Bauer, Alessia Pica, Philippe Schucht, Jürgen Beck, Rajeev Kumar Verma, Johannes Slotboom, Mauricio Reyes, and Roland Wiest. Multi-modal glioblastoma segmentation: Man versus machine, 05 2014. URL <https://doi.org/10.1371/journal.pone.0096873>.
- W. H. Reed and T. R. Hill. Triangular mesh methods for the neutron transport equation. In *Triangular mesh methods for the neutron transport equation*, 1973. URL <https://www.osti.gov/biblio/4491151>.
- Patrick J. Roache. Code Verification by the Method of Manufactured Solutions . *Journal of Fluids Engineering*, 124(1):4–10, 11 2001. ISSN 0098-2202. doi: 10.1115/1.1436090. URL <https://doi.org/10.1115/1.1436090>.
- Conrad Sanderson and Ryan Curtin. Armadillo: a template-based c++ library for linear algebra. *Journal of Open Source Software*, Vol. 1:pp. 26, 2016.

Conrad Sanderson and Ryan Curtin. A user-friendly hybrid sparse matrix class in c++. *Lecture Notes in Computer Science (LNCS)*, Vol. 10931:pp. 422–430, 2018.

Boris Schling. *The Boost C++ Libraries*. XML Press, 2011. ISBN 0982219199.

Daniel L. Silbergeld and Michael R. Chicoine. Isolation and characterization of human malignant glioma cells from histologically normal brain. *Journal of Neurosurgery*, 86(3):525 – 531, 1997. URL <https://thejns.org/view/journals/j-neurosurg/86/3/article-p525.xml>.

V.R. Simi and Justin Joseph. Segmentation of glioblastoma multiforme from mr images – a comprehensive review. *The Egyptian Journal of Radiology and Nuclear Medicine*, 46(4): 1105 – 1110, 2015. ISSN 0378-603X. doi: <https://doi.org/10.1016/j.ejrnrm.2015.08.001>. URL <http://www.sciencedirect.com/science/article/pii/S0378603X15001813>.

Anne Line Stensjøen, Ole Solheim, Kjell Arne Kvistad, Asta K. Håberg, Øyvind Salvesen, and Erik Magnus Berntsen. Growth dynamics of untreated glioblastomas in vivo. *Neuro-Oncology*, 17(10):1402–1411, 03 2015. ISSN 1522-8517. doi: 10.1093/neuonc/nov029. URL <https://doi.org/10.1093/neuonc/nov029>.

R. Stupp, M. Brada, M.J. van den Ben, J.-C. Tonn, and G. Pentheroudakis. High-grade glioma: Esmo clinical practice guidelines for diagnosis, treatment and follow-up. *Annals of Oncology*, 25:iii93 – iii101, 2014. ISSN 0923-7534. doi: <https://doi.org/10.1093/annonc/mdu050>. URL <http://www.sciencedirect.com/science/article/pii/S0923753419340773>. ESMO Updated Clinical Practice Guidelines.

Roger Stupp, Warren P. Mason, Martin J. van den Bent, Michael Weller, Barbara Fisher, Martin J. B. Taphoorn, Karl Belanger, Alba A. Brandes, Christine Marosi, Ulrich Bogdahn, Jürgen Curschmann, Robert C. Janzer, Samuel K. Ludwin, Thierry Gorlia, Anouk Allgeier, Denis Lacombe, J. Gregory Cairncross, Elizabeth Eisenhauer, and René O. Mirimanoff. Radiotherapy plus concomitant and adjuvant temozolomide for glioblastoma. *The New England journal of medicine*, 352:987–96, Mar 2005.

Christina Surulescu. glioMath, 2016. URL <https://www.uni-muenster.de/GlioMaTh/>.

Amanda Swan, Thomas Hillen, John C. Bowman, and Albert D. Murtha. A patient-specific

- anisotropic diffusion model for brain tumour spread. *Bulletin of Mathematical Biology*, 80(5):1259–1291, May 2018. ISSN 1522-9602. doi: 10.1007/s11538-017-0271-8. URL <https://doi.org/10.1007/s11538-017-0271-8>.
- K. R. Swanson, E. C. Alvord, and J. D. Murray. A quantitative model for differential motility of gliomas in grey and white matter. *Cell Proliferation*, 33(5):317–329, 2000. doi: 10.1046/j.1365-2184.2000.00177.x.
- K R Swanson, R C Rostomily, and E C Alvord. A mathematical modelling tool for predicting survival of individual patients following resection of glioblastoma: a proof of principle. *British Journal of Cancer*, 98(1):113–119, 2008. ISSN 1532-1827. URL <https://doi.org/10.1038/sj.bjc.6604125>.
- K.R Swanson, E.C Alvord, and J.D Murray. Virtual resection of gliomas: Effect of extent of resection on recurrence. *Mathematical and Computer Modelling*, 37(11):1177 – 1190, 2003. ISSN 0895-7177. doi: [https://doi.org/10.1016/S0895-7177\(03\)00129-8](https://doi.org/10.1016/S0895-7177(03)00129-8). URL <http://www.sciencedirect.com/science/article/pii/S0895717703001298>. Modeling and Simulation of Tumor Development, Treatment, and Control.
- Kristin R. Swanson, Russell C. Rockne, Jonathan Claridge, Mark A. Chaplain, Ellsworth C. Alvord, and Alexander R.A. Anderson. Quantifying the role of angiogenesis in malignant progression of gliomas: In silico modeling integrates imaging and histology. *Cancer Research*, 71(24):7366–7375, 2011. ISSN 0008-5472. doi: 10.1158/0008-5472.CAN-11-1399. URL <https://cancerres.aacrjournals.org/content/71/24/7366>.
- P Tracqui. Biophysical models of tumour growth. *Reports on Progress in Physics*, 72(5): 056701, apr 2009. doi: 10.1088/0034-4885/72/5/056701. URL <https://doi.org/10.1088%2F0034-4885%2F72%2F5%2F056701>.
- P. Tracqui, G. C. Cruywagen, D. E. Woodward, G. T. Bartoo, J. D. Murray, and E. C. Alvord Jr. A mathematical model of glioma growth: the effect of chemotherapy on spatio-temporal growth. *Cell Proliferation*, 28(1):17–31, 1995. doi: 10.1111/j.1365-2184.1995.tb00036.x.
- Tomasz Tykocki and Mohamed Eltayeb. Ten-year survival in glioblastoma. a systematic review. *Journal of Clinical Neuroscience*, 54:7 – 13, 2018. ISSN 0967-5868. doi: <https://doi.org/10.1016/j.jocn.2018.05.011>.

[//doi.org/10.1016/j.jocn.2018.05.002](https://doi.org/10.1016/j.jocn.2018.05.002). URL <http://www.sciencedirect.com/science/article/pii/S0967586817317216>.

Johannes Vorwerk, Jae-Hyun Cho, Stefan Rampp, Hajo Hamer, Thomas R. Knösche, and Carsten H. Wolters. A guideline for head volume conductor modeling in eeg and meg. *NeuroImage*, 100:590–607, Oct 2014.

A Appendix

A.1 Reproduction of numerical results

Most of the numerical tests we presented were set up so that they are easily reproducible for other researchers. We provide the output data of our numerical tests in the supplementary material. The numerical investigation of the Hölder method via the manufactured solutions and the 1D, 2D and 3D examples (see Section 4.5) can also be reproduced. Only the 3D comparisons of Section 6 require the full glioMath dataset. In the supplementary material we provide a working version of DUNE-glio, the configuration files (*.ini*) that were used to generate all numerical results and a digital copy of this document.

To reproduce the numerical results, do the following:

1. Open the supplementary material.
2. Retrieve all dependencies (see Section 5). The DUNE dependencies (major version 2.7) can be loaded with a provided bash script (`load_dune_dependencies.sh`).
3. Build DUNE-glio via the provided scripts (`release_compile.sh`) or via the DUNE build system. For a more recent version, retrieve a copy of DUNE-glio from <https://zivgitlab.uni-muenster.de/ag-engwer/dune-glio> and consult the documentation and the readme files therein for build instructions. The CMake build system should automatically produce multiple executables corresponding to our numerical examples.
4. Run the executable corresponding to the given numerical test while providing the config-file and a data-config file as command line arguments.

It is also possible to start the simulations consecutively via a provided bash script `run.sh` within the build folder.

Curriculum Vitae

Personal Information

Name: Michael Wenske
Address: Hansaring 32
48155, Münster
Germany
Date of birth: July 3rd, 1989
Place of birth: Bielefeld

Work experience

2017-2020 Institute of Applied Mathematics, WWU Münster
2009-2010 Civilian service in Accra, Ghana

Academic studies

2010-2017 Master of Science (Physics), WWU Münster.
2010-2014 Bachelor of Science (Physics), WWU Münster.
2000-2009 Abitur, Gymnasium Verl

Begin of PhD

2.5.2017 Supervisor: Prof. Christian Engwer

Münster, Germany, December 17, 2020

Erklärung der Eigenständigkeit

Hiermit versichere ich, Michael Wenske, dass ich die vorliegende Arbeit selbstständig verfasst habe und keine anderen als die angegebenen Quellen und Hilfsmittel verwendet habe.

Münster, Datum _____